ER9408

DYNAMICS OF SOIL-MOISTURE, SUBSURFACE FLOW AND RUNOFF IN COMPLEX TERRAIN

Christopher J. Duffy, PhD
Do-Hun Lee
Ming-Hui Jin

Report to U.S. Army Research Office
DAAL03-90-G-0075

July 1994

PENNSTATE

1855

ENVIRONMENTAL RESOURCES RESEARCH INSTITUTE

UNIVERSITY PARK, PA

Title

Dynamics of Soil-Moisture, Subsurface Flow and Runoff in Complex Terrain

by

Christopher J. Duffy

Associate Professor of Civil and Environmental Engineering

with

Do-Hun Lee

Ming-Hui Jin

Graduate Student Participants

8 July 1994

Report to

U. S. Army Research Office

DAAL03-90-G-0075

Department of Civil and Environmental Engineering

Penn State University

Table of Contents

1. INTRODUCTION AND RESEARCH OVERVIEW

1.1 Dynamic Hydrology and Complex Terrain

The focus of this research has been the study of spatio-temporal dynamics of the rainfall-runoff process in the common situation where topographic relief and shallow subsurface moisture control the storage and timing of runoff on the landscape. The geometry (shape, curvature, etc.) of the hillslope, catchment or river basin exerts a major control on the hydrologic storage-response, by defining the domain and boundary conditions of moisture storage. The difficulties stem from the fact that the governing equation known as Richards equation (Richards, 1931) is strongly nonlinear, requiring the solution of extremely large systems of equations even for small problems, and observed data (eg. soil moisture, groundwater levels, soil and geologic permeability) are typically not well resolved in space and/or time. Although the form of the nonlinearities in the governing local equations may be mathematically understood, the expression of these nonlinearities in the integrated spatio-temporal response of hillslope and watershed runoff, are not understood at present. Topographic, soil and geologic spatial variation further adds to the computational burden of solving the four dimensional Richards equation. Modeling the physical processes of such a system over multiple spatial scales remains a fundamental challenge for hydrologic science.

The role of topographic structure on hydrologic processes and modeling is a fundamental theme of this research effort. The research will attempt to incorporate the essentials of this structure directly into the model formulation. This approach is felt to be particularly useful where hydrologic predictions must be made over multiple scales (theories) appropriate to hillslopes, watersheds and river basins. In this regard we make the following assumptions: (1) The hillslope is the fundamental spatial scale characterizing a storage reservior which produces runoff. The hillslope itself is defined as that region bounded above by a topographic/hydrologic divide, bounded laterally by trajectories following the steepest path from divide to stream, and bounded below by a line or surface of discharge. It is noted that the boundary conditions of all hillslopes are directly tied to the drainage network. (2) The classical hypsometric, or area-elevation relationship, represents the physical domain of a hydrologic response unit. As such, it can be applied to all scales of interest (e.g. the hillslope, watershed or river basin scale). (3) The hypsometric relation $F(\phi)$ is defined as a probability distribution in the following sense. $F(\phi)$ is the fraction of area below an elevation contour ϕ, normalized by the total area. Likewise there exists a complementary hypsometric relationship $F(\psi)$, where ψ represent the orthogonal

trajectories of ϕ. $F(\psi)$ is defined as the fraction of area contained below a ψ contour. (4) Spatial averaging of hydrologic state variables (e.g. soil misture, saturated groundwater levels, etc) should be made with respect to the particular hydrologic unit. The appropriate weighting function for spatial averaging is the hypsometric distribution. Chapter 2 discusses in detail the implications of hypsometry to modeling and data structures within a hydrologic response unit.

A major effort of the last three years has been to devise a methodology for constructing spatially integrated constitutive relations for storage and flux of water on hillslopes and small watersheds. As the field data is typically sparse, the analysis must be supported by numerical experiments. A comprehensive series of numerical experiments were conducted as part of this research, and spatially integrated constitutive relations required in the dynamical model were proposed. In Chapter 3, steady-state flux-storage relationships are constructed from Richards equation subject to variations in slope shape, slope gradient, aspect ratio, and soil type. Steady-state flux-storage relationships are parameterized using a polynomial relationship. Following the steady-state analysis, the dynamic storage-flux relationships are examined by a series of numerical experiments with a range of input forcing pattern, slope shape, soil type, and boundary conditions.

In chapter 4 the research will explore the storage-flux relationships for Watershed No. 2 of the Shale Hills Watersheds in central PA using field measurements of soil moisture, water table elevation, and streamflow (Lynch, 1976). It is shown that the hypsometric duistribution of the hillslope, and spatial scaling transformations of the surface and bedrock topography, allow construction of integrated state variables of the hillslope. Namely the soil moisture γ and saturated storage η. Storage-flux relationships are then established for the watershed. The analysis shows that the dynamical behaviour between γ and η exhibits an inverse relationship, while storage-flux relationships display hysteretic behaviour. The field analysis demonstrates that local topographic scaling is a useful tool for modeling where sparse and scattered field data exists. Chapter 5 discusses solutions to the two-state dynamical system, and Chapter 6 examines scaling relations of digital elevation models, and the application of mapping seasonal precipitation and evaporation in mountainous terrain.

To summarize, the research uses a hypsometric basis to construct spatial averages of hydrologic state variables at the hillslope and watershed scale. The basis is applied to the partial differential equations for unsaturated-saturated flow to arrive at a low-dimensional predictive model for rainfall-storage-runoff, and to the interpretation of field data at Shale Hills watershed No. 2 to test the concept. Numerical experiments are used to

define the form of integrated constitutive relations as a function of hillsope geometry (relief, slope, curvature, convergence, soil type, soil depth).

1.2 A Brief Review of the Literature

Beven (1983) provides a comprehensive review of the role of basin structure on runoff generation. He points out the complicating issues of spatial and temporal variability. Nonetheless, he contends that the 'ordered nature' of drainage basins suggests it should be possible to develop a unifying theory relating basin structure to runoff response. Siviplan et al. (1990) provide an excellent overview of the importance of hydrologic similarity and scale on the problem of rainfall-runoff. The concept of a geomorphic unit hydrograph, of Rodriguez-Iturbe and Valdes (1979), and Gupta et al. (1980) provides a fundamental link between the stream network, stream order, contributing area, and empirical models of hydrologic response. The present research serves to extend the concept of a hydrogeomorphic response unit to include a physically-based and nonlinear response at the hillslope scale.

On the experimental side, Dunne (1978) summarizes the field evidence for currently accepted physical mechanisms generating streamflow. He suggests that the various processes (Horton overland flow, subsurface flow, and saturation overland flow) are not mutually exclusive, but rather are synergistic, where multiple pathways of storm runoff depend on physical geography, initial condition, and intensity of the hydrologic event. Jeppson and Shreiber (1972), using early data from the Upper Sheep Creek experiment, were one of the first to apply two-dimensional unsaturated flow theory to hillslope modeling. Subsequently Stephenson and Freeze (1974) simulated the Upper Sheep hillslope as a two-dimensional, transient system using finite differences. During the 70's, many advances were made in algorithms for numerical computation in subsurface hydrology (Freeze, 1971; Neuman, Feddes and Bresler 1975), and in instrumentation and experimentation of soil water processes in the field. Conceptual understanding of soil-water processes on natural landscapes such as macropore flow, spatial variability, basin structure etc., was a major focus of research during this period (see Beven, 1983, for review). At the basin scale, Klemeš (1983) examined the monthly dynamic relationship between runoff and basin storage using rainfall and runoff data from the Rainy Lake Basin in western Ontario, Canada. The storage-runoff relationship showed a complex pattern, however a linear relationship was used based on the winter season data. In a small hillslope catchment near the western suburbs of Tokyo, Ando et al. (1983) measured groundwater level and streamflow. Using these data, a quadratic relationship between

groundwater runoff and groundwater storage was derived. On the basis of this relationship, hourly and daily time scale hydrologic models were developed.

Recently the dynamics of soil moisture over large regions has begun to receive important attention. Rodriguez-Iturbe et al. (1991) have examined the nonlinear dynamics of soil moisture at, what they refer to as the climate-scale. In this research a statistical-dynamical model is developed to represent surface hydrology over continental regions. Famiglietti and Wood (1991) specifically deal with development of a catchment-scale water balance model for an intensively monitored field experiment in Kansas.

Klemeš (1983) emphasizes testability and observability as important elements of conceptualization and model development. He argues that many conceptual hydrologic models are developed without considering their testability. Stephenson and Freeze (1974) point out the difficulties of calibrating and testing a physically based model (i.e., Richards equation), even at a well-equipped experimental watershed. The problem of what to measure, and where to measure it remains an important issue. The application of dynamical systems methodology as an organizing framework to study hydrologic processes in complex terrain, offers a consistent way of linking data to models, and ultimately to satisfy requirements of observability and testiblility.

2. INTEGRAL BALANCE MODELS AND TOPOGRAPHIC STRUCTURE

2.1 The Integral-Balance and State-Space Concept

It can be said that the fundamental equation of hydrology is represented by the simple water balance or conservation of fluid volume

$$\frac{dS}{dt} = I - Q \qquad (1)$$

where S represents the fluid storage volume, I the volumetric input and Q the volumetric discharge or output. For a hydrologic system with interacting physical processes and time scales, (1) is represented in the general state-space form

$$\frac{d\bar{\xi}}{dt} = \bar{u}(\bar{\xi},t) - \bar{f}(\bar{\xi},t) \qquad (2)$$

where storage is now a vector of state variables $\bar{\xi} = \{\xi_1, \xi_2, \ldots \xi_n\}$, with input flux vector $\bar{u} = \{u_1, u_2, \ldots u_n\}$, and the output flux vector $\bar{f} = \{f_1, f_2, \ldots f_n\}$. Formulating the particular dynamical model, requires a determination of the geometry and spatial scale of the system, the corresponding dimension of the state-space n and finally, estimation of the particular form of the constitutive or storage-flux relationship $\bar{f}(\bar{\xi},t)$, $\bar{u}(\bar{\xi},t)$ at the particular scale. Clearly, as scales and geometry change, the dimension of the state-space may change and the storage-flux relationships may change as well. Nonetheless, the state-space approach offers a general framework to study the dynamics of hydrologic systems across multiple scales.

Throughout this research it is assumed that state variables (e.g. soil moisture and saturated storage) can be represented by spatial averages. These averages must taken with respect to the geometry of the hydrologic flow system in question, and not simply averaged over an arbitrary region. In this section it is shown that the hypsometric or area-elevation relation, when redefined in terms of probability, serves as a physical meaningful weighting function.

To proceed, we consider a general space-time representation for the state variable $y(\bar{x},t)$ of the form

$$y(\bar{x},t) = \sum_{k=1}^{\infty} y_k(t)\alpha_k(\bar{x}) \qquad (3)$$

where $y_k(t)$ represents the k_{th} amplitude and $\alpha_k(\bar{x})$ are a corresponding set of spatial modes or shape functions with respect to the position vector $\bar{x}=\{x_1,x_2,x_3\}$. The next section develops the relationship between the $\alpha_k(\bar{x})$, hypsometry and spatial averages.

2.2 Hypsometry, Probability and Topographic Shape Functions

A classical descriptor of the morphology of a watershed or river basin uses the concept of the hypsometric function or area-elevation relationship, introduced to the hyrology literature by Langbein et al (1947). The hypsometric curve is an empirical, nondimensional curve relating the fraction of catchment area contained by an elevation contour. It is defined for any scale of hydrologic response, from hillslope, to watershed, or river basin. The hypsometric curve or its integral has been shown to be related to geomorphic characteristics of the drainage network. For example Hack (1957) relates drainage basin area to the length of longest channel. Geologic interpretations of the characteristic shapes of the hypsometric curve for a given landform (see Schumm (1956), or Sheideggar (1970)), generally assert that the present state of the landform depends on the balance of tectonic and erosive activity, and degree of disequilibrium. Notwithstanding these implications, the hypsometric relation is fundamentally a means to reduce the spatial dimension of a topographic surface to a simple function of elevation. In the context of hydrology, the hypsometric relation defines the domain over which state variables (e.g. soil moisture and saturated storage) contribute to runoff.

The hypsometry of a hydrologic unit is defined

$$\frac{A(\phi)}{A_T} = 1 - F(\phi) \qquad (4)$$

where $\phi=z$ represents the normalized elevation contour above base level ($0 \le z \le 1$), $A(\phi)$ is area associated with $z>\phi$, A_T is the total area of the basin, and $F(\phi)$ is the fraction of total area enclosed by $z \le \phi$ in the catchment, or in terms of probability, $F(\phi)=\text{prob}(z \le \phi)$. Likewise, we may define a function orthogonal to ϕ, describing the path or trajectory of the landform, ψ. Both ϕ and ψ are defined with respect to the natural coordinates of the landform $\{s,n\}$. Figure 2.1 illustrates the elevation contours and orthogonal trajectories for a small watershed near Penn State campus known as Shale Hills Experimental Watershed (J. Lynch, 1976). Also indicated in Figure 1 is the hypsometric relation defined by (4).

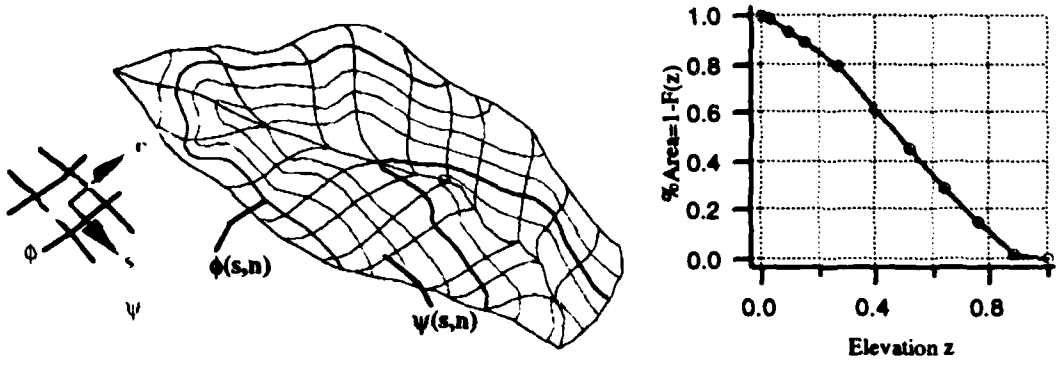

Figure 2.1 Elevation contours and orthogonal trajectories ϕ and ψ, in the natural coordinate system {s, n} for the Shale Hills Watershed #2. Also shown is the hypsometric relation.

The rationale for a probabilistic interpretation of the hypsometric relation, is to construct a weighting function for spatial averaging of state variables. For the state variable $y(\phi)$, the k_{th} spatial moment is given

$$E[y^k(\phi)] = \int_{z=0}^{z_{max}} y^k(\phi)\, f(\phi) d\phi; \quad . \qquad (5).$$

Practical experience suggests that local effects of aspect, vegetation, soils, geology, etc. may influence the y-process. In these cases it will be useful to construct conditional spatial averages over subregions within the watershed. A subregion is defined as the area contained by a pair of flow trajectories, $\Delta\psi=\psi_2-\psi_1$ which originate at the local topographic divide, and intersect the stream at local base level. The conditional distribution for the subregion with elevation change $z_1<\phi\leq z_2$ is given by

$$F(\phi|\Delta\psi) = \int_{z_1}^{z_2} f(\phi|\Delta\psi)d\phi = \frac{F(\phi)-F(z_1)}{F(z_2)-F(z_1)}, \qquad (6)$$
$$= 0, \quad \phi \leq z_1$$
$$= 1, \quad \phi > z_2,$$

and the conditional density is defined

$$f(\phi|\Delta\psi) = \frac{dF(\phi|\Delta\psi)}{d\phi} = \frac{f(\phi)}{\int_{z_1}^{z_2} f(\phi)d\phi} = \frac{f(\phi)}{F(z_2)-F(z_1)} \; . \qquad (7)$$

Conditional expectation of the state variable, $y(\phi)$ within the subregion $\Delta\psi$ is given by

$$E[y(\phi)|\Delta\psi] = \int_{z_1}^{z_2} y(\phi)\; f(\phi|\Delta\psi)d\phi \qquad (8)$$

If the catchment is made up of non-overlapping subregions i=1,2,...m the density for the overall region is

$$f_\phi(\phi) = \sum_{i=1}^{m} \lambda_i f_i(\phi|\Delta\psi_i); \qquad \sum_{i=1}^{m} \lambda_i = 1 \tag{9}$$

where $f_i(\phi)$ is now the local density and λ_i the fraction of area associated with $\Delta\psi_i$. The spatial average for the subregion y_i is given by

$$y_i = E[y_i(\phi)|\Delta\psi_i] = \int_{z_1}^{z_2} y_i(\phi) f_i(\phi|\Delta\psi_i) d\phi \tag{10}$$

The spatial average for the entire catchment is then determined from (10) and

$$\bar{y} = \sum_{i=1}^{m} \lambda_i y_i \tag{11}$$

A general approach to the problem of hypsometric subregions, can be devised by looking at the joint distribution of elevation ϕ and the orthogonal trajectories ψ. Let $F_y(\psi)$ be the fraction of catchment area below a given ψ.

$$F_\psi(\psi) = \frac{A(z) \le \psi)}{\text{total area}}, \tag{12}$$

$F_f(\phi)$ is now given in complementary form

$$F_\phi(\phi) = \frac{A(z) \le \phi}{\text{total area}}. \tag{13}$$

The relative frequency or specific area for each is given by

$$f_\phi(\phi) = \frac{dF_\phi(\phi)}{d\phi}; \qquad f_\psi(\psi) = \frac{dF_\psi(\psi)}{d\psi} \tag{14}$$

The functions ϕ and ψ are orthogonal, and if they also happen to be statistically independent , the joint distribution can be written

$$f_{\phi\psi}(\phi,\psi) = f_\phi(\phi) \cdot f_\psi(\psi) \tag{15}$$

Applying the usual rules for determining the marginal density from the joint density yields

$$f_\phi(\phi) = \int_{-\infty}^{\infty} F_{\phi\psi}(\phi,\psi) d\psi; \quad f_\psi(\psi) = \int_{-\infty}^{\infty} F_{\phi\psi}(\phi,\psi) d\phi; \tag{16}$$

The conditional density for ϕ is

$$f_{\phi|\psi}(\phi|\psi) = \frac{f_{\phi\psi}(\phi,\psi)}{f(\psi)} = f(\phi) \tag{17}$$

To estimate spatial moments of the process $y=g(\phi,\psi)$, we take the joint-conditional expectation over the subregion $\Delta\phi$ and $\Delta\psi$

$$E[y^k|\Delta\phi,\Delta\psi] = \int_{\psi_1}^{\psi_2}\int_{\phi_1}^{\phi_2} g^k(\phi,\psi)\, f_{\phi|\Delta\phi}(\phi|\Delta\phi) \cdot f_{\psi|\Delta\psi}(\psi|\Delta\psi) d\phi d\psi. \tag{18}$$

Figure 2.2. illustrates the complementary functions $F_\phi(\phi)$ and $F_\psi(\psi)$ for the Shale Hills watershed of Figure 2.1, and indicates a subregion over which spatial moments are locally conditioned by discrete pairs of elevation contours and flow paths.

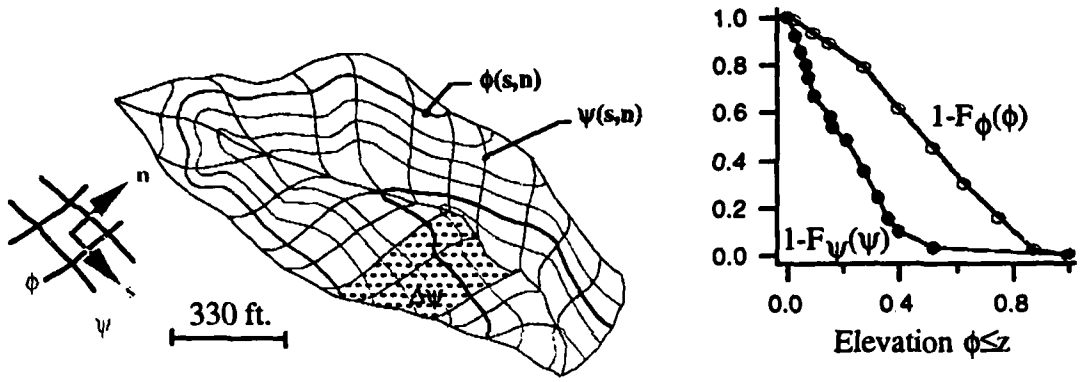

Figure 2.2 The complementary hypsometric distributions $F_\phi(\phi)$, the fraction area enclosed by $\phi \le z$ and $F_\psi(\psi)$, the area enclosed by $\psi \le z$. The hillslope (shaded region) represents the conditional area fraction bounded by the region $\Delta\phi$ and $\Delta\psi$.

The above probability arguments are easily extended to the general the spatio-temporal process represented by (1). For the special case where a hypsometric basis is appropriate ($\bar{x} -> \phi$. It is instructive to decompose $y(\phi,t)$ into a time average ($\bar{y}$) and a stationary time-fluctuation (y')

$$y(\phi,t) = \bar{y}(\phi) + y'(\phi,t) \qquad (19)$$

where $\bar{y}(\phi)$ is a simple function of elevation (ϕ), while the perturbation $y'(\phi,t)$ varies with elevation and time. Now let $y'(\phi,t)$, have the expansion

$$y'(\phi,t) = \sum_k y_k(t)\alpha_k(\phi) \qquad (20)$$

where $y_k(t)$ is a zero mean stationary process in time representing stationary harmonic *and/or random contributions* to the overall process, and $\alpha_k(\phi)$ represents the basis functions or shape functions for the same component of the y fluctuation. The y-process now has the representation

$$y(\phi,t) = \bar{y}(\phi) + \sum_k y_k(t)\alpha_k(\phi) \qquad (21)$$

Taking the first moment with respect to elevation ϕ yields

$$\begin{aligned} M_{(1)}(t) &= E_z[y(\phi,t)] = E_z[\bar{y}(\phi)] + y_1(t)E_z[\alpha_1(\phi)] + y_2(t)E[\alpha_2(\phi)] + \ldots. \\ &= \int_\phi \bar{y}(\phi)f_\phi(\phi)d\phi + y_1(t)\int_\phi \alpha_1(\phi)f_\phi(\phi)d\phi + y_2(t)\int_\phi \alpha_2(\phi)f_\phi(\phi)d\phi + \ldots\ldots \\ &= \bar{\bar{y}} + \beta_1 y_1(t) + \beta_2 y_2(t) + \ldots. \end{aligned} \qquad (22)$$

The coefficients β_k represents the elevation-weighted average contribution to the k_{th} time fluctuation in y, and $\bar{\bar{y}}$represents the ϕ-t average. In cases where the state variable is a function of two independent spatial variables, $y=g(\phi,\psi,t)$, the perturbation is given by

$$y(\phi,\psi,t) = \bar{\bar{y}}(\phi,\psi) + \sum_k y_k(t)\alpha_k(\phi,\psi)$$

Taking the first moment with respect to ϕ and ψ yields

$$M_{(1)}(t) = E_{\phi\psi}[y(\phi,\psi,t)] = E_{\phi\psi}[\bar{\bar{y}}(\phi,\psi)] + y_1(t)E_{\phi\psi}[\alpha_1(\phi,\psi)] + y_2(t)E_{\phi\psi}[\alpha_2(\phi,\psi)]+....$$

$$= \iint_{\phi\psi} \bar{\bar{y}}(\phi,\psi)f_{\phi\psi}(\phi,\psi)d\phi d\psi + y_1(t)\iint_{\phi\psi} \alpha_1(\phi,\psi)f_{\phi\psi}(\phi,\psi)d\phi d\psi+....$$

$$= \bar{\bar{\bar{y}}} + \beta_1 y_1(t) + \beta_2 y_2(t)+..... \qquad (23)$$

The coefficients β_k represent the spatial mean contribution to the k_{th} time fluctuation in y, and $\bar{\bar{\bar{y}}}$represents the ϕ–ψ-t average. In Chapter 6 a method for estimation of the $\alpha(z)$'s is presented for seasonal orographic precipitation and temperature fluctuations in the Wasatch mountains of northern Utah (Fan and Duffy, 1992).

In some cases it will be useful to relate the hypsometric function $f_\phi(\phi)$ to map distance 's' rather than elevation. This is done by defining a characteristic trajectory of the catchment, and applying a change of variable. The obvious characteristic trajectory is the elevation of the channel, z(s) with projected distance, $s=(x^2+y^2)^{1/2}$. To cover the full range of elevation in the catchment, the channel trajectory is extended to the point of maximum elevation in the catchment along the steepest path. Base level is locally defined as the outlet elevation for the catchment, z=0. The specific area or relative frequency $f_\phi(\phi)$, is now defined as the fraction of total area dF_ϕ associated with an increment of elevation change $d\phi$, which can be related to the projected distance ds along the channel $\phi=z(s)$. The distribution $f_\phi(s)$ is given by

$$f_\phi(s) = f_\phi[z(s)]\left|\frac{dz(s)}{ds}\right| \qquad (24)$$

The specific area for the orthogonal trajectories $f_\psi(\psi)$, is also be defined as in (24). In terms of watershed geometry, $f_\phi(s)$ or $f_\psi(s)$ represent the relative frequency or area per unit change in length along the channel. Thus f(s) is a measure of the width or bounding shape of the watershed relative to the channel. The characteristic shape of the catchment or subcatchment enclosing the longest channel is now approximated by the pair of shape functions, the characteristic shape $f_\phi(s)$ and characteristic elevation $\phi=z(s)$. However, there is no characteristic shape for hillslopes, since a channel is not enclosed by the hillslope. We use similarity arguments are used to construct the characteristic shape of the hillslope.

The perspective of landform 'similarity' was well described in a paper by Strahler (1958), where he stated; "Systems of landforms involving the same geologic processes and materials are generally recognized to possess a considerable degree of similarity. Indeed

the classification of landforms depends on this...". Qualitatively, the attributes of landform pattern and similarity imply an invariance with respect to scale of measure. For example, in small watersheds it is often the case that soil and colluvium tend to be thicker near the stream than on the ridges, and that the water table tends to reflect a subdued image of the terrain or bedrock. This pattern suggests a local form of scaling which preserves the spatial relationship of field observations (soil thickness) with respect to natural boundary conditions (e.g. ridge and stream, mountain and valley). Duffy, et al (1991) proposed a local rescaling of topographic trajectories to define a unit hillslope. Each trajectory is scaled by its overall height and distance from ridge to stream. The process of rescaling the flow geometry and corresponding hydrologic measurements, leads to delineation of a soil moisture and saturated storage envelope, and to an empirical analysis of the storage-flux dynamics of the hillslope.

In general this type of scaling is referred to as self-affine, as opposed to self-similar, since the invariance requires both vertical and horizontal scaling ratios. For a self-affine surface we can say that for any two trajectories $z(s_1)$and $z(s_2)$, the increments of elevation and map distance are proportional but with different scale ratios

$$dz_1 = \lambda' dz_2 \quad \text{and} \quad ds_1 = \lambda'' ds_2$$

where λ' and λ'' represent scale ratios for the vertical and map plane respectively and $ds^2=dx^2+dy^2$. This transformation is used to preserve the relative position of field measurements with respect to boundary conditions along a path, and to project sparce and scattered field data onto a smooth curve, thereby reducing the dimensionality of the hillslope from three to two. Figures 2.3 illustrates the concept of a unit hillslope, where $z_0(s)$ represents the rescaled surface elevation trajectories, $z_1(s,t)$ the rescaled location of the water table, and $z_2(s)$ the corresponding bedrock position. Note that map distance and elevation are scaled by overall change for each trajectory Δs and Δz respetively, $s=s'/\Delta s$ $(0\leq s\leq 1)$ $z=z'/\Delta z$, $(0\leq z(s)\leq 1)$. The z(s)'s are represented by polynomial shape functions, and a(t) and b(t) are length scales indicating the upslope penetration of the subsurface saturated region and the surface-saturation region respectively. The corresponding conditional hypsometric relation defines the relative divergence/convergence of the bounding trajectories in the map plane. In section 2.4 a power law-type hypsometric distribution is fit to the Shale Hills data.

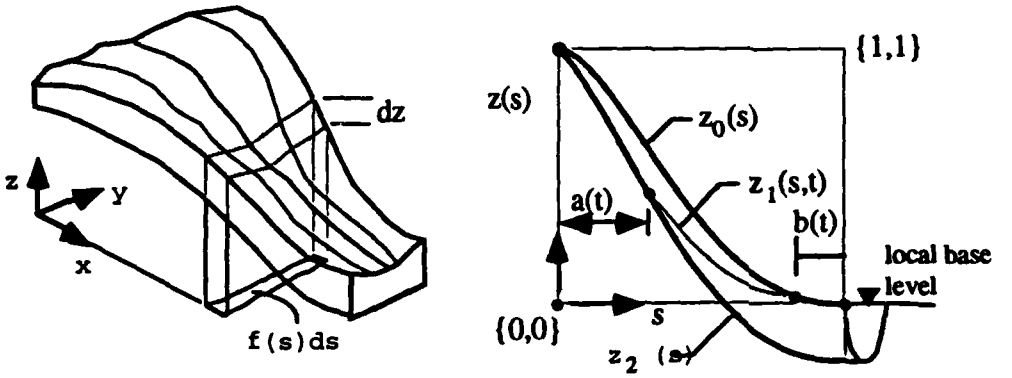

Figure 2.3. Converging hillslope trajectories defining a region of local similarity. Similarity is tested by rescaling each trajectory by its overall height and length to form a unit hillslope $z_0(s)$ trajectory. The region of similarity has trajectories of the same unit shape. The corresponding rescaled water table, bedrock, partial-area length scale, and the upslope penetration of the saturated region is indicated.

2.3 The Hypsometric Integral

A measure of volume or fractional volume of land mass above local base level is determined by integrating the hypsometric distribution $F(\phi)$, referred to as the hypsometric integral I,

$$I = 1 - \int_0^1 F(\phi)d\phi. \qquad (25)$$

From the method of derived distributions (24), the volume intergation may be applied to the shape functions for the land surface, water table and bedrock surface ($z_0(s)$, $z_1(s,t)$, $z_2(s)$), which leads to

$$I_0 = 1 - \int_0^1 F_0(s)ds \qquad (26)$$

$$I_1(t) = 1 - \int_0^1 F_1(s,t)ds \qquad (27)$$

$$I_2 = 1 - \int_0^1 F_2(s)ds \qquad (28)$$

The differential volumes I_0-I_2 and I_1-I_2 represents the volume of soil and the saturated volume over the hydrologic unit.

2.4 A Model for Hypsometry

In the previous section probability arguments are related to watershed hypsometry. It was noted that the problem of evaluating the local hypsometric relation for a hillslope or subcatchment becomes an evaluation of the joint distribution of elevation and flow trajectories. To demonstrate, a hypsometric distribution is proposed of the form

$$F(x) = \frac{(1+a)x^{\alpha}}{(a+x^{\beta})}; \quad (0 \le x \le 1);\ (\alpha \ge \beta \ge 1) \qquad (29)$$

where x represents the normalized random variable, and the distribution is defined for the unit interval ($0 \le x \le 1$). The specific area or density f(x) is given by

$$f(x) = \frac{(1+a)\alpha\, x^{\alpha-1}}{a+x^{\beta}} - \frac{(1+a)\beta\, x^{\alpha+\beta-1}}{(a+x^{\beta})^2} \qquad (30)$$

The flexibility of (29) and (30) for describing watershed shape is illustrated in Figure 2.4. The function captures a wide range of hypsometric shapes ranging from uniformly distributed regions (rectangular), to regions with a large fraction of area at high or low elevation.

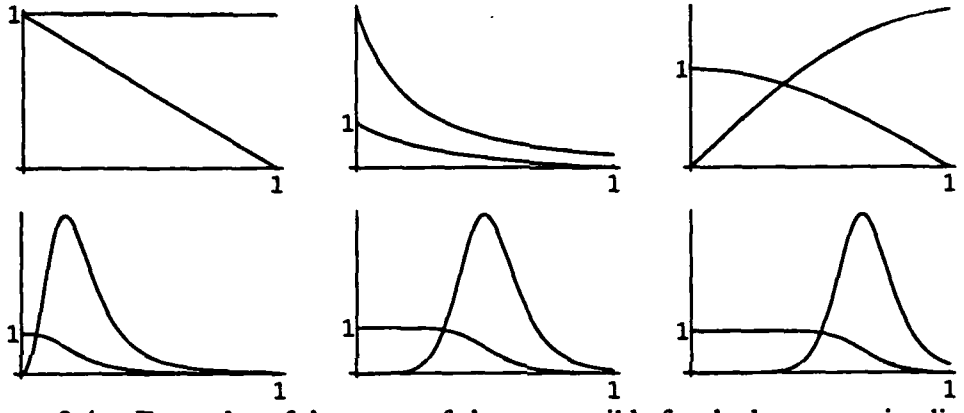

Figure 2.4. Examples of the range of shapes possible for the hypsometric distribution 1-F(x) and f(x) from equation (29) and (30). From the top row and moving left to right the parameters are: {{α,β,a}}= {{1.,1.,200.},{1.,1.,.4},{2.,2.,4.},{3.,3.,.01},{7.,7.,.01}, {10.,10.,.02}}.

The topographic shape function z(s) can be represented as a polynomial in s

$$z(s) = \sum_{i=0}^{m} a_i s^i \qquad (31)$$

For the Shale Hills watershed 2, z(s) was fit to a third order polynomial

$$\hat{z}(s) = 1.027 - 2.738s + 2.828s^2 - 1.128s^3 \qquad (32)$$

The hypsometric relations $1\text{-}F_f(\phi)$ and $1\text{-}F_y(\psi)$ are given in Figure 2.5. The joint distribution $F(\phi,\psi)$ is shown in Figure 2.6.

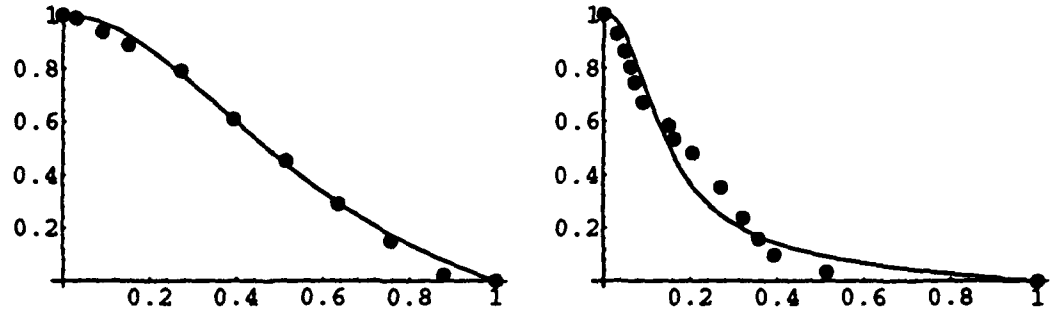

Figure 2.5. Hypsometric relationship for Shale Hills and the fitted model eq. (25) $1\text{-}F_{\phi}(\phi)$ ($a=2,\alpha=2,\beta=0.4$) and $1\text{-}F_{\psi}(\psi)$, ($a=0.009,\alpha=2.4,\beta=2.3$).

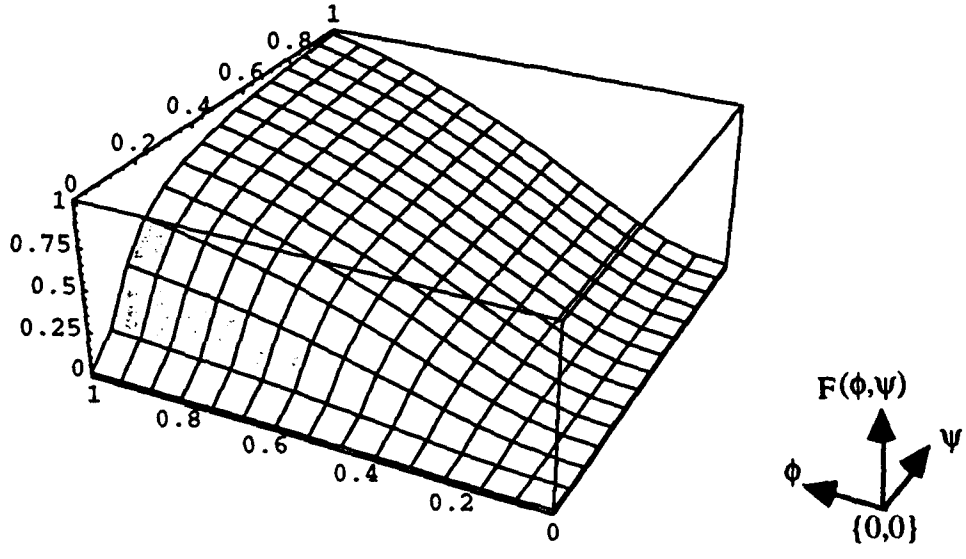

Figure 2.6. The joint distribution $F(\phi,\psi)$ for the Shale Hills watershed determined for the hypsometric ϕ–ψ relations shown in Figure 2.5.

The density $f_{\phi}(\phi)$ and conditional density $f_{\phi}(\phi|\Delta\psi)$ or width distribution for the hillslopes in the region adjacent to channel elevation ($0.2 \le z \le 0.5$) is shown in Figure 2.7.

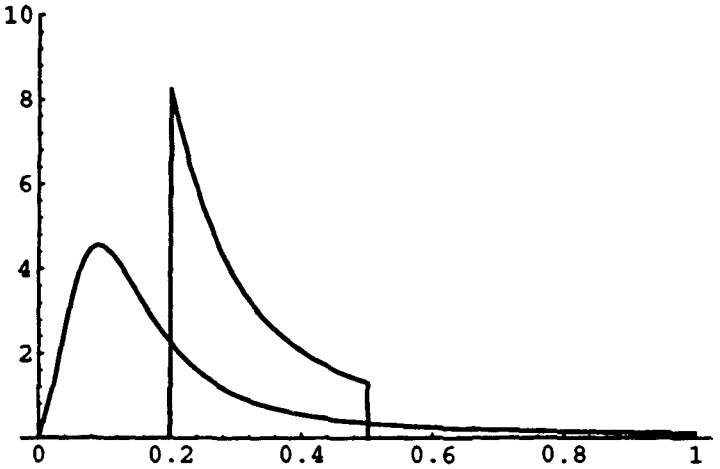

Figure 2.7. The density $f_\phi(\phi)$ and conditional density $f_\phi(\phi|\Delta\psi)$ for Shale Hills for hillslopes contributing to the normalized stream reach interval, $0.2 \le z(s) \le 0.5$.

2.5 Deriving the Dynamical System at the Hillslope Scale

In this section the hypsometric distribution is used to derive the dynamical system for space-averaged state variables at the hillslope scale. Consider the conservation equation for subsurface flow of moisture in the hillslope geometry of Figure 2.3.

$$\frac{\partial \Theta}{\partial t} + \nabla \cdot \vec{q}' = 0 \qquad (33)$$

where $\Theta'(s,z,t) = \theta(s,z,t)\, f_\phi(s|\Delta\psi)$ represents the volumetric moisture per unit area in the $\{s,z\}$ plane, θ is moisture content $[L^3/L^3]$, $f_\phi(s|\Delta\psi)$ is the conditional density for relative width of the hillslope, and $\vec{q}'(s,z,t) = \{q'_s, q'_z\} = \vec{q}(s,z,t)\, f_\phi(s|\Delta\psi)$ is the volumetric Darcy flow per unit area. Vertical integration of (33) is performed over a column of porous media

$$\frac{\partial}{\partial t}\int_{z_2}^{z_0} \Theta'\, dz = \int_{z_2}^{z_0}\left(\frac{\partial q'_s}{\partial s} + \frac{\partial q'_z}{\partial z}\right) dz. \qquad (34)$$

The integration is carried out in two intervals, below and above the water table $z_2(s) \le z \le z_1^-(s,t)$ and $z_1^+(s,t) < z \le z_0(s)$, respectively

$$\frac{\partial}{\partial t}\int_{z_2}^{z_1^-} \Theta'\, dz + \frac{\partial}{\partial t}\int_{z_1^+}^{z_0} \Theta'\, dz = \frac{\partial \eta(s,t)}{\partial t} f_\phi(s|\Delta\psi) + \frac{\partial \gamma(s,t)}{\partial t} f_\phi(s|\Delta\psi) \qquad (35)$$

where $\eta(s,t)$ and $\gamma(s,t)$ are vertically averaged state variables for the saturated and unsaturated depth of water (see Fig. 2.8). Applying Liebnitz rule to the right hand side of (34) yields

$$\int_{z_2}^{z_1^-}\left(\frac{\partial q_s'}{\partial s}+\frac{\partial q_z'}{\partial z}\right)dz+\int_{z_1^+}^{z_0}\left(\frac{\partial q_s'}{\partial s}+\frac{\partial q_z'}{\partial z}\right)dz=$$

$$\frac{\partial q_\eta'}{\partial s}+\frac{\partial q_\gamma'}{\partial s}-q_\eta'|_{z_1^-}\frac{\partial z_1^-}{\partial s}+q_\eta'|_{z_2}\frac{\partial z_2}{\partial s}-q_\gamma'|_{z_0}\frac{\partial z_0}{\partial s}+q_\gamma'|_{z_1^+}\frac{\partial z_1^+}{\partial s}$$

$$+q_z'|_{z_0}-q_z'|_{z_1^+}+q_z'|_{z_1^-}-q_z'|_{z_2} \qquad (36)$$

where

$$q_\eta'=\int_{z_2}^{z_1^-}q_s'dz \text{ and } q_\gamma'=\int_{z_1^+}^{z_0}q_s'dz. \qquad (37)$$

The final integration is performed over the length of the unit hillslope ($0\le s\le 1$). Substituting for the primed quantities $\Theta'(s,z,t)=\theta(s,z,t)\,f_\phi(s|\Delta\psi)$ and $\bar{q}'(s,z,t)=\bar{q}(s,z,t)\,f_\phi(s|\Delta\psi)$ the unsaturated and saturated storage terms become

$$\frac{\partial}{\partial t}\int_{s=0}^{1}\eta(s,t)\,f_\phi(s|\Delta\psi)ds+\frac{\partial}{\partial t}\int_{s=0}^{1}\gamma(s,t)\,f_\phi(s|\Delta\psi)ds= \qquad (38a)$$

$$+\int_{s=0}^{1}\frac{\partial q_\eta'}{\partial s}ds+\int_{s=0}^{1}\frac{\partial q_\gamma'}{\partial s}ds \qquad (38b)$$

$$-\int_{s=0}^{1}q_\eta'|_{z_1^-}\frac{\partial z_1^-}{\partial s}ds+\int_{s=0}^{1}q_\eta'|_{z_2}\frac{\partial z_2}{\partial s}ds-\int_{s=0}^{1}q_\gamma'|_{z_0}\frac{\partial z_0}{\partial s}ds+\int_{s=0}^{1}q_\gamma'|_{z_1^+}\frac{\partial z_1^+}{\partial s}ds \qquad (38c)$$

$$+\int_{s=0}^{1}q_z'|_{z_0}ds-\int_{s=0}^{1}q_z'|_{z_1^+}ds+\int_{s=0}^{1}q_z'|_{z_1^-}ds-\int_{s=0}^{1}q_z'|_{z_2}ds \qquad (38d)$$

The equivalent depths of integrated soil moisture $\gamma(s,t)$ and saturated storage $\eta(s,t)$ represent the state variables of interest. Evaluating the integrals in $\eta(s,t)$ and $\gamma(s,t)$ from (38a) yields the conditional spatial mean storage quantities for the hillslope

$$\eta(t|\Delta\psi)=\int_{s=0}^{1}\eta(s,t)f_\phi(s|\Delta\psi)ds. \qquad (39)$$

$$\gamma(t|\Delta\psi)=\int_{s=0}^{1}\gamma(s,t)f_\phi(s|\Delta\psi)ds\,. \qquad (39)$$

Equation (38b) represents the volumetric boundary flux from the soil moisture and saturated storage reservoirs at the stream, $q_\eta'+q_\gamma'=q(t)$. As a first approximation we assume that horizontal flow components in the unsaturated zone are small $q_\gamma'|_{z_1^+}=q_\gamma'|_{z_0}\approx 0$, $q_\eta'|_{z_1^-}\approx q_\eta'|_{z_2}$ and $\frac{\partial z_1^-}{\partial s}\approx\frac{\partial z_2}{\partial s}$, and thus the terms in row (38c) cancel. The terms in (38d) respectively are: spatially integrated vertical flux evaporation and precipitation, recharge to the saturated zone from soil moisture (r^+), recharge to soil moisture from the saturated zone (r^-), and the flux of water to or from the bedrock (u). The dynamical system for the spatial average storage-flux over the hillslope is now given by

$$\frac{d\eta}{dt}+\frac{d\gamma}{dt}=p-e-r^{+}+r^{-}-q-u \qquad (40)$$

Writing (40) separately, combining surface inputs, and indicating the general dependence of flux quantities on state variables, leads to a two-component state-space form of the model

$$\frac{d\gamma}{dt}=i(\eta,\gamma,p,e,t)-r(\eta,\gamma,t) \qquad (41)$$

$$\frac{d\eta}{dt}=r(\eta,\gamma,t)-q(\eta,\gamma,t) \qquad (42)$$

where $i(\eta,\gamma,p,e)$ is surface infiltration rate , or that flux which infiltrates the soil less evaporation, $r(\eta,\gamma)$ is the recharge rate per unit surface area to/from the water table, and $q(\eta,\gamma)$ the volumetric subsurface runoff per unit area. Equations (41-42) are referred to as the integral-balance model for the coupled unsaturated-saturated system. The state variables are defined locally in the subregion $\Delta\psi$. Figure 2.8 illustrates the relationship for soil moisture θ and the vertically integrated soil moisture depth γ, and the saturated thickness η for an increment of hillslope length ds with surface elevation $z_0(s)$.

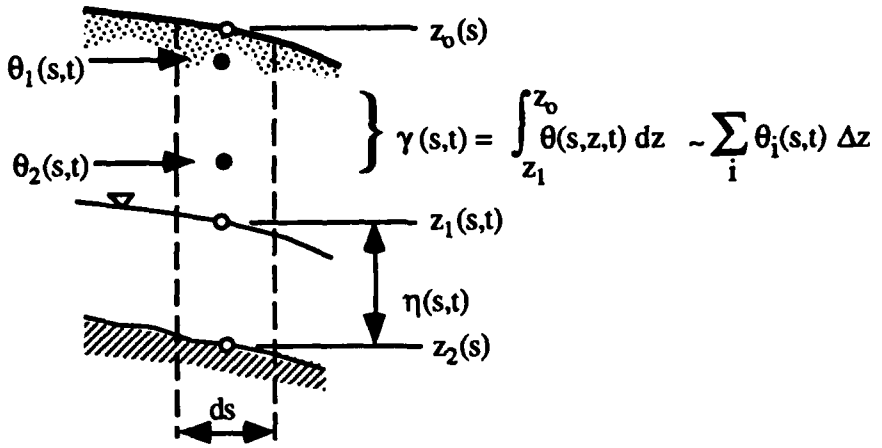

Figure 2.8 The soil moisture depth function $\gamma(s,t)$ and the saturated thickness $\eta(s,t)$ are defined for a column of porous material on the hillslope

3 SOIL MOISTURE NUMERICAL EXPERIMENTS

Two and three dimensional numerical experiments were conducted based on the theory of unsaturated-saturated flow in a porous medium. The integrated storage-flux constitutive relationships $q(\eta)$, $r(\gamma, \eta)$ and the partial-area length scale $b(\eta)$ were determined as a function of slope gradient (H/L), slope curvature/shape, aspect ratio (d/L), the degree of topographic convergence or divergence, soil type, and boundary conditions. Parameterization is performed by fitting a polynomial to each steady-state relationship $q(\eta)$, $r(\gamma, \eta)$, and $s(\eta)$. The goal of the experiment is to construct the functional form of storage-flux and surface saturation relationships in the dynamical model as discussed in chapter 2, and to generally establish the nonlinear structure of spatially integrated state variables.

3.1 Richards Equation and Solution

The partial differential equation describing this flow is known as Richards' equation

$$C(\psi)\frac{\partial \psi}{\partial t} = \nabla \cdot (K(\psi) \cdot (\nabla \psi + \nabla z)) \qquad (43)$$

where ψ is the soil-water pressure head, $C(\psi)=\partial\theta/\partial\psi$ is the specific moisture capacity, θ is moisture content, $K(\psi)$ is the nonhysteretic unsaturated hydraulic conductivity, and z is the elevation head or gravity contribution. The Richards equation was solved by the finite element code, FEMWATER of Yeh (1987), and this reference gives details of the numerical solution methodology based on the Galerkin finite-element approximation as well as an input guide for the program. An example of element mesh design using a few quadrilateral elements is illustrated in Figure 3.1. For most cases a uniform element mesh distribution was used. The number of elements for each simulation is given in Table 3.4.

The finite-element formulation results in a nonlinear matrix equation that needs to be solved by means of iterative technique. For example, the following nonlinear matrix is obtained from the formulation: $[C(\psi)]\{\psi\} = \{L\}$, where [C] is the coefficient matrix, ψ is the dependent vector (pressure head), and {L} is the load vector. First, an initial guess of for $\{\psi\}$ is made. From this estimate, the nonlinear matrix is linearized and solved by Gaussian elimination. New values for $\{\psi\}$ are acquired using a weighted average between each solution and previous values for $\{\psi\}$. This procedure is $\{\psi^{j+1}\} = \{\psi\} + (1\text{-}w)\{\psi^j\}$, where j is the iterative index, and w is the iteration parameter. Under-relaxation is

0<w<1, exact relaxation is w = 1, and over-relaxation is w >1. For all runs, the under-relaxation option to Picard's iteration scheme was the most efficient for convergence of the nonlinear matrix. The parameter w varied from 0.1 to 0.5 depending on the case.

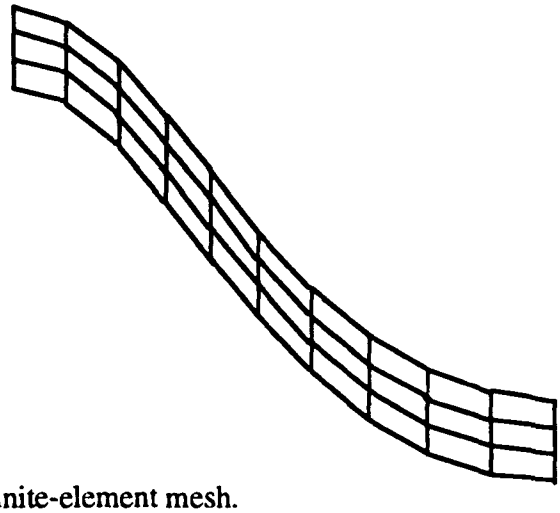

Figure 3.1. A quadrilateral finite-element mesh.

In the mass-balance routine, FEMWATER calculates total moisture volume using Gaussian quadrature integration technique. Since total moisture volume is a sum of unsaturated water volume and saturated water volume, the integral unsaturated water storage was calculated as $\gamma = \theta_{total} - \eta$.

3.2 Flow Geometry and Boundary Conditions

The shapes and boundary conditions considered in the numerical experiments are given in Figures 3.2 and 3.3. The shapes chosen here are to some degree arbitrary, but are considered to be representative of hillslope profiles in humid-temperate regions. A letter (A, B, C, D, and E) is assigned to indicate each shape which will be used throughout the text. Table 3.1 defines the surface and bedrock shape functions that appear in Figure 3.2.

For all hillslope cases, the impermeable boundary is assumed to be B-C. The A-B and C-D are symmetry boundary conditions such that no flow crosses these boundaries. The constant pressure head condition at the point D represents a perennial stream. The infiltration and seepage boundary conditions coexist on the soil surface (A-D), and the position of the seepage face is not known a priori. The boundary condition is tested during each solution (see Yeh, 1987).

For the horizontal stream-aquifer system (shape E), the no-flow boundary condition was imposed on the boundaries through A-B-C and D-E. A fully penetrating stream was assumed on the boundary C-D, and a constant pressure head represents the stream. On the land surface A-E, a variable boundary condition was specified to handle the infiltration rate. A variable condition means a mixed boundary condition for Neuman (flux) type and Dirichlet type. For each iteration, either Neumann type or Dirichlet type is determined by flux balance consideration between rainfall flux and Darcy flux.

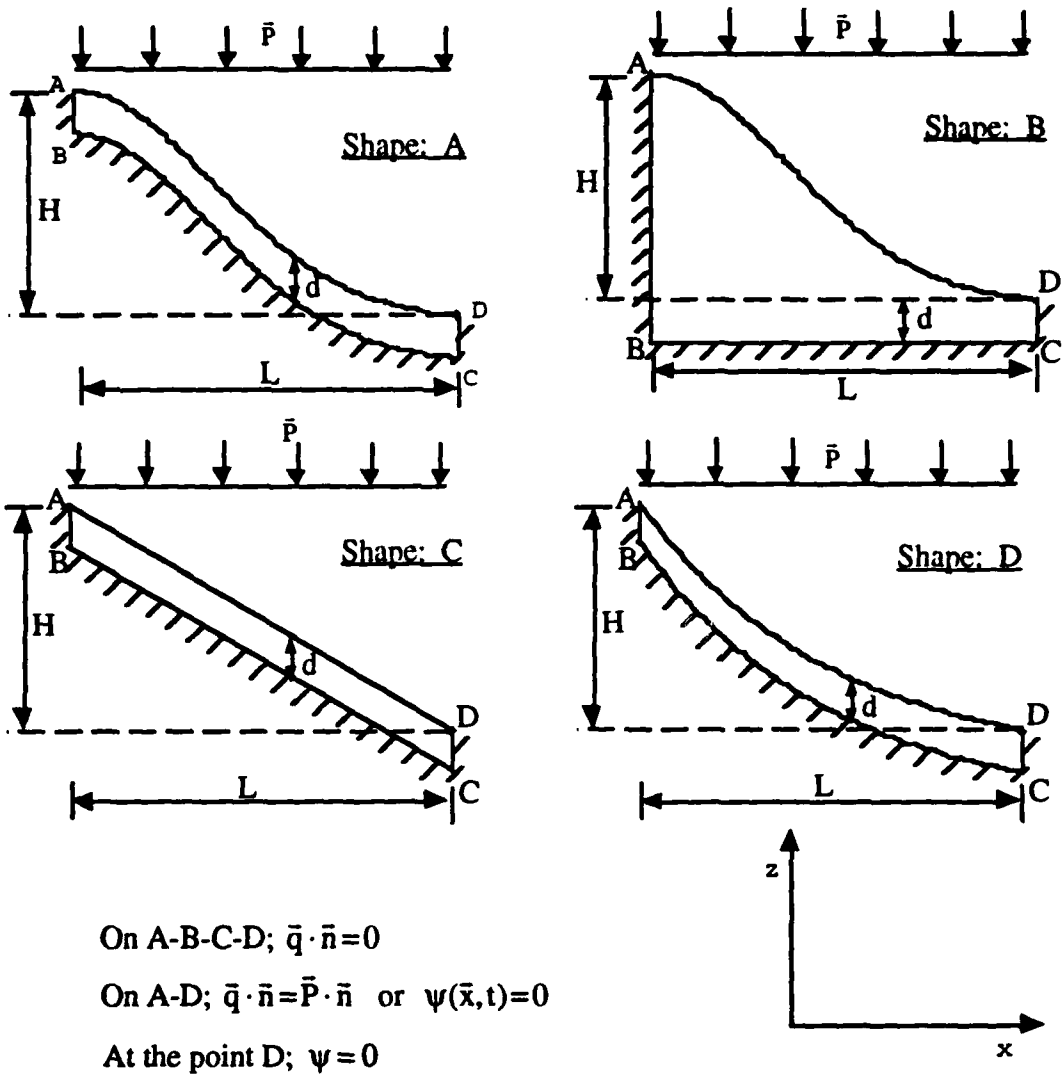

On A-B-C-D; $\vec{q} \cdot \vec{n} = 0$

On A-D; $\vec{q} \cdot \vec{n} = \vec{P} \cdot \vec{n}$ or $\psi(\vec{x},t) = 0$

At the point D; $\psi = 0$

Figure 3.2. Hillslope shapes and boundary conditions ($\vec{p}$ = rainfall flux vector, $\vec{q}$ = Darcy flux vector, and $\vec{n}$ = unit normal vector).

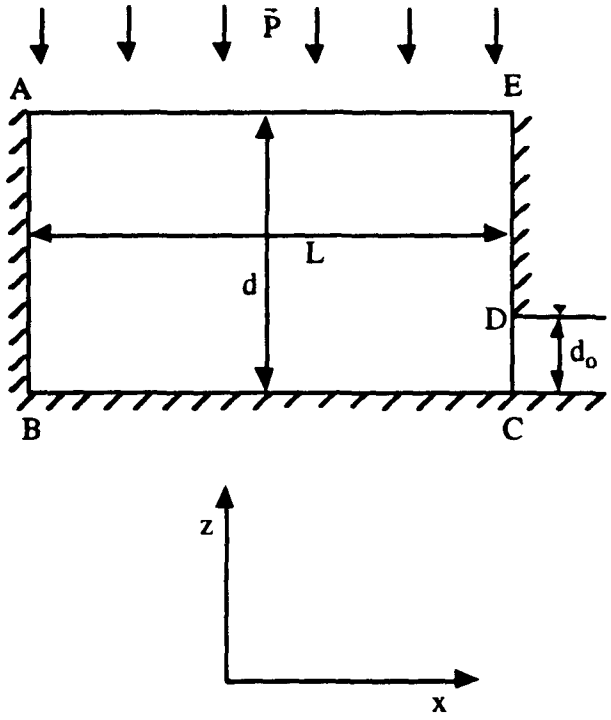

Shape E

On A-B-C and D-E; $\vec{q} \cdot \vec{n} = 0$

On A-E; $\vec{q} \cdot \vec{n} = \vec{P} \cdot \vec{n}$ or $\psi(\vec{x},t) = 0$

On C-D; $\psi + z = 0$

Figure 3.3. A horizontal aquifer shape and boundary conditions ($\vec{p}$ = rainfall flux vector, $\vec{q}$ = Darcy flux vector, and $\vec{n}$ = unit normal vector).

Table 3.1. Surface and bedrock shape functions.

Shape	Surface shape function, $z_0(x)$
A	$\frac{H\{e^{[4-4(\frac{x}{L})^2]}-1\}}{e^4-1}$
B	"
C	$H(1-\frac{x}{L})$
D	$\frac{H\{e^{[2-2(\frac{x}{L})]}-1\}}{e^2-1}$

Table 3.1 (cont.)

Shape	Bedrock shape function, $z_2(x)$
A	$\frac{H\{e^{[4-4(\frac{x}{L})^2]}-1\}}{e^4-1}-d$
B	$-d$
C	$H(1-\frac{x}{L})-d$
D	$\frac{H\{e^{[2-2(\frac{x}{L})]}-1\}}{e^2-1}-d$

3.3 Soil Texture and Hydraulic Properties

In general, soil hydraulic properties vary with moisture, soil texture and soil structure. The numerical experiments were conducted for four soils (Guelph Loam, Plainfield Sand, Yolo Clay, and Touchet Silt Loam G.E.3). Soil hydraulic properties for these soils reported in Elrick et al. (1990) and van Genuchten (1980) are reproduced below. The unsaturated hydraulic conductivity $K(\psi)$ for Guelph Loam, Plainfield Sand, and Yolo Clay, is given by

$$K(\psi)=K_s \exp(\alpha\psi)$$

and for Touchet Silt Loam G.E.3

$$K(\psi)=K_s\frac{\{1-(a\psi)^{n-1}[1+(a\psi)^n]^{-m}\}^2}{[1+(a\psi)^n]^{m/2}}$$

where K_s is the saturated hydraulic conductivity, and α , a, n, m=1-1/n are fitting parameters. The relationship between soil moisture content and matric potential is given for Guelph Loam, Plainfield Sand, and Yolo Clay, as

$$\theta=\frac{p_1p_2}{[p_2+|\psi|^{p_3}]}+p_4 \qquad \psi<0$$

and for Touchet Silt Loam G.E.3, as

$$\theta=\theta_r+(\theta_s-\theta_r)\Theta,\quad \Theta=\left[\frac{1}{1+(a\psi)^n}\right]^m \qquad \psi<0$$

Soil water capacity relations $C(\psi)$ are obtained by differentiating the water retention curve. The for Guelph Loam, Plainfield Sand, and Yolo Clay have the form

$$C(\psi)=\frac{d\theta}{d\psi}=\frac{p_1p_2p_3|\psi|^{(p_3-1)}}{[p_2+|\psi|^{p_3}]^2} \qquad \psi<0$$

and the Touchet Silt Loam G.E.3 is

$$C(\psi)=\frac{d\theta}{d\psi}=\frac{-a\,m(\theta_s-\theta_r)}{1-m}\Theta^{1/m}(1-\Theta^{1/m})^m. \qquad \psi<0$$

Table 3.2 summarizes parameter values for each relationship. Figure 3.4 illustrates soil moisture retention and relative hydraulic conductivity curves as a function of pressure head.

Table 3.2. The parameter values in the $C(\psi)$ and $K(\psi)$ relations.

soil type	K_s (m/hr)	θ_S	α (1/m)	P_1	P_2	P_3	P_4
Guelph Loam	0.013212	0.523	3.36	0.243	0.421	2.0	0.28
Plainfield Sand	0.12384	0.477	13.06	0.377	0.00154	4.0	0.1
Yolo Clay	0.0004428	0.499	1.88	0.259	0.609	1.5	0.24

soil type	K_s (m/hr)	θ_S	θ_r	a	n
Touchet Silt Loam G.E.3	0.12625	0.469	0.19	0.243	0.421

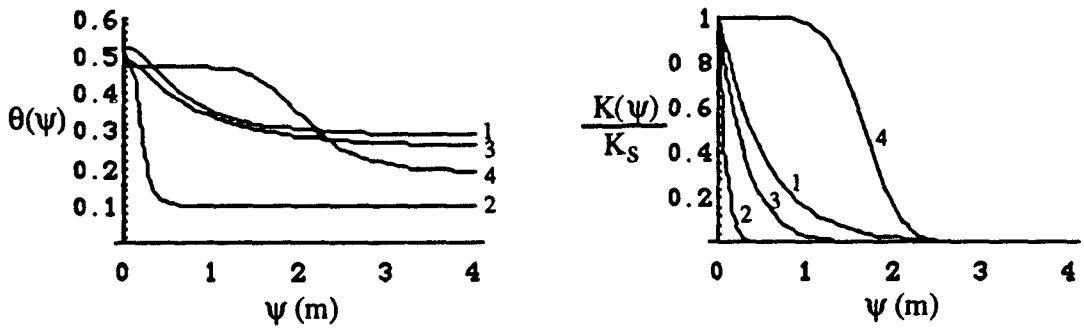

Figure 3.4. Water retention function $\theta(\psi)$ and relative conductivity function $K(\psi)/K_S$ for Guelph Loam (1), Plainfield Sand (2), Yolo Clay (3), and Touchet Silt Loam G.E.3 (4).

3.4 Equilibrium Experiments

Equilibrium numerical experiments were conducted to evaluate the steady-state (constant forcing) constitutive relations for the spatially-integrated state variables (η and γ) and the relation to system fluxes. The partial area length scale, or region of saturation overland flow was also determined. The experiments were comprehensive in that for each

geometry and parameterization, constant rainfall rates were specified to cover all possible cases of soil moisture and saturated storage, from very dry and entirely unsaturated to complete saturation. Table 3.3 lists physical information and Table 3.4 describes computational information for 20 simulated cases.

Table 3.3. Steady-state simulation cases.

case	cross section shape	plan shape	H/L	d/L	soil type	ρ/L
1	A	parallel	0.25	0.025	Guelph Loam	∞
2	"	"	0.1	"	"	"
3	"	"	0.4	"	"	"
4	"	"	0.7	"	"	"
5	"	"	0.25	0.01	"	"
6	"	"	"	0.04	"	"
7	C	"	"	0.025	"	"
8	D	"	"	"	"	"
9	B	"	"	"	"	"
10	"	"	"	0.1	"	"
11	A	"	"	0.025	Plainfield Sand	"
12	"	"	"	"	Yolo Clay	"
13	"	"	"	"	Touchet Silt Loam G.E. 3	"
14	E	"	NA	0.05	Guelph Loam	"
15	"	"	"	"	Touchet Silt Loam G.E.3	"
16	A	hollow	0.25	0.025	Guelph Loam	1
17	"	"	"	"	"	2
18	"	spur	"	"	"	1
19	"	"	"	"	"	2
20	A	parallel	"	"	"	∞

Note: L = slope length = 100 m and H = slope height. NA = not applicable.

Table 3.4. Computational information for steady-state cases.

case	nodes	dx (m)	dx/dz	w
1	2211	0.5	2	0.25
2	"	"	"	"
3	"	"	"	"
4	"	"	"	0.15
5	"	"	"	0.25
6	"	"	"	"
7	"	"	"	"
8	"	"	"	"
9	3276	"	"	0.1
10	3861	"	"	"
11	4221	0.5	4	0.15
12	2211	"	2	0.25
13	4221	"	4	0.15
14	4141	1.0	2	0.1
15	"	"	"	0.05
16	2211	0.5	2	0.25
17	"	"	"	"
18	"	"	"	"
19	"	"	"	"
20	"	"	"	"

Note: dx = horizontal length of an element, dz = vertical length of an element, w is the iteration parameter for solving a nonlinear matrix equation.

The cross-section shape and symbols in Table 3.3 refers to Figures 3.2 and 3.3.

Changes in slope gradient alone (H/L) were considered in cases 1-4, while other parameters were fixed. For cases 5 and 6, the aspect ratio (d/L) was varied while the remaining parameters were the same as case 1. Cases 7 and 8 examine the effect of different hilllslope shapes (linear and concave). Cases 9 and 10 investigate the role of storage capacity on the flux-storage relationship by changing the depth to bedrock. The effect of soil type was examined in cases 11-13, and cases 14 and 15 simulate a horizontal hillslope system with different soil types.

Cases 16-19 show the effect of convergence or divergence in plan or map view, while the remaining parameters follow case 1. Figure 3.5 shows the converging and diverging sections for these cases. The degree of convergence or divergence was controlled by the parameter ρ/L, that is, the ratio of the radius of curvature in the plan view (ρ) to the hillslope length (L). Since a circular converging or diverging domain is considered, ρ is simply the radius of a circle. For other planametric shapes, ρ can be defined as the inverse of the magnitude of curvature vector and depends on position. Notice that ρ/L approaches infinity for a parallel hillslope, or the hillslope length is small relative to ρ. The ratio $\rho/L=1$ is the other limiting case, and the range is $1< \rho/L <\infty$. For each plan shape, two cases were examined, $\rho/L=1$ and $\rho/L=2$. Solutions were obtained using axisymmetric coordinates in FEMWATER.

Case 20 tests the effect of the stream boundary condition. Instead of a constant head condition, a seepage face was defined as shown in Figure 3.6. All other parameters remained the same as case 1. Case 1 represents the base case for comparison.

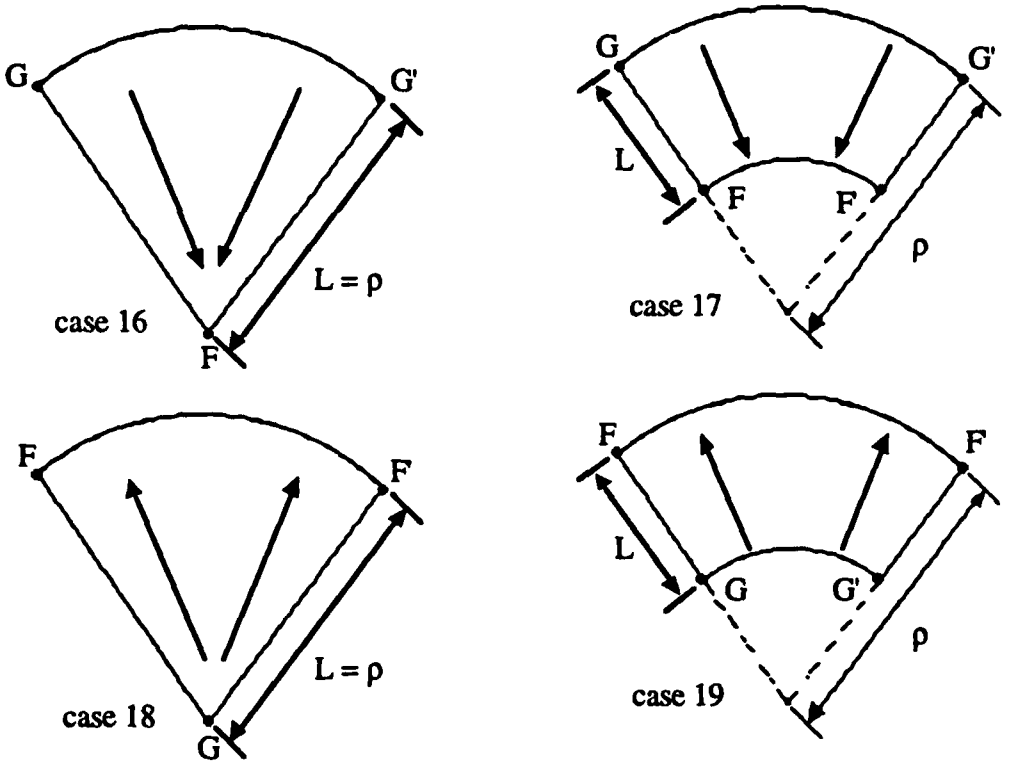

Figure 3.5. Plan view of hollows and spurs (F-F' = stream and G-G' = divide).

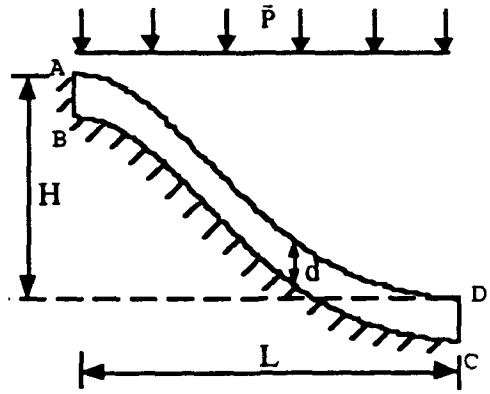

On A-B-C; $\vec{q} \cdot \vec{n} = 0$

On A-D-C; $\vec{q} \cdot \vec{n} = \vec{P} \cdot \vec{n}$ or $\psi(\vec{x},t) = 0$

Figure 3.6. Boundary conditions for case 20.

3.4.1 Saturated Storage-Runoff Relation

Figure 3.7 summarizes the steady-state subsurface outflow or baseflow versus saturated storage, $q(\eta)$ for a complete range of (constant) precipitation rate p, and all cases in Table 3.4. Each point represents a single steady-state solution to the Richards equation for η and q with specified p. A third-degree polynomial was fit to the calculated values of $q(\eta)$. Polynomial coefficients for all cases are summarized in Appendix A.

Note that for steep slopes, the shape of $q(\eta)$ tends to become more convex (case 4). The magnitude of $q(\eta)$ is similar for cases 1, 2, and 3. For dry to moderately wet conditions, a linear $q(\eta)$ can be defined for convex-concave hillslopes, at least for the range of conditions examined here. For steep slopes however, the magnitude of q is a nonlinear function of η.

When the aspect ratio of the hillslope (d/L=soil depth/slope length) is increased, almost no change in the shape of $q(\eta)$ is observed. However, the magnitude of $q(\eta)$ increases rapidly with aspect ratio (cases 1, 5, and 6).

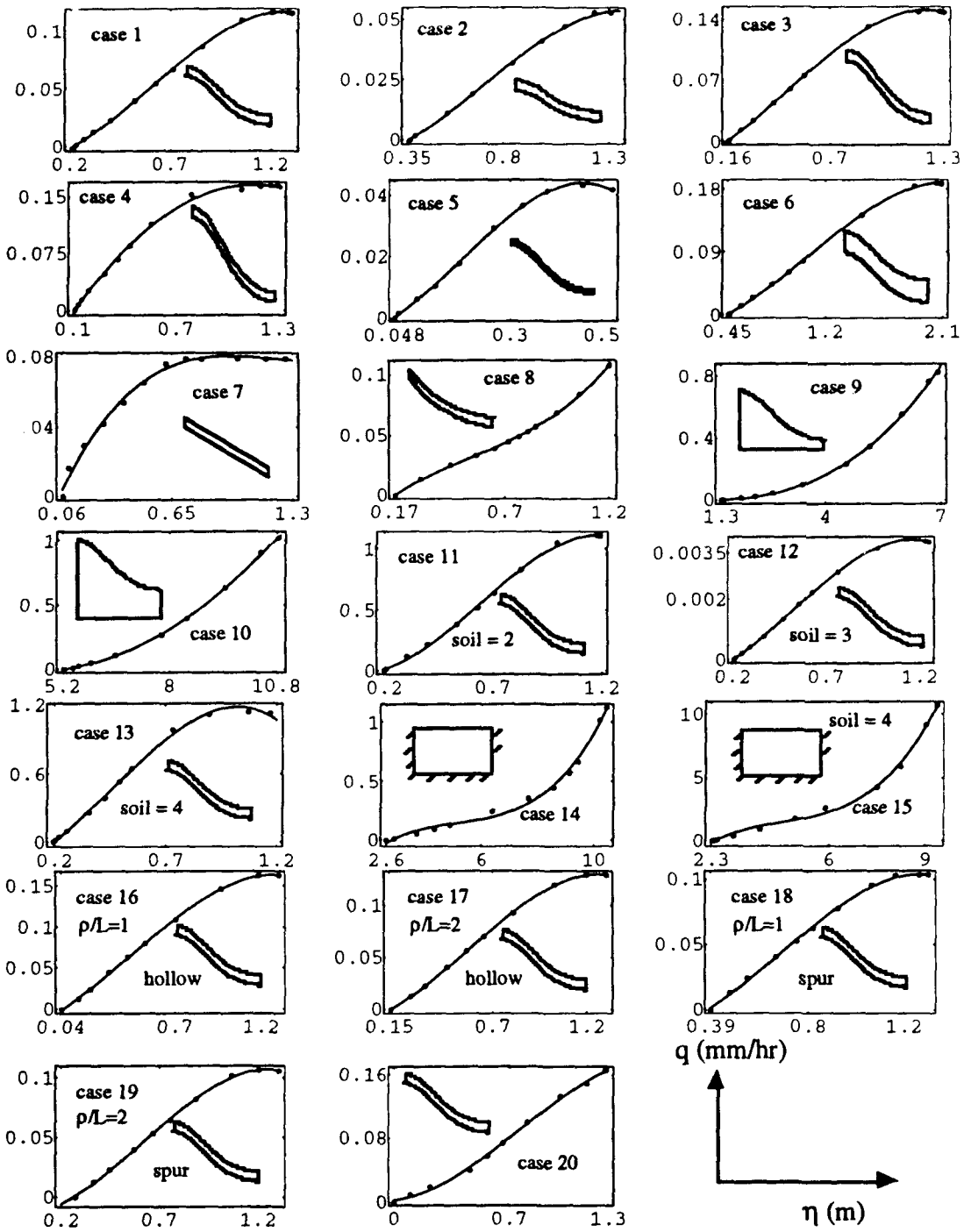

Figure 3.7. Steady-state $q(\eta)$ relationships. Dots were determined from steady-state solutions to Richards equation for a constant rainfall rate. The solid curve is the third degree fitted polynomial. Soil type assumed is soil 2 = Plainfield Sand, soil 3 = Yolo Clay, and soil 4 = Touchet Silt Loam G.E.3. Guelph Loam soil is assumed unless specified. The fitted polynomial is the third-order: $q(\eta) = a_0 + a_1 \eta + a_2 \eta^2 + a_3 \eta^3$.

Hillslope curvature (cases 1, 7, 8) substantially alters the shape of q. The linear slope (case 7) exhibits a concave q-η relationship, while cases 1 and 7 have slightly convex to concave q-n. For the linear slope, q approaches saturation at a lower value of η (η >0.7m), as compared to the convex-concave or concave slopes, indicating the greater efficiency of linear slopes in generating runoff.

When depth to bedrock increases and storage capacity increases, a concave relation for q(η) emerges (cases 9 and 10). The magnitude of q also increases. This relationship could be quite useful in field studies where the storage geometry is unknown. Ando et al. (1983) found a similar relation q(η) in a forested hillslope watershed, and fitted a quadratic polynomial to saturated storage and discharge. As the aspect ratio d/L increases (case 10), the shape of the relationship displays somewhat less concavity and the range of q increases slightly.

The effect of soil type on q(η) was examined for hillslopes in cases 11-13 and for horizontal flow in cases 14-15. For all cases soil type did not affect the basic form of q(η) (cases 1, 11, 12, 13, 14 and 15). However, variations in soil type have a large impact on the magnitude of q. The increase in the magnitude of q was found to be nearly proportional to the increase in saturated hydraulic conductivity for a given aquifer shape.

Cases 16-19 illustrate the effect of topographic convergence and divergence on q(η). As noted previously, topographic convergence or divergence in plan (Figure 3.5) was simulated for an axisymmetric coordinate system. From radial symmetry, the soil moisture gradient is constant along radii from the center of convergence. In order to fairly compare the response with a parallel case, the total hillslope volume for the hollow or spur geometry was made the same as the parallel slope. As might be expected for radial symmetry, the simulations demonstrate the similarity in the shape of q(η), independent of the overall angle of topographic convergence or divergence. For the same η, as ρ/L ratio increases, q decreases for hollow cases, and increases for spur slopes. Also, as the ratio ρ/L increases, the relationship q(η) for hollow or spur approaches the limiting case of a parallel slope (ρ/L = ∞) as expected.

Case 20 displays the effect of boundary condition at the stream. Compared to case 1, the shape of q(η) in case 20 is quite different for dry and very wet moisture conditions, but for the medium wetness range, the two cases exhibit the same linear relationship q(η). The amplitude of subsurface outflow in case 20 is slightly larger than case 1.

3.4.2 Recharge-Soil Moisture-Saturated Storage Relation

With the same series of steady-state simulations, recharge rates were estimated and parameterized in terms of γ and η. Figure 3.8 plots these results for $r(\gamma, \eta)$ and its projection onto three orthogonal planes: r-γ plane, r-η plane, and γ-η plane. The a cubic polynomial was fit to $r(\gamma, \eta)$ and the results are given in the Appendix.

Figure 3.8 shows that r decreases with an increase in γ. The soil moisture γ generally decreases with an increase in η. Both γ-r and γ-η exhibit an inverse relationship over most of the range of rainfall. Recharge r is directly proportional to saturated storage η. This can be interpreted to mean that for an incremental increase n precipitation, the saturated zone will increase at the expense of unsaturated moisture storage. The implication is that γ-η are competitive for the overall storage volume. This is an important structure with major implications to modeling a two-state system. For very low moisture conditions however,, the relationships γ-r and γ-η are direct rather than inverse. Under very dry conditions, we expect both soil moisture and saturated storage to increase. At some critical value of γ-η a threshold is reached, and the relationship becomes inverse as p increases. This effect may be extremely important for explaining the transition from drought to wetter conditions or vice- versa, as the constitutive relation apparently changes form.

The recharge relationship $r(\gamma,\eta)$ exhibits only modest changes in shape and magnitude when the geometry and physical attributes of hillslopes are varied. Chapter 5 will take up this discussion again in the context of model development and parameterization.

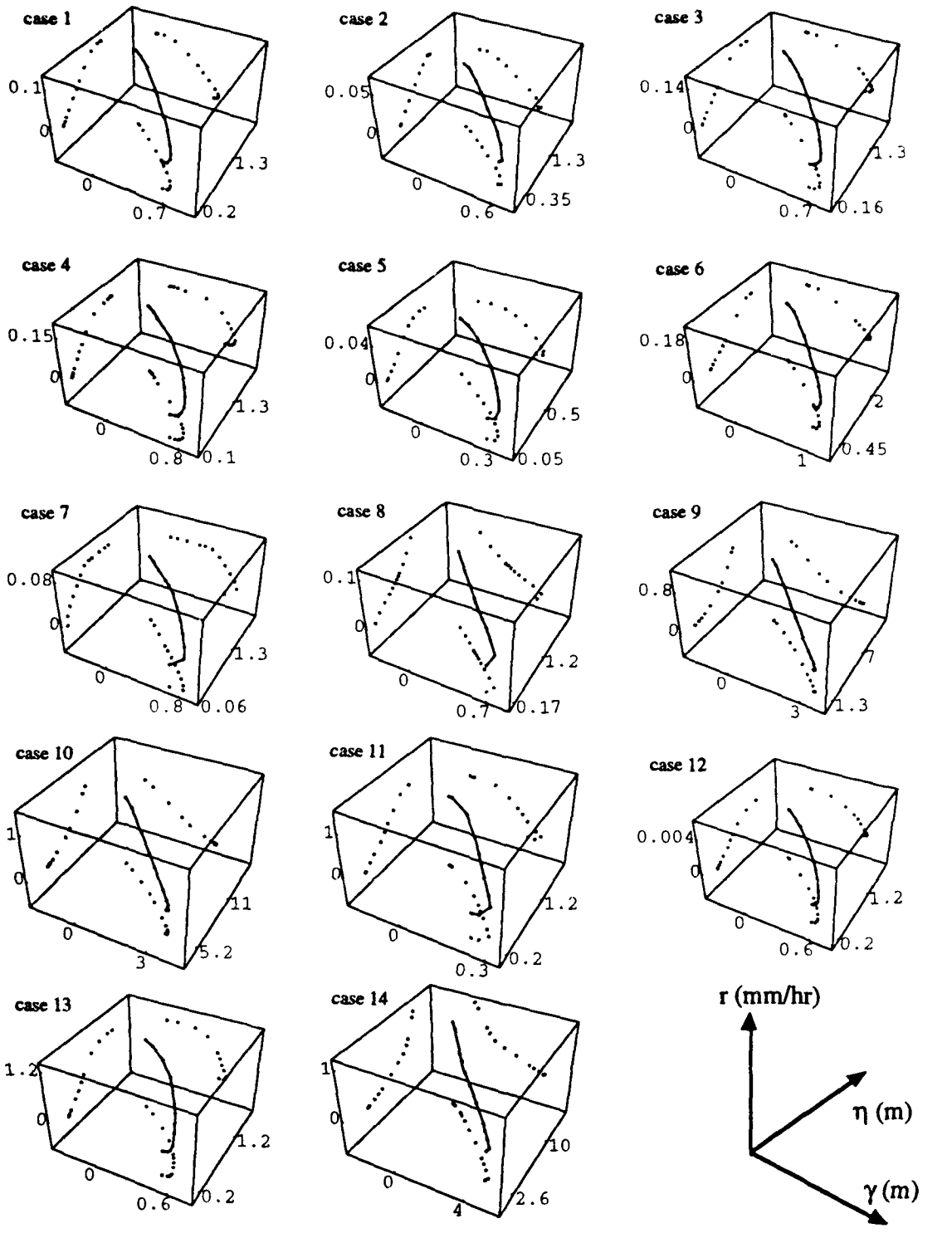

(cont. on next page)

Figure 3.8. Steady-state r(γ,η) relationships for steady-state solutions to the Richards equation (Lee, 1993). The dots represent the steady-state solutions for a given precipitation rate.

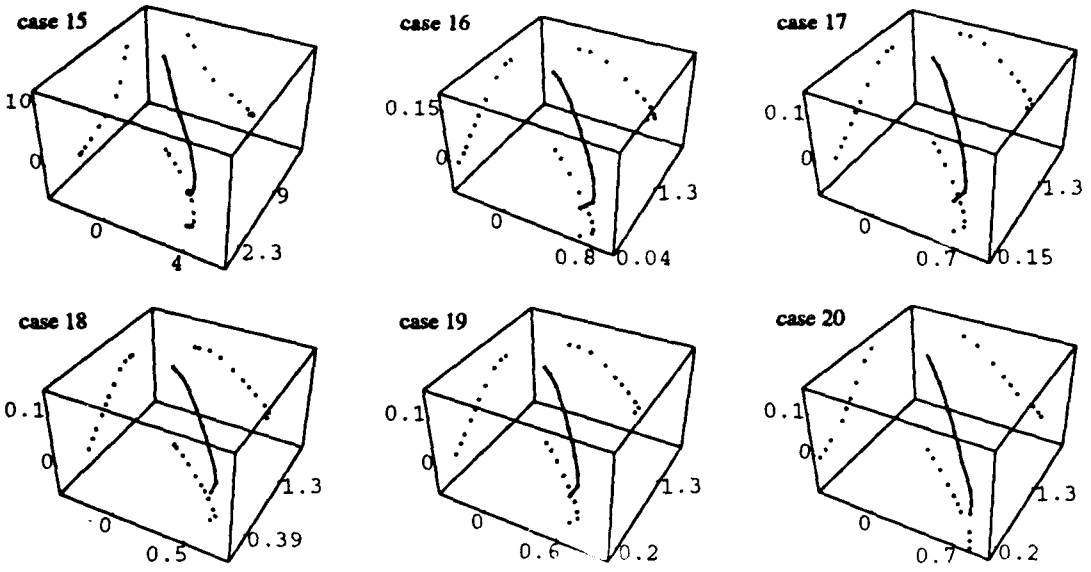

Figure 3.8 (cont.)

3.4.3 Partial Area-Saturated Storage Relation

As defined earlier, b is the length or area fraction of surface saturation for the hillslope. The length scale b was parameterized as a function of the saturated storage (η). In the numerical simulations, b was estimated as the distance over which atmospheric pressure is maintained, as illustrated in Figure 3.9.

Figure 3.10 shows the relationship b-η obtained from the numerical simulations. The parameterization was performed by fitting a third-degree polynomial in η, and results are given in Appendix C.

The effect of relief H/L on b(η) is apparently small (cases 1, 3 and 5), with nearly the same shape and magnitude for all cases. The shape of b(η) between different aspect ratios is similar despite the difference in the scale of η (case 1, case 5, and case 6). The slope curvature has a relatively large effect on the shape of b(η) (case 1, case 7, and case 8). In case 7 (straight slope), b(η) is concave, with b increasing rapidly with η. Over most of the range of η, the magnitude of b for a linear slope is smaller than for concave or convex-concave slopes.

Comparing the effect of soil thickness of cases 9 and 10, we see that the shape of b(η) is similar. However, the penetration distance (b) is much larger than is the case for shallow soils. Soil type has very little impact on the shape and magnitude of b(η), as observed in cases 11, 12 and 13.

The effect of topographic convergence and divergence on the shape and scale of $b(\eta)$ is shown in cases 16-19. For converging slopes (hollow) with $\rho/L = 1$ and 2 (cases 16 and 17), the shape and amplitude of $b(\eta)$ is quite close to the parallel slope (case 1). For diverging slopes (spur) the magnitude of q is reduced near the channel.

Case 20 (boundary condition effect) is similar to case 7 (linear slope), where growth of the zone of saturation is limited until saturated storage is quite high, $\eta > 0.4$. The shape of $b(\eta)$ is concave for both cases. By comparison with case 1, where the boundary condition is constant head or stream stage, the partial area b will increase even at low values of saturated storage.

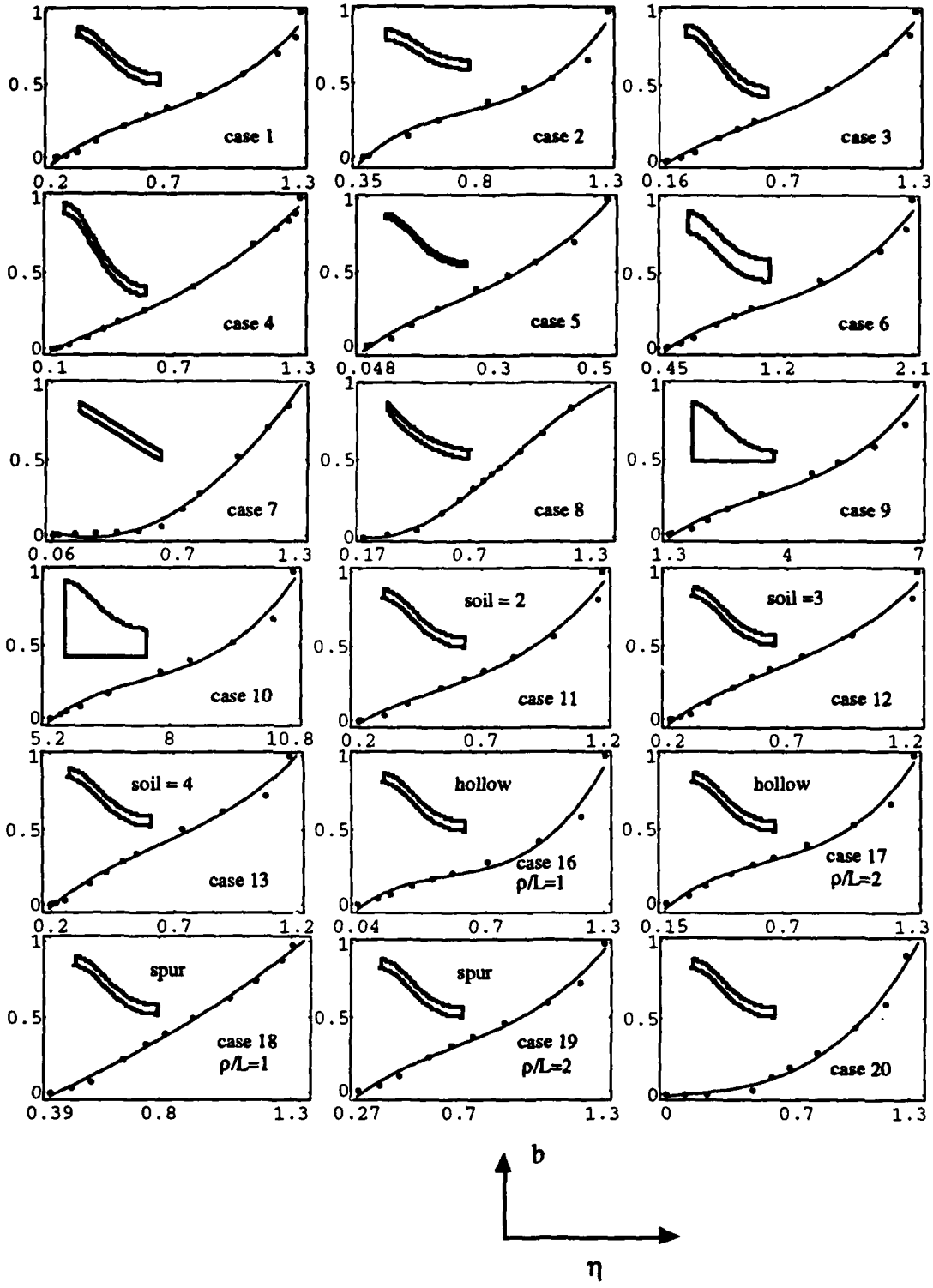

Figure 3.10. Steady-state $b(\eta)$ relationships. Dots were determined from steady-state solutions to Richards equation. The solid curve is the third degree fitted polynomial. Soil type assumed is soil 2 = Plain field Sand, soil 3 = Yolk Clay, and soil 4 = Touchet Silt Loam G.E.3. Guelph Loam soil is assumed unless specified. The fitted polynomial is the third-order: $b(\eta) = a_0 + a_1 \eta + a_2 \eta^2 + a_3 \eta^3$.

3.4.4 Summary of Equilibrium Experiments

The steady-state storage-flux relations $q(\eta)$, $r(\gamma, \eta)$, and $b(\eta)$ were established through numerical experiments with Richards equation for wide range of hillslope geometry and hydraulic properties. The shape of the steady-state $q(\eta)$ relation is mainly affected by the degree of slope gradient, hillslope shape (curvature), and aquifer storage capacity. On the other hand, the effects of aspect ratio, soil type, and topographic convergence or divergence on the shape of $q(\eta)$ are small for a given hillslope geometry. The shapes for $q(\eta)$ show a combination of linear, convex, and concave components. Moreover, the magnitude of $q(\eta)$ is strongly influenced by the saturated hydraulic conductivity, and the capacity of saturated water storage or aspect ratio.

Steady-state recharge rate was examined in terms of both state variables γ and η. The relationship $r(\gamma, \eta)$ is determined by the geometric attributes of slope, hillslope shape, soil type, storage capacity, and boundary condition near the stream. The relationships γ-r and γ-η are inverse for wet soil moisture conditions. Apparently γ-η are competitive for the available storage volume. However, γ-r and γ-η have a direct relationship under dry conditions. The implications of this threshold and transition are critical to modeling and are discussed further in chapter 5.

In general, the surface saturation area increases with the increase in the saturated water storage. For the same slope shape, the effect of aspect ratio, soil type, and storage capacity on the shape of steady-state $b(\eta)$ is small, whereas the shape of $b(\eta)$ changes with the degree of slope gradient and topographic convergence or divergence. The shape of $b(\eta)$ is also affected by hillslope shape and the boundary condition at the stream. The range of b is always bounded between 0 and 1, while the range of η depends on porosity and aquifer storage capacity.

The motivation for this reasonably comprehensive series of steady-state numerical experiments is to improve the conceptual basis for interpreting storage-flux relationships observed in the field. The nature of dynamic forcing is examined in the next chapter.

3.5 Transient Experiments

The steady-state storage-flux relationships examined in section 3.4 provide insight into the equilibrium patterns of hydrologic variables as a function of geometry and hydraulic parameters. One expects however, that the general storage-flux relationships will be time dependent. Numerical experiments in this chapter investigate the dynamics of subsurface storage-flux subject to variations in the input parameters. Special attention is

given to determining the dynamic relationships for storage γ–η, runoff $q(\eta,t)$ and recharge $r(\gamma,\eta,t)$. The dynamic experiments are by no means comprehensive, and additional experiments are planned.

The dynamic experiments are conducted for two geometries, horizontal flow and convex-concave hillslopes. The state variables are presented in two ways. The first is simply the time series of the response and the second is phase plane or phase portrait of the response. The phase portrait represents a graph of the trajectories of the state variables γ-η with time implicit. Chapter 5 provides a brief discussion of the phase portrait as basic tool of dynamical systems analysis. The constitutive relations $q(\eta)$ and $r(\gamma,\eta)$ are also plotted against the state variable with time implicit. The structure of γ-η and q-η trajectories is first examined using a simple step input from initially steady-state conditions. The effects of finite-duration rainfall intensity, hillslope shape, soil type, and boundary conditions are investigated to understand their role on storage-flux dynamics. Finally, the γ-η and q-η trajectories are studied using a periodic forcing (sinusoid), and the response characteristics of storage and fluxes are analyzed and interpretations are made. For the dynamic experiments the recharge rate or flux to or from γ and η, was estimated from the numerical solution using the following form of mass balance for the saturated zone, $r=\frac{d\eta}{dt}+q$. Given discrete values for η_t and q_t, r_t is calculated explicitly $r_{t+1} = (\eta_{t+1} - \eta_t) / dt + q_{t+1}$.

3.5.1 Step Input Response

For the step input shown, Table 3.5 describes the particular information about simulation shape and input characteristics for each of the four cases examined in this section, and Figure 3.11 illustrates the input form and initial conditions. The simulation shape and boundary conditions for the horizontal flow case are shown in Figure 3.3. For the hillslope cases, shape-A-and the boundary conditions of Figure 3.2 were chosen. The geometric and physical parameter values used in case 1 and case 2 in Table 3.5 are the same as case 14 in Table 3.3, and the parameter values for cases 3 and 4 in Table 3.5 are the same as case 1 in Table 3.3. The initial condition for each experiment was based on the steady-state solution obtained for rainfall intensity f_0.

Simulation results are presented in Figure 3.12, and the γ-η phase trajectories are found to closely follow the steady-state results, which are also shown. Note that for all cases, the γ-η phase trajectories have an inverse relation except at very low-storage conditions.

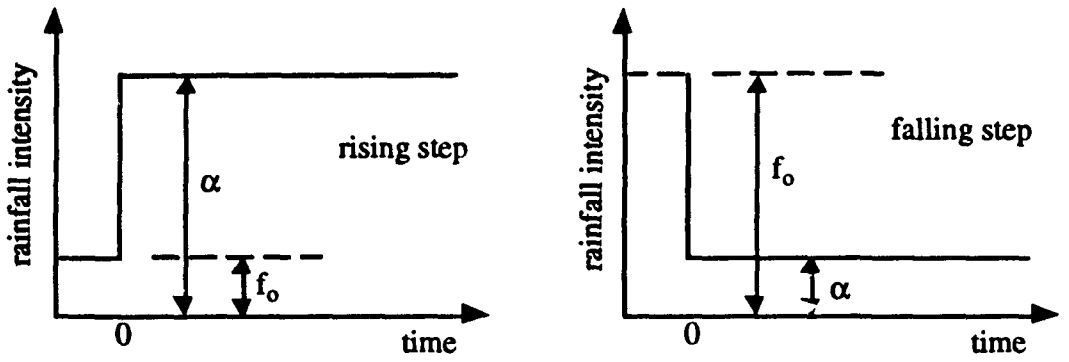

Figure 3.11 . The rising step (+) and falling step (-) for rainfall.

Table 3.5. Aquifer shape and forcing feature of step input cases.

case	type	f_o/K_S	α/K_S	aquifer shape
1	rising step	0.001	0.03	horizontal rectangular
2	falling step	0.03	0.001	"
3	rising step	0.001	0.02	hillslope
4	falling step	0.02	0.001	"

note: K_S = 0.013212 m/hr = saturated hydraulic conductivity of Guelph Loam soil.

Figure 3.13 illustrates the transient q-η relationship. The transient relationship for q-η also follows the steady-state result fairly well.

Figure 3.14 represents the time series of infiltration, recharge, and subsurface outflow for the horizontal flow system. Case 1 represents the (+) step change in input, and case 2 represents the (-) or recession. It was later determined that the rapid fluctuation in recharge were the due to the explicit equation used. The fluctuations dissipate, but do somewhat confuse the interpretation of the recharge response. In case 1 with a rising step, there is no change in the integral recharge rate until about 1440 hours, after which the recharge rate increases rapidly reaching a peak nearly 2400 hours after the start of the event.

During the recession, recharge decays slowly and converges to the equilibrium infiltration rate. It is interesting to note that recharge rate exceeds infiltration during most of rising phase. That is, the net recharge rate has been enhanced by existing soil moisture in unsaturated zone. This demonstrates the importance of soil moisture in controlling the recharge dynamics. Similar to recharge, subsurface outflow exhibits a delay at early time, and then increases to steady state.

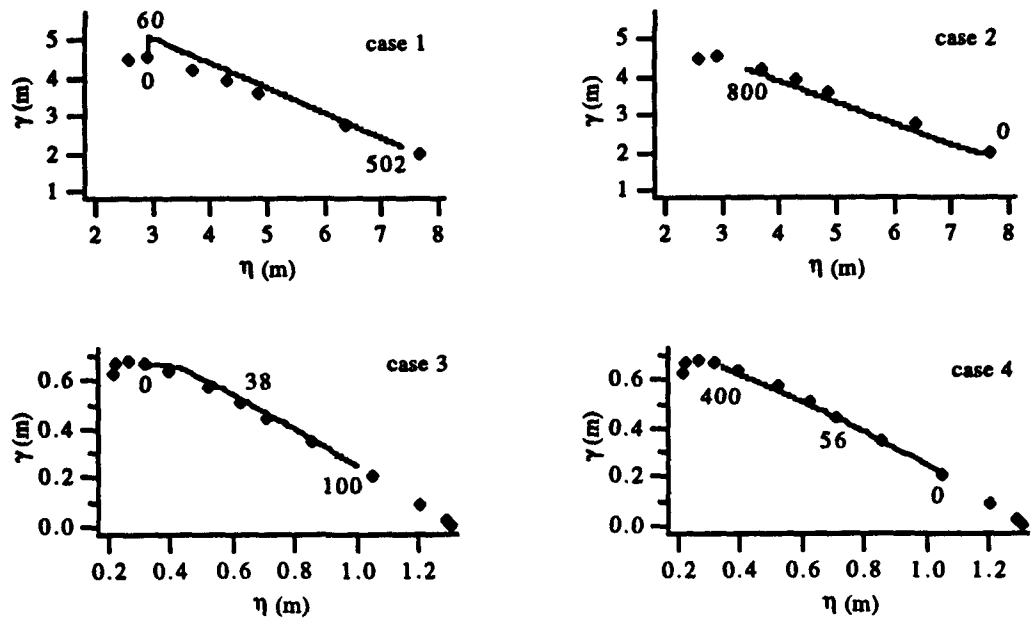

Figure 3.12. Phase portrait for γ-η. Numbers denote the position of path in days from the start of simulation. Dots refer to steady-state simulations-upper cases from case 14 and lower cases from case 1 in Table 3.3.

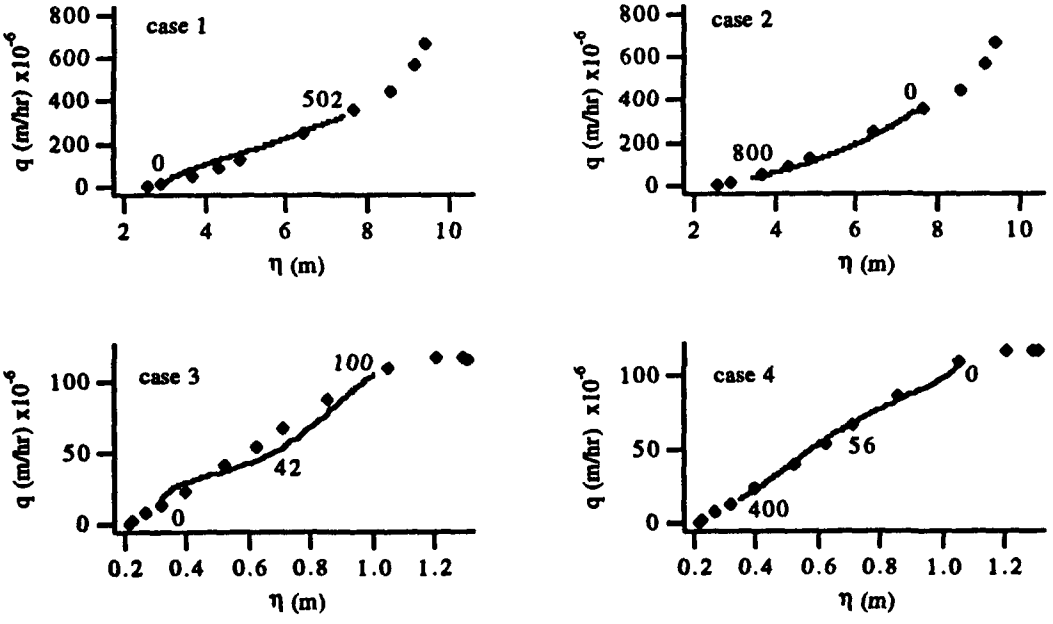

Figure 3.13. Trajectories for q-η for a step input. Numbers denote the position of the path in days from the start of simulation. Dots refer to steady-state simulations-upper cases from case 14 and lower cases from case 1 in Table 3.3.

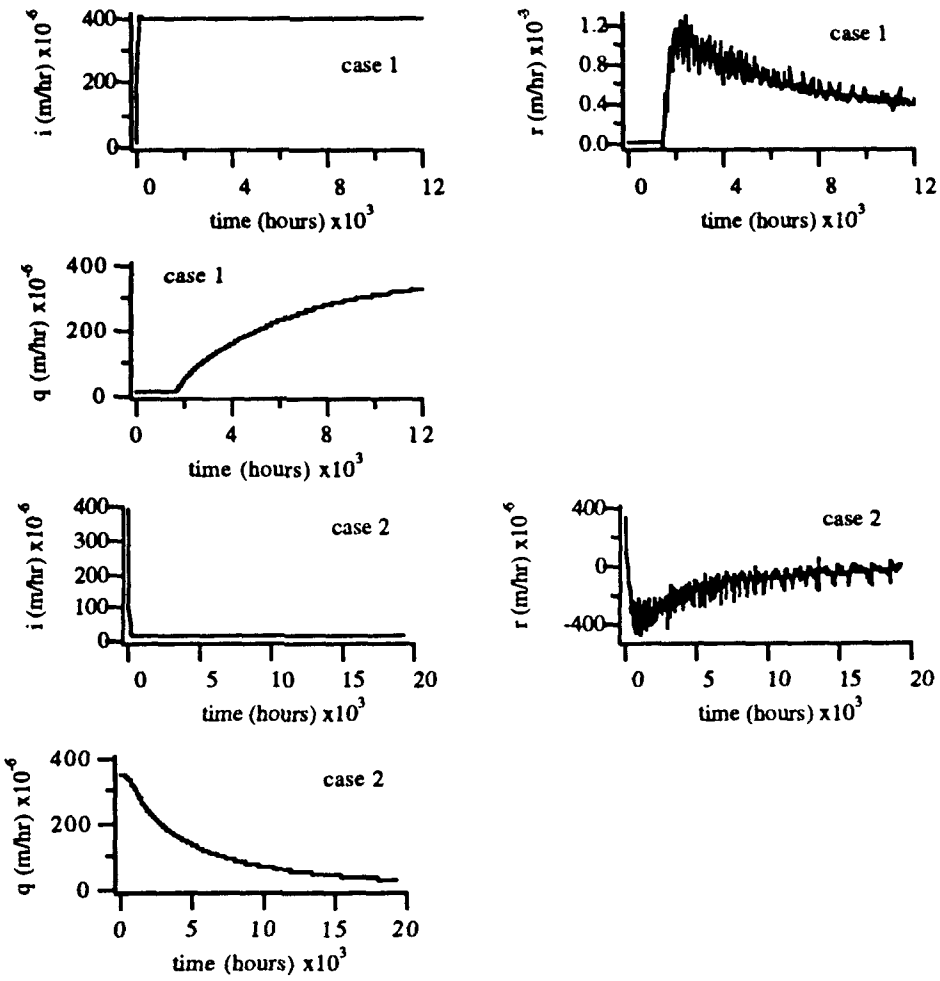

Figure 3.14. Infiltration (i), recharge (r), and subsurface outflow (q) responses to cases 1 and 2. Note: the oscillations in r are an artifact of the method used for estimation .

For case 2, with a falling step, recharge quickly decreases during the event, and the sign of recharge changes from positive to negative. Negative recharge (loss to saturated zone) is maintained during the recession to steady conditions. Negative recharge represents a loss from saturated to unsaturated storage, where the water table is relaxing while leaving behind soil moisture. The subsurface outflow response in case 2 shows a smooth relaxation, while the recharge response exhibits a slow response with numerical oscillations as in case 1.

Figure 3.15 shows the time series for infiltration, recharge, and subsurface outflow, and the surface saturation area for the hillslope response resulting from a rising and falling step input. In case 3 (rising step) the infiltration rate increases with time until it reaches infiltration capacity, and then decreases smoothly with time. The reduction in

infiltration rate is caused by the expansion of the surface saturation area where rainfall is rejected. The recharge rate displays a bimodal distribution in time, with a maximum value at around 1000 hours for this soil. The q and b response both increase with time.

In case 4 (hillslope-falling step), recharge changes sign from positive to negative similar to the horizontal flow case, and remains negative during recession. The q and b response is a simple decay. The investigation next examines the dynamics of storage and flux subject to time variations in rainfall pattern, and the role of slope shape, soil type, and boundary conditions.

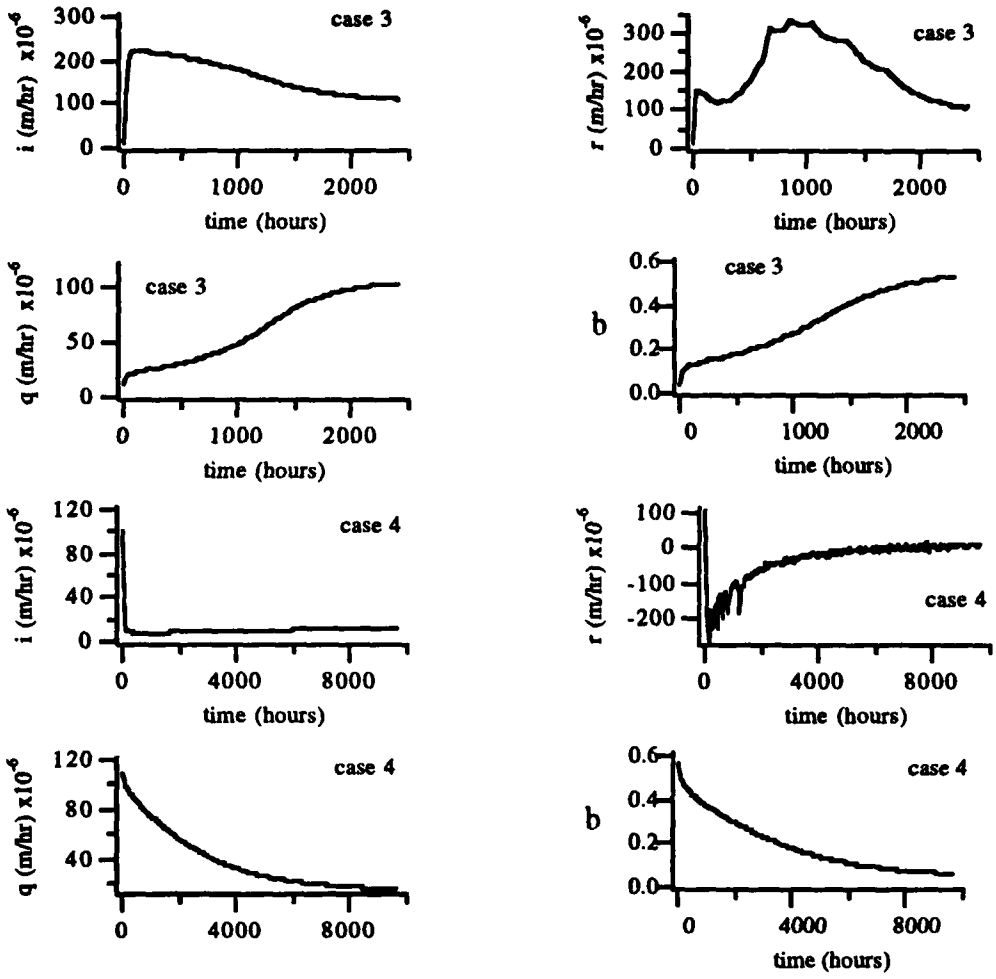

Figure 3.15. Infiltration (i), recharge (r), subsurface outflow (q), and partial area response (b) to cases 3 and 4.

3.5.2 Finite Duration Step Input

For a discrete rainfall duration as shown in Figure 3.16, three different cases were investigated by changing the intensity or duration of rainfall. Table 3.6 describes input data for the intensity (α) and duration (δ) for each case. The hillslope shape-A and boundary condition of Figure 3.2 were applied to all cases, the soil was a Guelph Loam, H/L=0.25, d/L=0.025, and L=100 m were assigned. The same parameters as case 1 in Table 3.3 were applied to all pulse input cases. To obtain a starting initial condition, a steady-state simulation was made with rainfall intensity f_o. After the storm of duration δ and uniform rainfall intensity of α, the experiment was continued until the solution returned to the original equilibrium (~250 days).

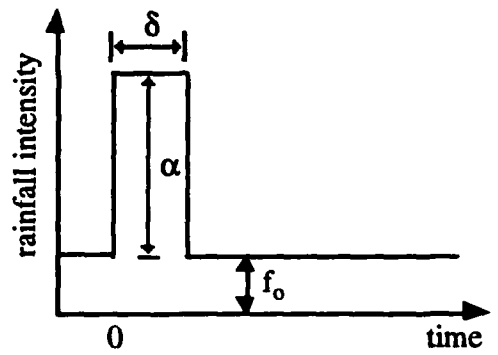

Figure 3.16. Finite duration rainfall event.

Table 3.6. Pulse input cases.

case	f_o/K_S	α/K_S	δ (hours)
5	0.002	0.2	48
6	"	0.4	"
7	"	0.2	24

note: K_S = 0.013212 m/hr = saturated hydraulic conductivity of Guelph Loam soil.

Figure 3.17 shows the transient response of q-η for all 3 cases. Clearly, the intensity and duration of the rainfall event effect the response. The departure of the transient relationship from steady-state is also indicated. This departure is large when either the intensity or the duration increases. The q-η trajectory exhibits hysteresis.

Figure 3.18 illustrates the phase trajectories for γ-η, which exhibit clockwise looping. The looping size of γ-η trajectories varies with rainfall intensity or duration. The

looping pattern itself is similar in shape for all cases. Figure 3.19 shows time series for i, r, q, and b for the pulse input simulations. The infiltration time series for all 3 cases is similar, increasing smoothly until infiltration capacity is reached at 7 to 8 hours, and then decreasing with the expansion of surface saturation area.

Apparently subsurface runoff q is characterized by two peaks. The initial peak for all 3 cases occurs at the end of the input event. The first peak magnitude varies with rainfall volume. For case 6, with the largest event volume, the magnitude of the delayed peak is greater than the first peak. For case 7 with shorter duration/volume, the delayed peak is much smaller. Clearly the magnitude and timing of the delayed peak (more than 1 month delay after the storm) depends on the rainfall characteristics, but it is also a function of the low saturated hydraulic conductivity of Guelph Loam soil used in the simulations. Additional simulations for the remaining soil types were conducted. Remarkably the timing of the second peak remained >1000 hours, but the magnitude of the second peak decreased for more permeable soils. This large delay in the second peak for these simulations illustrates an important nonlinear response of Richards equation.

Changes in the recharge response of Figure 3.19 are most dramatic during the rise and fall of the pulse input. Again, small oscillations are due to the estimation method. The recharge rate in case 6 exhibits a distinct pattern compared to other cases in that the peak recharge occurs slightly after the storm event. Note that the peak recharge rate exceeds infiltration capacity, as was noted for the step input cases.

The dynamics of the surface saturation area b(t) exhibit nearly the same response as subsurface outflow. The timing of the initial and delayed peak is identical for q(t) and b(t). Again, the expansion or contraction of b(t) largely depends on rainfall intensity and duration if other conditions on the hillslope are fixed.

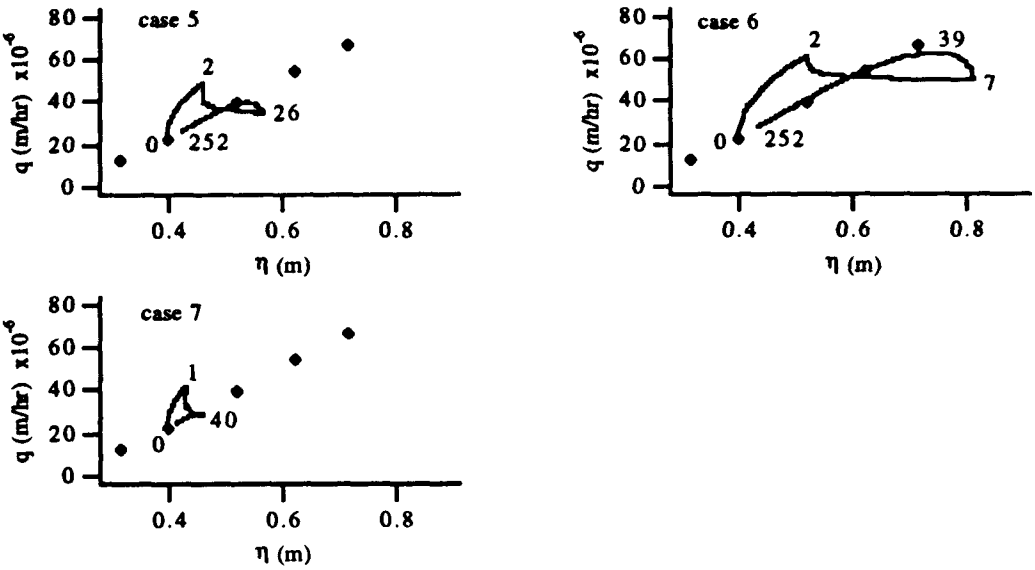

Figure 3.17. Trajectories for q and η for a pulse input. Numbers denote the position of path in days from the start of simulation. Dots refer to steady-state simulations from case 1 in Table 3.3.

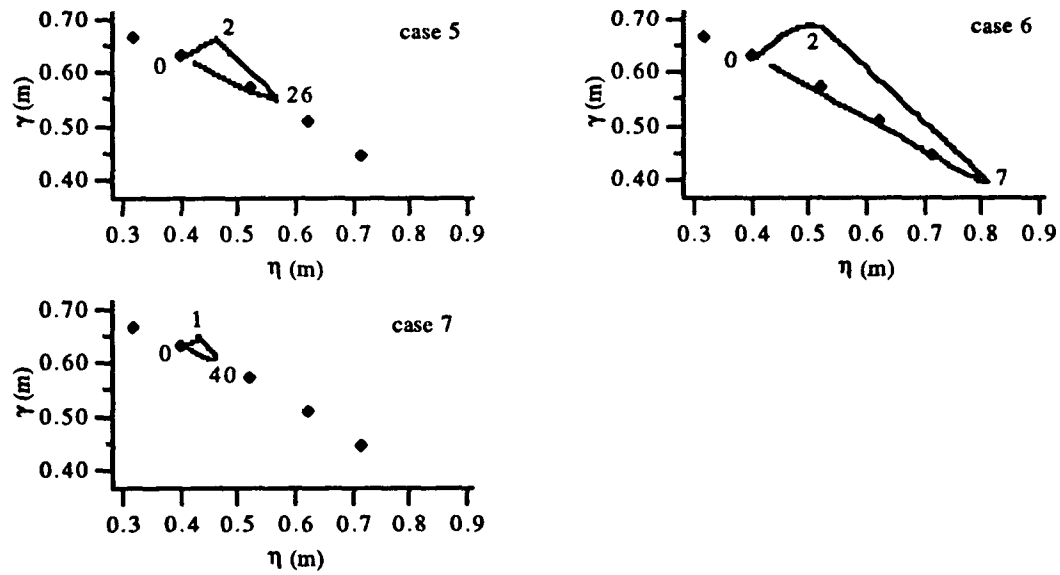

Figure 3.18. Phase trajectories for γ-η. Numbers denote the position of path in days from the start of simulation. Dots refer to steady-state simulations from case 1 in Table 3.3.

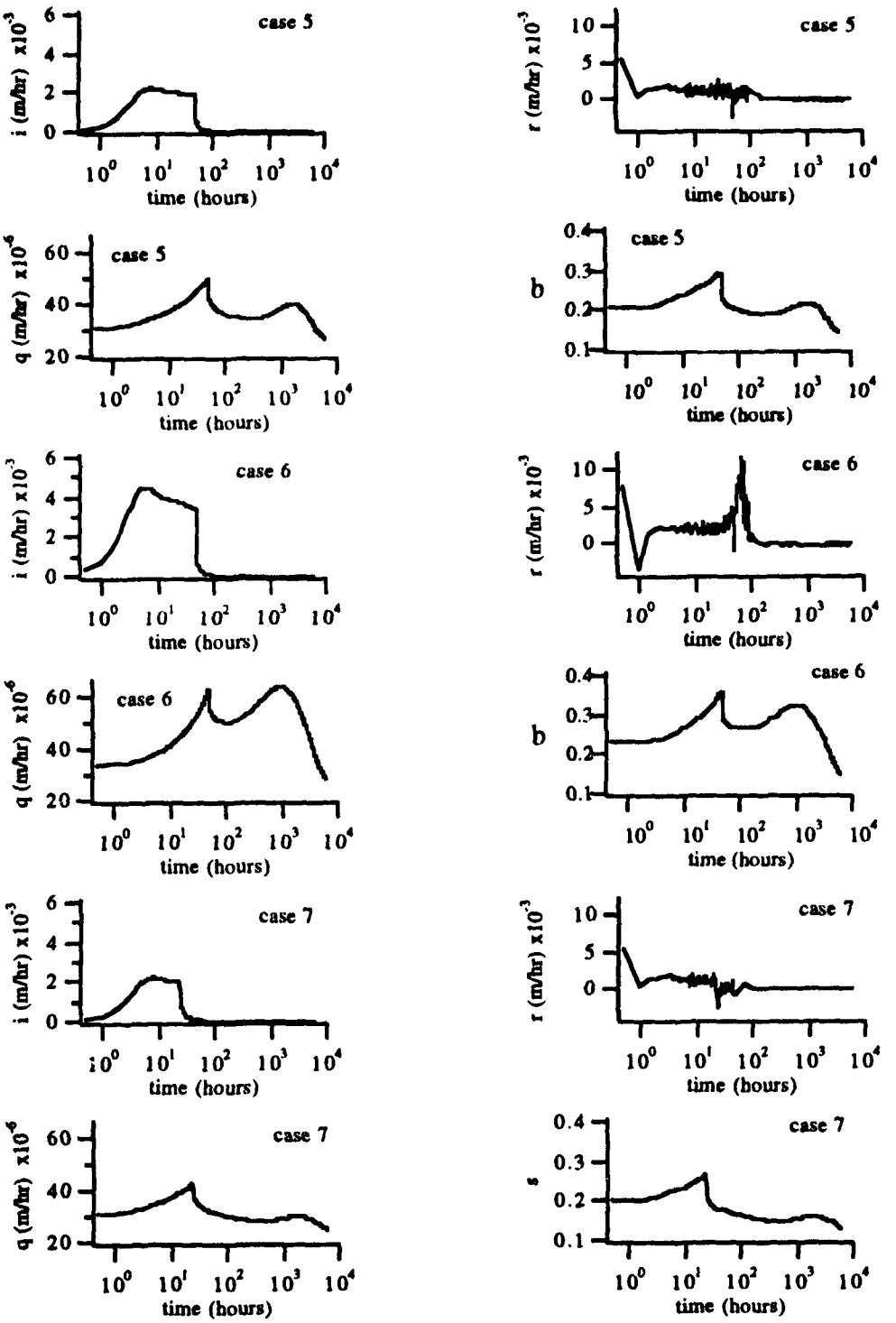

Figure 3.19. Infiltration (i), recharge (r), subsurface outflow (q), and fraction of surface saturation area (s) responses for cases 5-7.

3.5.3 Periodic Input and Dynamic Steady State

In this section the numerical experiments examine periodic variations in rainfall. Moisture conditions fluctuate from relatively dry to wet. After achieving dynamic steady state, the γ-η and q-η trajectories and the spectrum of the response time series are constructed. The shape-A hillslope and boundary condition from Figure 3.2 were assumed for the simulations. The parameters given in case 1 of Table 3.3 were implemented in the simulations. Figure 3.20 illustrates the rainfall forcing, where $p(t)=f_o+\alpha \sin(2\pi\, t/T)$. A diurnal fluctuation with input period T = 24 hours was assumed.

Three forcing amplitudes were examined as described in Table 3.7. The amplitudes $\alpha = 0.002\ K_S$ and $\alpha = 0.02\ K_S$ were used for cases 15 and 16, respectively. Case 17 represents $\alpha = 0$. A steady-state solution to Richards equation based on the rainfall intensity of $0.001\ K_S$ was the assigned initial condition. Note that all three cases examined have the same initial condition and the same average forcing amplitude.

Figure 3.21 shows the simulation response for γ, η, and q. The dotted line in the figure is the equilibrium solution based on $f_o = 0.004\ K_S$ and $\alpha = 0$.

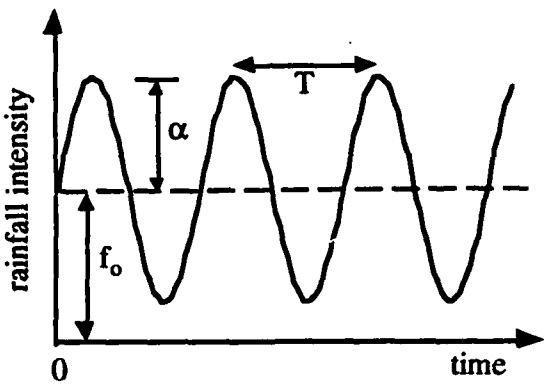

Figure 3.20. A periodic input.

Table 5.4. The periodic input cases.

case	input type	f_o/K_S	α/K_S
15	periodic	0.004	0.002
16	"	"	0.02
17	"	0.004	0.0

note: $K_S = 0.013212$ m/hr = saturated hydraulic conductivity of Guelph Loam soil.

It was observed that the time average for γ and η for the stationary response of cases 15 and 16, show an increasing departure from the equilibrium case. That is, as the amplitude of fluctuation increases, the mean q response for the fluctuating process becomes increasingly different from the static equilibrium case. Also note that γ, η vary inversely as observed earlier. The dynamic equilibrium for the two-state variables γ and η, depend on the amplitude of the input rather than the mean of the input, demonstrates a fundamental nonlinearity of the simulated soil water process.

Next, we look at the output behavior at dynamic steady state, or after transient effects have died out. Figures 3.22 and 3.23 show the time series and their corresponding power spectra for case 15 and case 16, respectively. The time series are truncated up to the last 240 hours of the signal. The power spectra were calculated based on a record length of 4096 hours with a 2 hour sampling interval or 2048 sampling points. The estimation of power spectrum was performed using MATHEMATICA software. The unit of frequency is expressed in terms of cycles/τ, where τ is the record length of 4096 hours.

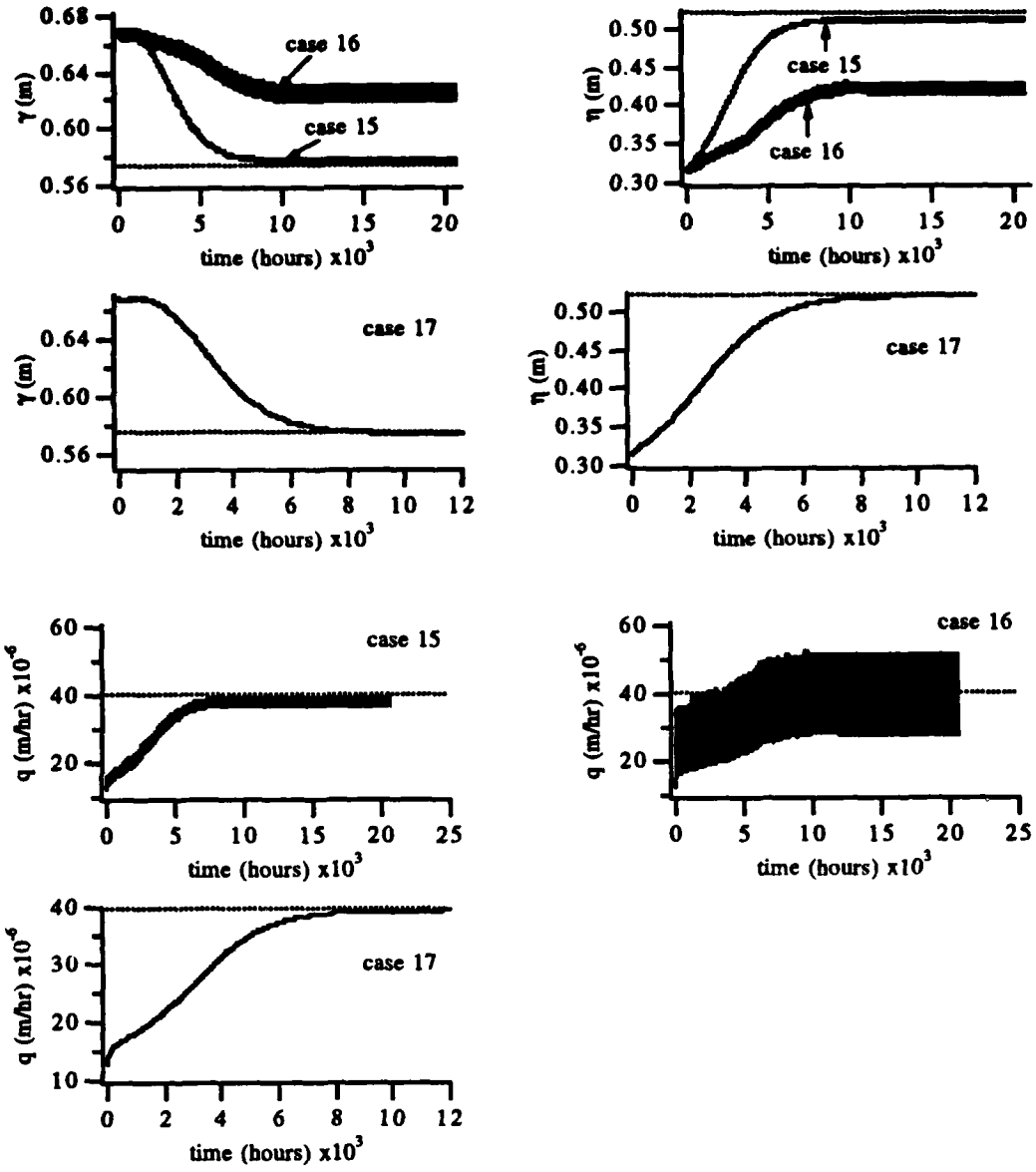

Figure 3.21. Responses for γ, η, and q for cases 15-17.

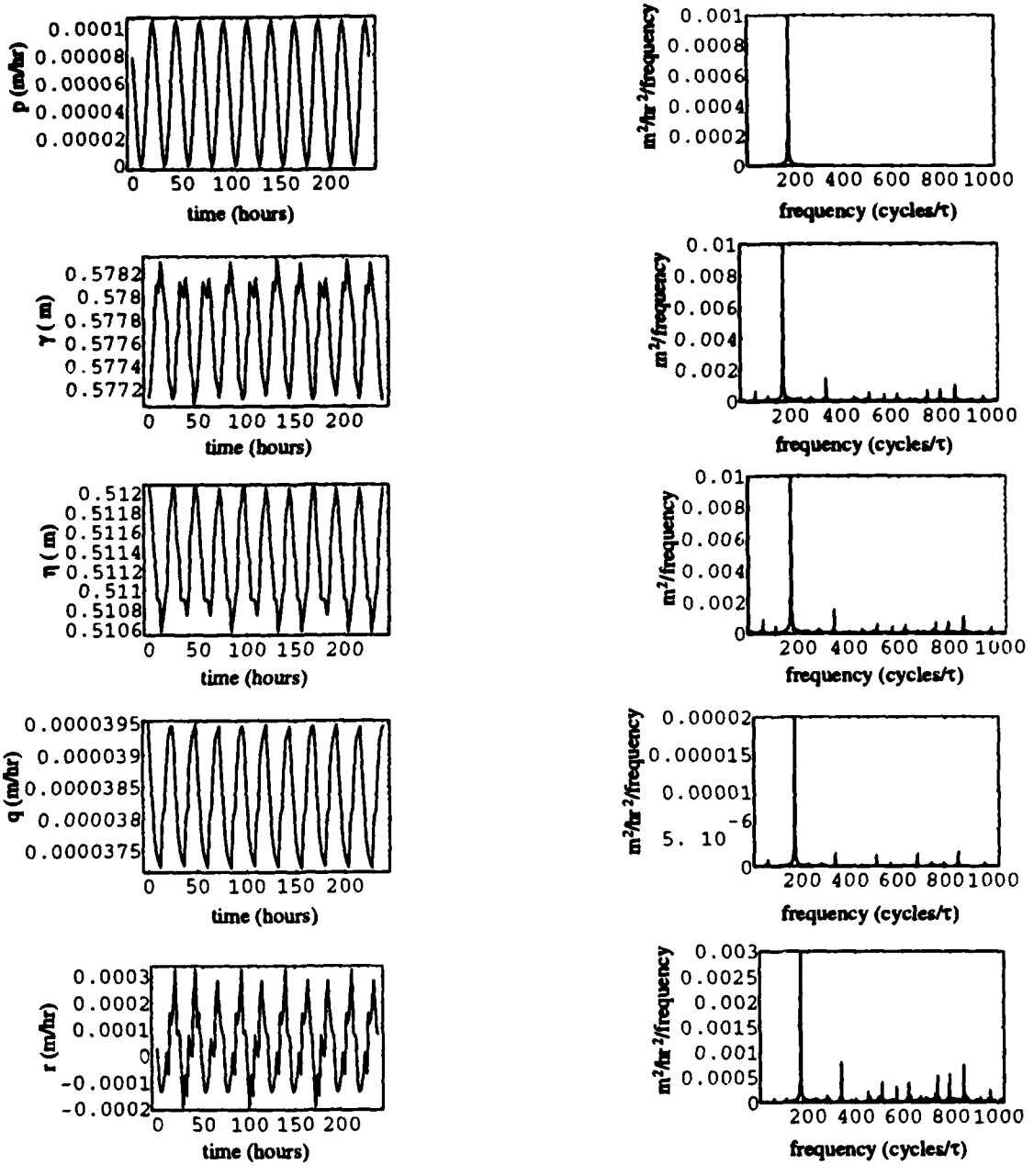

Figure 3.22. Time and frequency domain response for p, γ, η, r and q for case 15 (small amplitude case $\alpha = 0.002K_S$). The forcing frequency is 170.7 cycles/τ, $\tau = 4096$ hours.

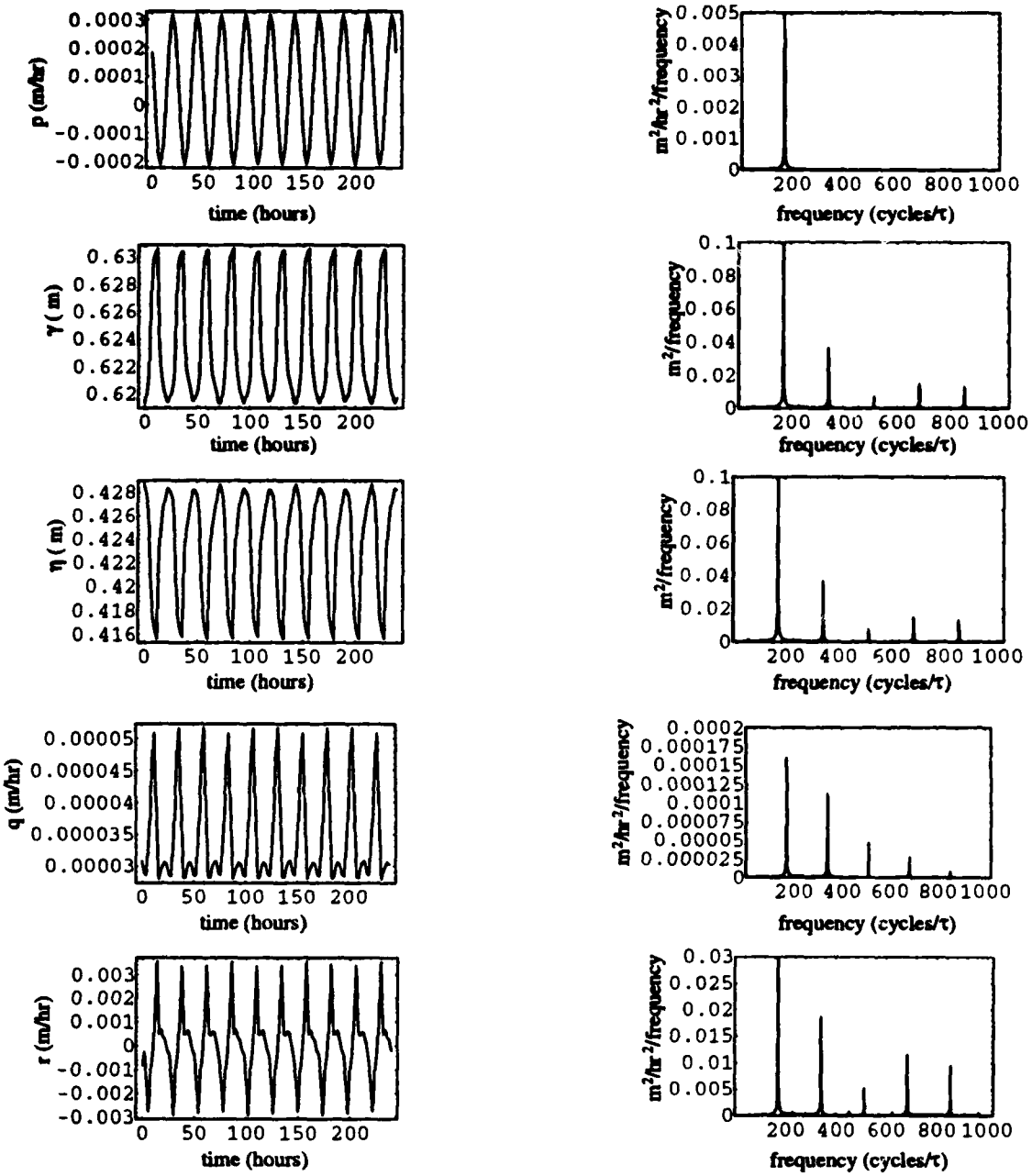

Figure 3.23. Time and frequency domain responses for p, γ, η, r, and q for case 16 (large amplitude case $\alpha = 0.02K_S$). The forcing frequency is 170.7 cycles/τ, $\tau = 4096$ hours.

Spectral analysis of the time series is used to determine the frequency content of the time series. Recall that in a linear system, a single input frequency will only produce the same output frequency. On the other hand a single input frequency with a nonlinear filter, produces a spectrum of frequencies in the output. The fundamental or forcing frequency is the largest spectral peak, with integer multiples of the forcing frequency indicating the nonlinear effect. This form of nonlinearity known as harmonic distortion.

Other types of nonlinear behavior can be detected via signal processing tools. Higher order spectra such as the bispectrum offers the possibility of detecting the role of nonlinear behavior reflected in the frequency content of higher time moments (e.g. skewness). Our initial attempts at higher order spectral analysis for stream-aquifer problems in this research effort, are described separately in Jin and Duffy (1994).

For the case of small forcing amplitude, the dominant power or variance in γ, η, r and q spectra is concentrated at the forcing frequency (Figure 3.22). However some variance is observed at harmonics of the forcing frequency. The peak amplitude in the recharge power spectrum is 3 times as large as the peak magnitude in rainfall spectrum. On the other hand, the peak power in the subsurface outflow spectrum is highly damped compared to the peak amplitude in rainfall or recharge power spectra. The spectral peak for γ and η spectra are nearly the same magnitude.

As the forcing amplitude increases (case 16), the spectral peaks in the γ, η, r, and q series also increase (Figure 3.23). The power spectra show that total variance in the records is mainly in the first and second harmonics, except for the recharge signal where higher harmonics exist, probably related to the estimation problem described earlier. Clearly, as the forcing amplitude increases, the amplitude of secondary spectral peaks also increases. As in case 15, the spectral peaks for γ and η are similar.

Figure 3.24 shows the γ-η phase trajectories constructed from the stationary time series. It is found that the phase trajectories cycle in a clockwise direction but the looping is not very broad. Much more analysis is required to fully understand the implications of this behavior.

Figure 3.25 displays the q-η phase trajectories. The q-η phase trajectories change with the forcing amplitude, and the looping structure apparently is affected by the secondly harmonics. Again, this behavior requires additional analysis to fully understand the structure.

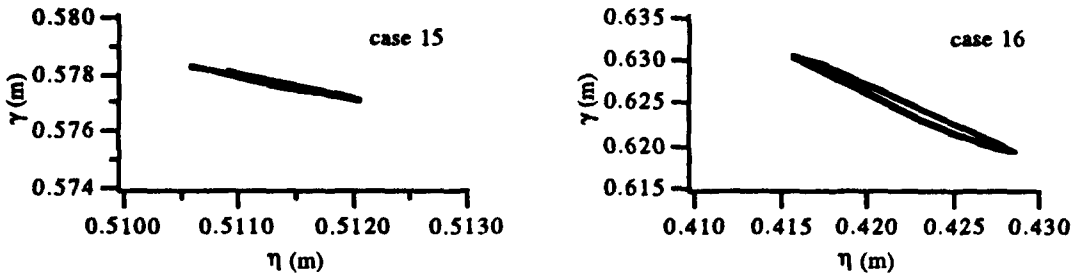

Figure 3.23. Phase trajectories for γ-η for cases 15 and 16.

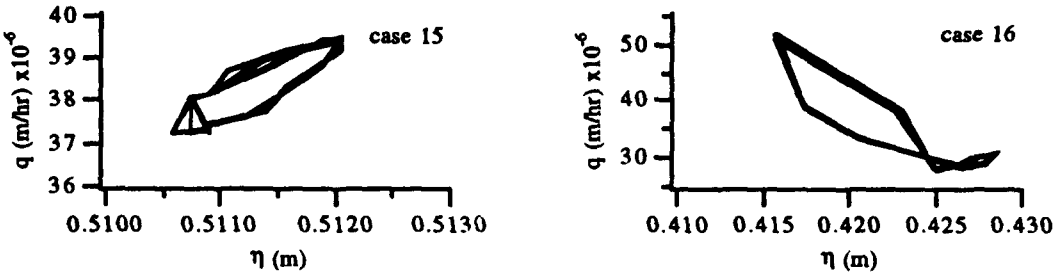

Figure 3.24. Trajectories of q-η for cases 15 and 16. The direction for phase trajectories is clockwise for both cases.

3.5.4 Discussions of Results

The delayed subsurface outflow peak has been observed through simulation with Richards equation under a specified hydrologic conditions. The mathematical origin for delayed subsurface outflow peak appears to be nonlinearity inherent in soil water process. During the storm event, the saturated region expands upslope due rapid infiltration and recharge. Following the storm event, accumulated upslope infiltration moves downslope primarily as a saturated layer above the bedrock. Since this lateral subsurface flow takes some time to reach the discharging area of hillslope, a delayed subsurface flow is observed. This mechanism for the delayed peak has little to do with the expansion of the saturation region near the stream, but rather depends on expansion of the upslope subsurface saturation region. Figure 3.25 illustrates the numerical simulation of this effect. Each component of the response is labeled. The magnitude and timing of the delayed subsurface outflow peak depends on factors such as the nature of input forcing, topography, soil type, and storage capacity of hillslope.

The dynamic relationships for q(η) based on Richards equation exhibit hysteresis, even though the soil property assumed is homogeneous and non-hysteretic. In the field,

Duffy et al. (1991) also observed a hysteretic relationship between baseflow and saturated water storage at the Upper Sheep Creek hillslope watershed. They also provide a qualitative discussion of hysteresis which involves the interplay between slope steepness, near-channel storage, the distribution of infiltration sources, and soil heterogeneity. Without any complicating factors present in the field, hysteretic behaviour evident in the physics-based model under the idealized conditions appears to be related to the dynamic interaction between saturated water volume and subsurface outflow.

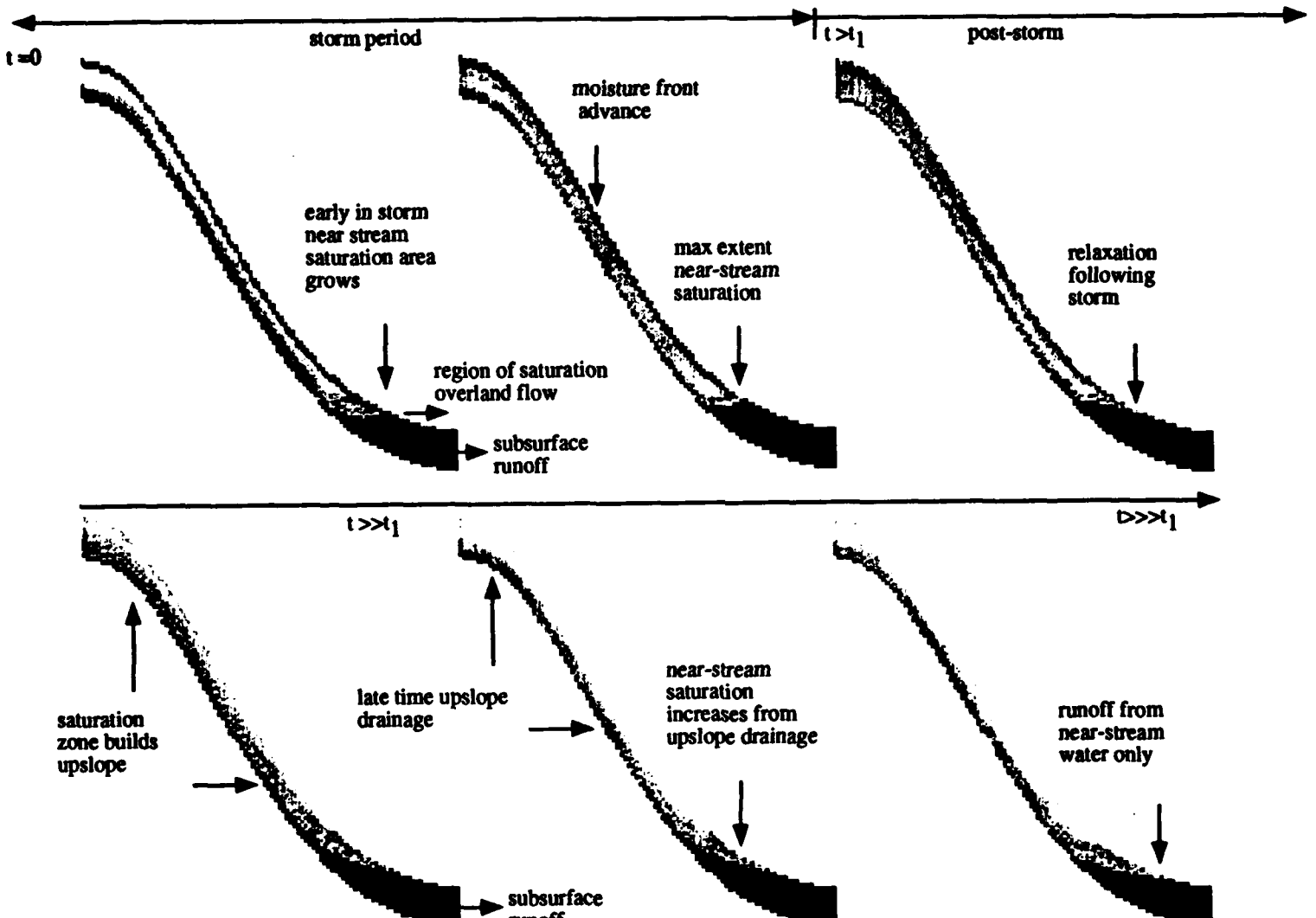

Figure 3.25. The evolution of a pulse type storm event.

4. FIELD EXPERIMENT AT SHALE HILLS

4.1 Description of the Experimental Watershed 2

The Shale Hills Watershed 2, a 7.9 hectare forested site located near the Penn State campus was the subject of an NSF-funded experimental study, initiated in the 1970's, to evaluate the effects of antecedent soil moisture on stormflow volumes (J. Lynch, 1976). The site is a forested watershed characterized by steep slopes and narrow ridges typical of the low-lying shale hills of the Ridge and Valley Province of eastern United States. The average slope gradients are 16 and 18 degrees on the south and north aspects, respectively. The average channel gradient is 4.5 %. The maximum relief is 61 meters and average local relief is about 30 m.

The study area is underlain by the Rose Hill shale about 213 m thick with occasional interbedded limestone. Soil depth or depth to bedrock is quite uniform, with the ridges only slightly thicker than the valley floor, and the estimated average soil depth is 1.4 meters (Lynch, 1976). Soil types on the watershed are Ashby shaley-silt-loam that mantles the moderate to steeply sloping valley sides. Blairton silt-loam is found on the gently sloping upper end of the valley, and Ernest silt loam underlies the lower valley floor. Leavesley (1967) and Lynch (1976) provide a detailed description of soil physical properties, the soil profile, vegetation characteristics, and history of land use.

At Watershed 2, Lynch (1976) instrumented the site with artificial rainfall sprinklers, and simulated rain events from July 31, 1974 to September 20, 1974. During this period, 8 sequential artificial storm events were replicated with the same intensity of 6.1 mm per hour and duration of 6.15 hours. Rainfall depth was measured by a network of rain gages: six recording, 40 standard eight-inch and 17 trough-type nonrecording gages. Stream discharge was measured at 4 different weirs with continuous recording water level recorders. Soil moisture content at 32 locations was monitored using neutron scattering method. At each site soil moisture measurements were made at one foot intervals from the surface to bedrock. Water table elevation was obtained for fifty shallow observation wells. We have used a portion of this data base to investigate a method for estimating the integrated storage-flux relationship, as part of a longer term goal of implementing the integral balance modeling approach at the site. Table 4.1 below gives a summary of the results for all eight storms. Note the small range in total antecedent moisture, and the order of magnitude increase in total storm runoff.

Date	antecedent soil moisture mm	total storm runoff mm	rapid flow mm	delayed flow mm	max. peak flow m^3s^{-1}/km^2
*8/01/74	278.1	4.55	2.64	1.90	0.099
*8/07/74	287.5	12.19	8.36	3.84	0.201
8/14/74	290.1	15.52	11.94	3.58	0.253
*8/19/74	295.1	15.90	12.27	3.63	0.239
8/23/74	304.8	20.75	17.02	3.73	0.304
8/27/74	310.4	23.34	19.58	3.76	0.328
*9/16/74	313.2	29.74	25.78	3.96	0.526
9/19/74	316.2	32.66	28.88	3.78	0.628

Table 4.1. Stormflow volumes for eight 6.1 mm/hr artificial storms of 6.15 hour duration. The experiment was conducted over a range of antecedent moisture conditions (after Lynch, et al, 1976). Note: * indicates the events used in the present research.

Figure 4.1. illustrates a subset of the field data which Lee (1993) has analyzed and these results are presented here. Stream stage was measured continuously during and after each storm. The soil moisture and groundwater levels were measured just before the event, immediately at the end of the event, and daily after the event, until the runoff response was complete or a new rainfall event was initiated. Characteristic curves for the soils are available. Figure 4.1 also shows contour lines and flow paths orthogonal to the contours at Watershed 2. Six soil moisture access sites and eight observation well sites were chosen for this study between weir 2 and weir 4. Four events were selected and these are indicated in Table 4.1. Soil moisture and water table elevation measurements were available before an event and once a day after the event.

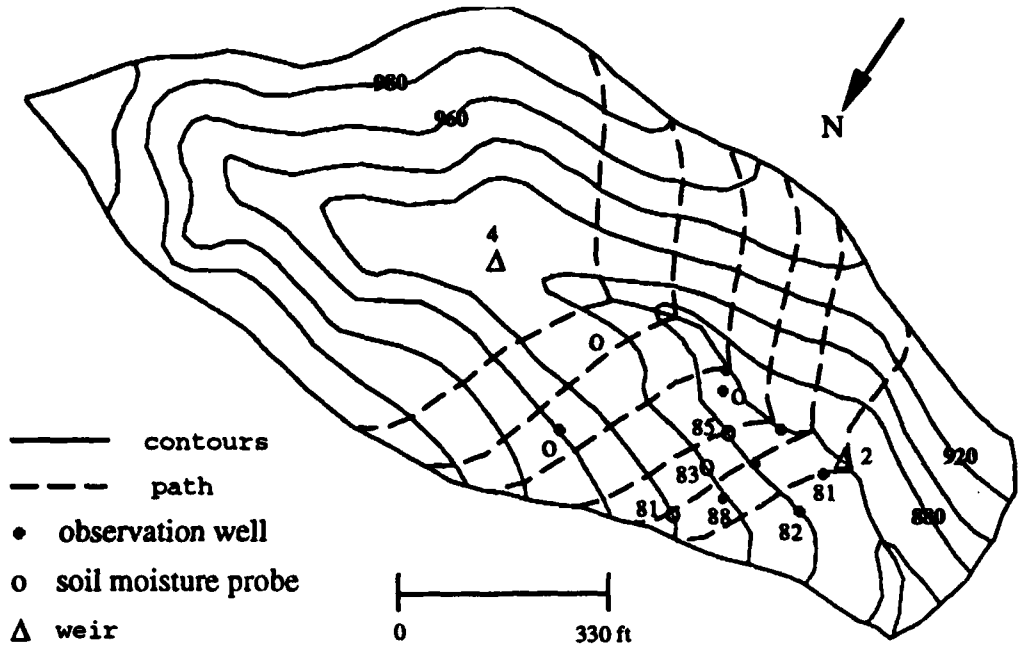

Figure 4.1. Contour and path lines, and monitoring sites at Watershed 2.

4.2 Defining Similarity Regions

Duffy et al. (1991) have proposed a local affine transformation of the hillslope as a basis scaling state variables and for estimating the storage-flux characteristics of a hillslope. The method of rescaling the trajectories to form a unit hillslope is discussed in chapter 2. Of course the critical problem is to determine the region over which the hillslope geometry is self-affine. Figure 4.1 illustrates a hillslope where trajectories were found to be approximately similar. Recall that the motivation for determining similarity regions is to rescale the land surface, bedrock, water table and soil moisture, such that sparse and scattered field data (water levels, bedrock elevation, etc.) can be plotted on a smooth curve. Each trajectory starts at the divide and truncates at the stream (local base level), following the steepest path orthogonal to contour lines. The topography scaled in this manner is locally self-affine since two length scales are required, one for elevation and one for distance. As perfect scaling is not possible, the unit hillslope for a similarity region is constructed in a statistical sense, by fitting. Once the similarity region is determined the hypsometric relation or area elevation distribution is also determined so that spatial averaging can be performed.

By trial and error the similarity region for the hillslope in Fig. 4.1 was determined, and the fitted surface and bedrock topography is shown in Fig. 4.2. The difference

produces the corresponding soil-colluvium thickness for the unit hillslope. The fitted polynomials along with the rescaled water table at a particular time are shown in Figure 4.3, which together define the saturated fraction of the unit hillslope. The conditional hypsometric distribution for the hillslope is shown in Figure 4.4, with scaled elevation $0 \leq z \leq 1$.

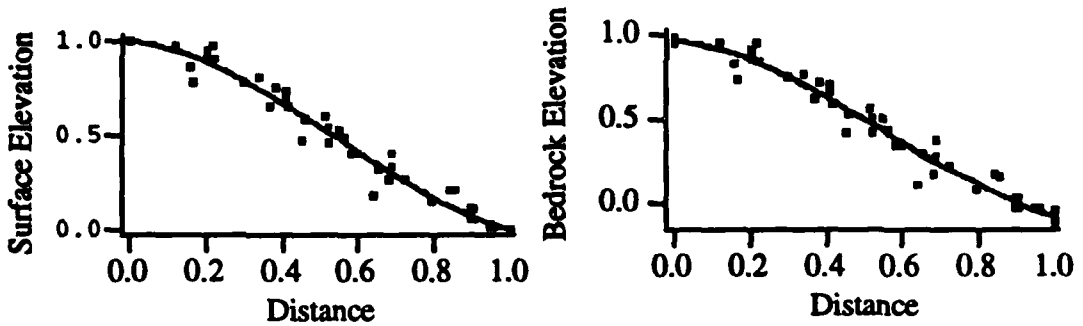

Figure 4.2. Projection of the surface and bedrock trajectories from Figure 7 onto the unit hillslope. Surface shape function: $z_0(s)=1 - 0.175\ s - 2.09\ s^2 + 1.27\ s^3$. Bedrock shape function: $z_2(s)= 0.972 - 0.136\ s - 2.411\ s^2 + 1.526\ s^3$.

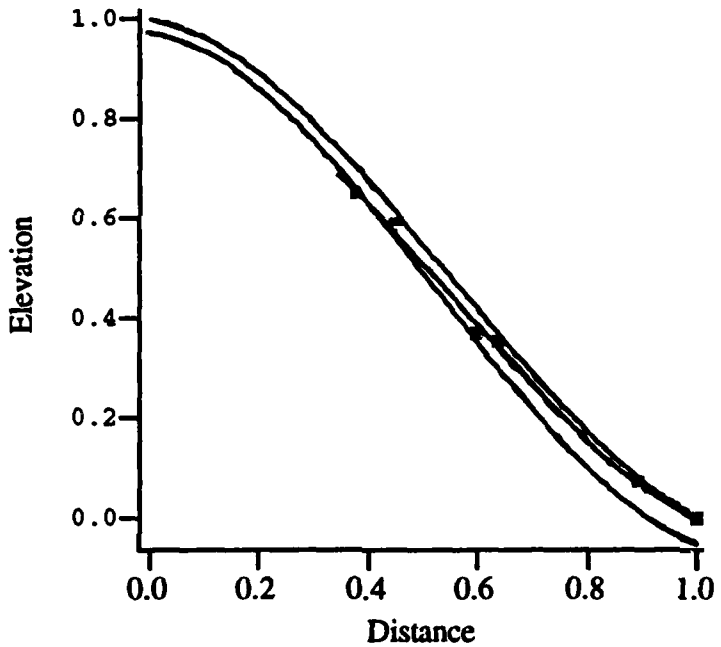

Figure 4.3. Water table shape function: $z_1(s)= 0.829 + 0.374\ s - 2.807\ s^2 + 1.607\ s^3$ and the rescaled unit hillslope $z_0(s)$ with corresponding trajectory of bedrock $z_2(s)$. Date: 19 Aug. 1974.

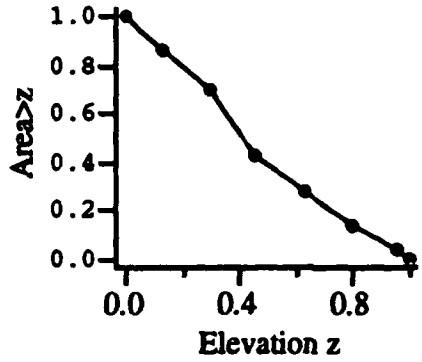

Figure 4.3. The area-elevation relation or conditional hypsometric curve for the hillslope of Figure 4.1.

In the field experiment (Lynch, 1976) neutron probes were used to estimate the vertical distribution of soil moisture at 1 foot sampling interval down to the bedrock surface (e.g.. total moisture in the soil column). Water table elevation measurements were determined independently from piezometers. Integration of the resulting polynomials proceeded as outlined in chapter 2, and the state variables for spatially integrated soil moisture and saturated storage were determined. In the next section the results are given for four simulated rainfall events with the varying antecedent soil moisture.

4.3 Integrated Storage-Flux Response

The analysis of the hillslope study for the four events are shown in Figures 4.4-4.7 Each figure shows the time response for discharge (Q [m^3/hr]) at the upstream weir 4, the downstream weir 2, estimated recharge, and the integrated unsaturated and saturated storage elements. The time series for point measured soil moisture and the depth to water table at various locations on the hillslope are given in the figure. The water table elevation and depth-averaged soil moisture are plotted versus ground surface elevation.

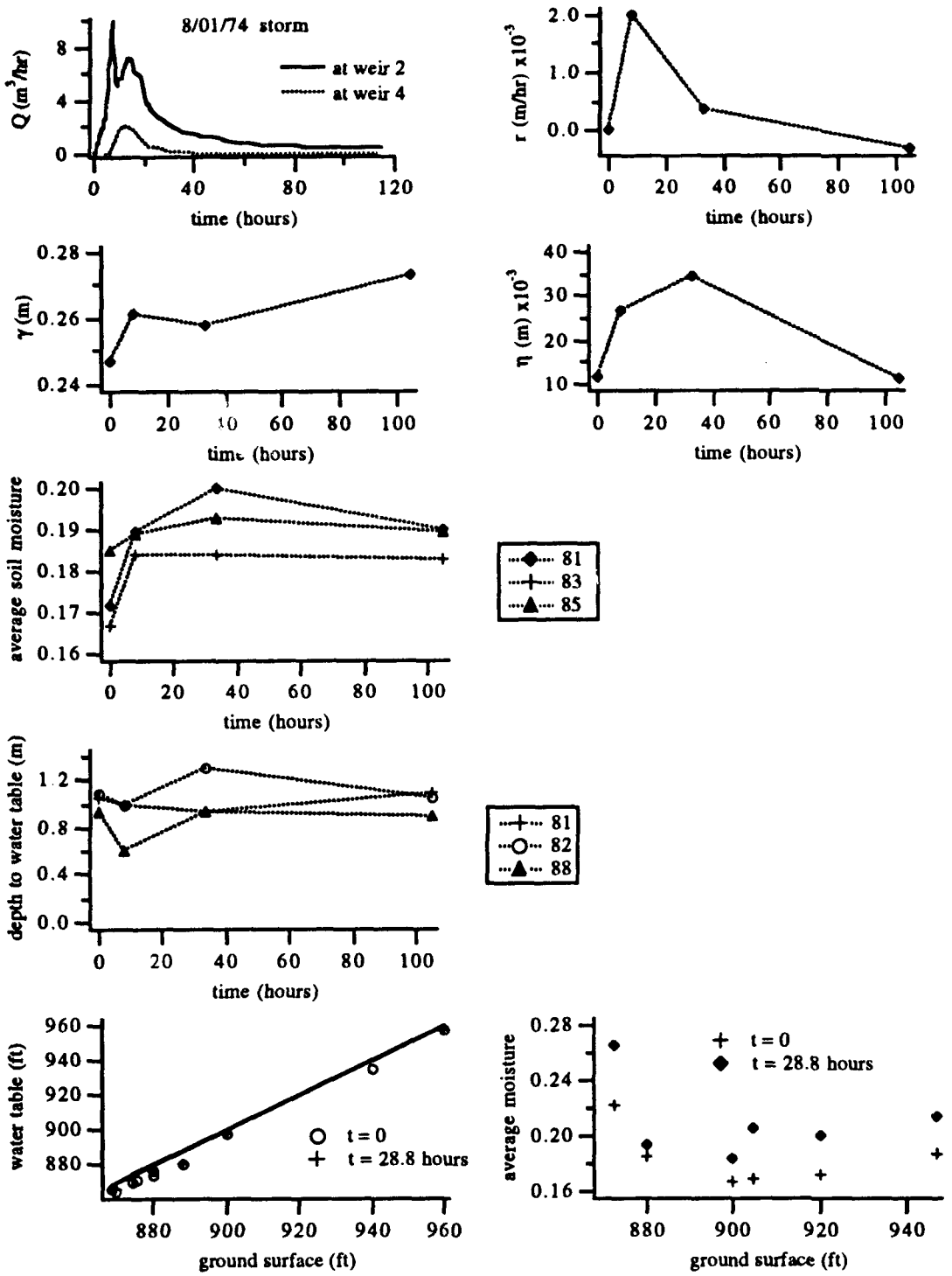

Figure 4.4. The Q, r, γ and η hydrographs, and time and space distribution for depth-averaged moisture and water table for 8/01/74 storm. The ground surface and water table refer to elevation. The position for moisture access tube and observation well locations is shown in Figure 4.1.

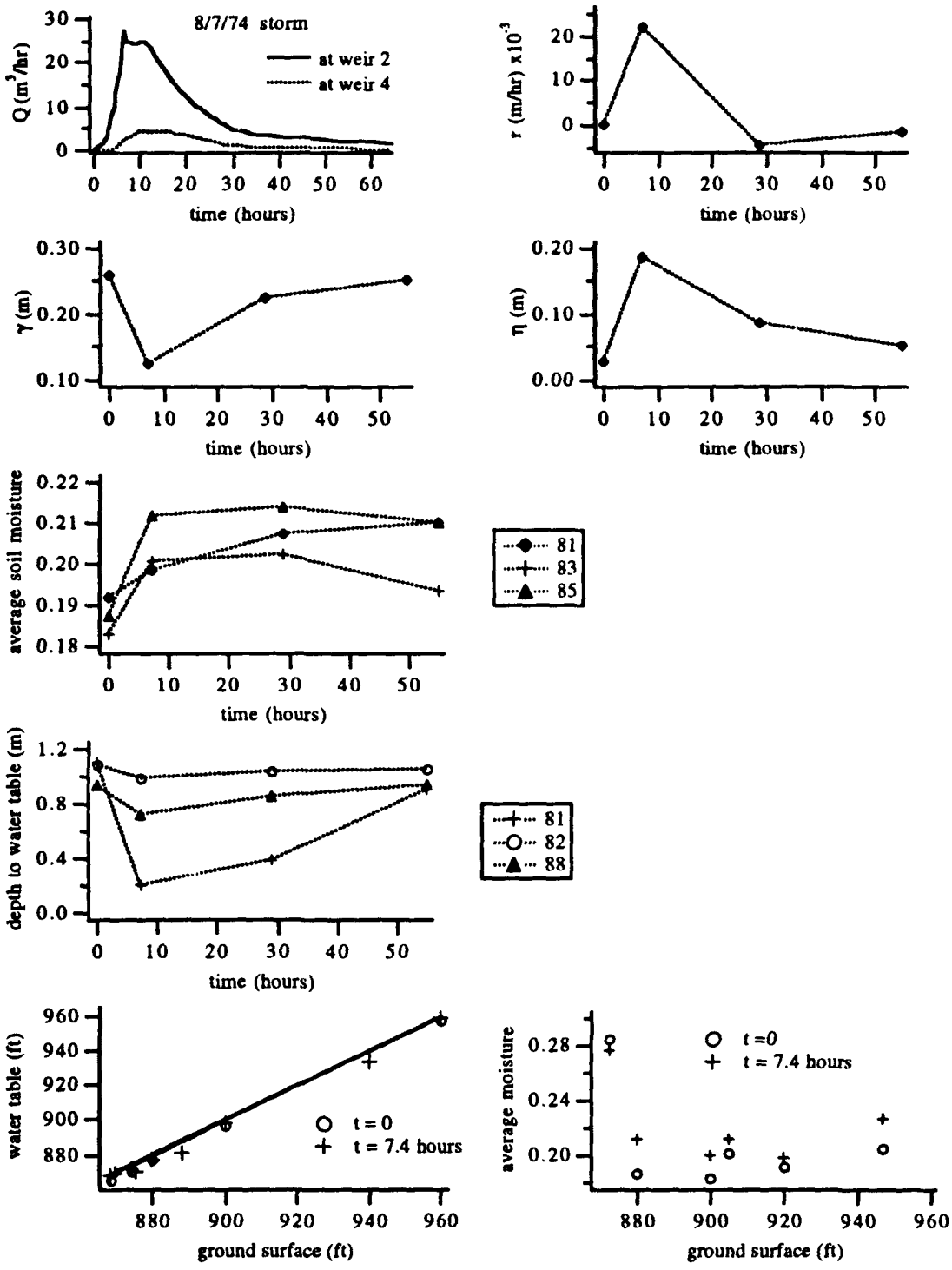

Figure 4.5. The Q, r, γ and η hydrographs, and time and space distribution for depth-averaged moisture and water table for 8/7/74 storm. The ground surface and water table refer to elevation. The position for moisture access tube and observation well locations is shown in Figure 4.1.

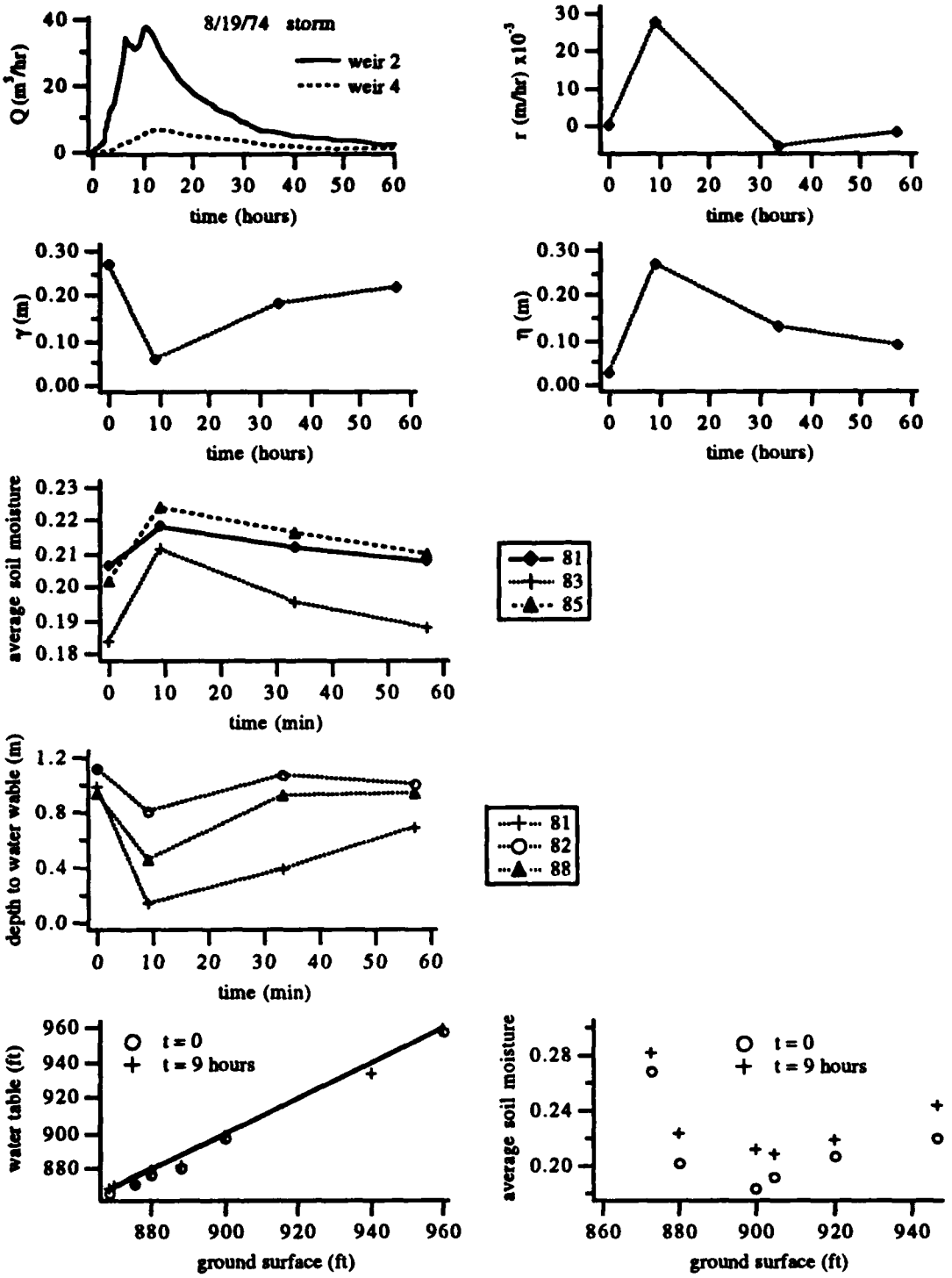

Figure 4.6. The Q, r, γ and η hydrographs, and time and space distribution for depth-averaged moisture and water table for 8/19/74 storm. The ground surface and water table refer to elevation. The position for moisture access tube and observation well locations is shown in Figure 4.1.

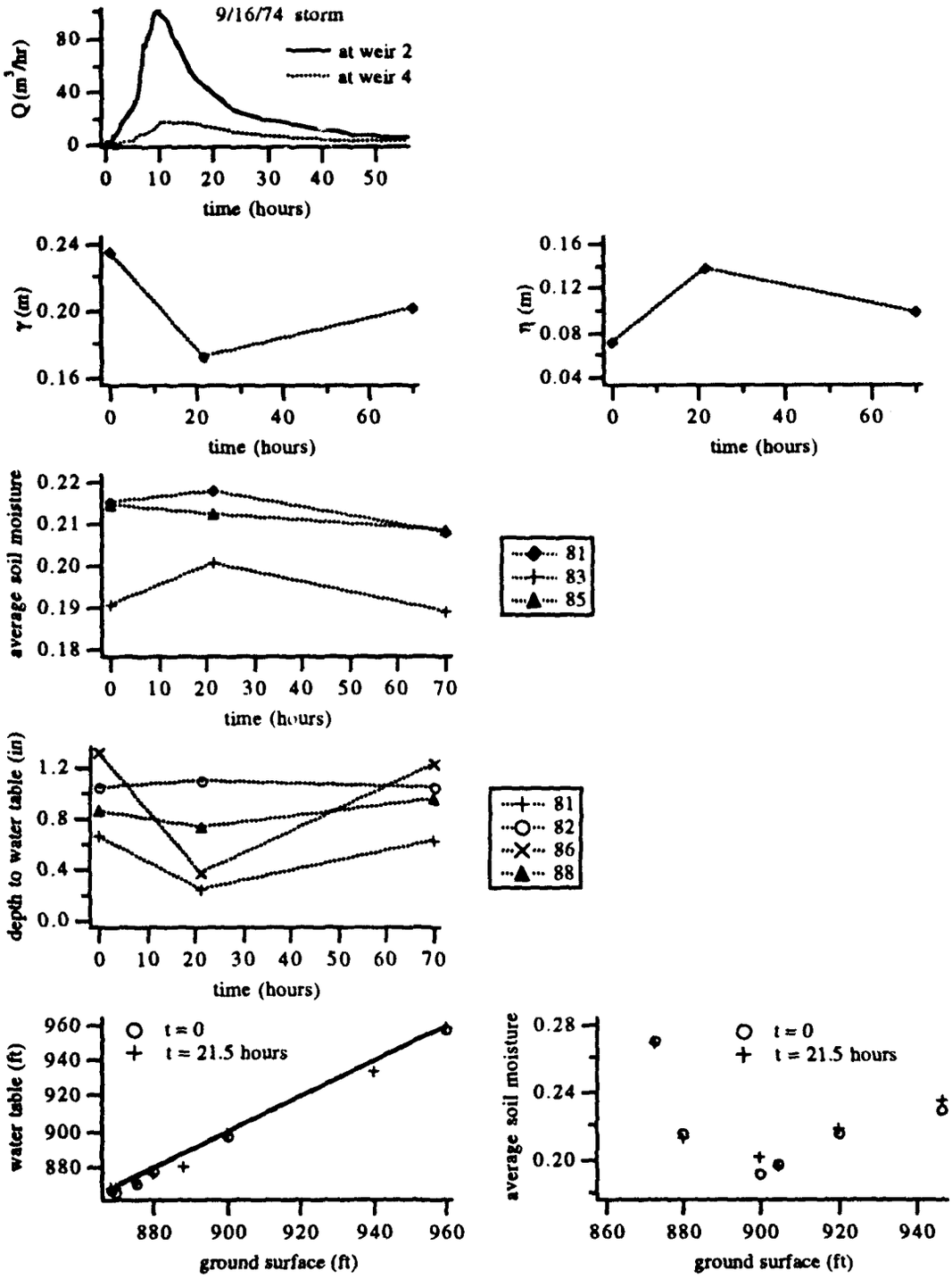

Figure 4.7. The Q, γ and η hydrographs, and time and space distribution for depth-averaged moisture and water table for 9/16/74 storm. The ground surface and water table refer to elevation. The position for moisture access tube and observation well locations is shown in Figure 4.1.

The discharge hydrographs at downstream weir 2 display both single and double peaks, while no delayed streamflow peak is observed at upstream weir 4. The double peaks are present in the 8/01/74 and 8/19/74 storms, a minor second peak occurs on 8/7/74, and the 9/16/94 storm has no double peak. For 8/01/74 storm, the delayed peak discharge is smaller than the initial peak, but the second peak is larger than the first for 8/19/74 storm. The presence of double peaks appears to vary with antecedent soil moisture conditions, and wetter initial conditions cause the second peak to diminish or disappear. We note that the discharge at weir 4 is small in magnitude and lags discharge at weir 2.

Recharge hydrographs are constructed based on an explicit finite difference form of the integral balance equation for the saturated zone as discussed in section 3.5, where discrete q and η time series are used. During the event, recharge rapidly increases, while post-event recharge decreases with a sign change from positive to negative during the drainage period. The r is positively correlated with η and negatively correlated with γ except for 8/1/74 storm (dry conditions). Saturated storage increases for each storm event, and decreases during the recession period. Unsaturated storage γ shows an inverse relation to η response. The distribution of soil moisture and water table elevation measured at 3 locations demonstrate the difference between the point measured response and the integrated response. Note that at a point on the hillslope the soil moisture response increases during and then decreases after the storm, while the integrated soil moisture decreases and then increases. It is important to emphasize that the competitive nature of γ and η dynamics observed in the numerical experiments is also observed in the field data. Another interesting observation is that the overall range of integrated soil moisture change is quite small, less than 4 % by volume for the entire experiment.

Although the data are sparse for all storms examined, the time scales for discharge and storage are different when comparing the storm event with the drainage period. If we define the time scale as the slope of the curve Q versus dQ/dt, then during the storm phase the time scale is seen to be much shorter than during recession phase. This may also be the result of the competitive relationship between capillary and gravity storage during the storm and recession periods.

The relationship between altitude and water table elevation is evaluated at two times, before and after the storm. The relationship shows that the water table is highly correlated with surface topography. This empirical correlation provides support for the unit hillslope scaling method for water balance studies. The depth-averaged soil moisture is high near the stream as expected, is lower over the mid-slope region, and interestingly is somewhat higher again in the ridge-top region. Again, a clear pattern exists within the similarity region.

Figure 4.8 shows the γ-η and q-η trajectories for all storms analyzed in this chapter. The γ-η trajectories exhibit an inverse relationship which indicates a competitive relation between the state variables. For the dry initial-moisture condition of the 8/01/74 event, γ increases with η during the storm, while γ increases and η decreases during the recession phase. The looping behavior is seen in the γ-η phase portrait, but the width of the loop is small. The looping or hysteretic behavior is much more pronounced in q-η trajectories. The q-η paths reveal clockwise evolution for all storm events and its shape and magnitude vary with antecedent soil moisture condition. .

Figure 4.9 illustrates the $\gamma(\eta)$ and $q(\eta)$ relationship for the data of all four events. A linear function was fitted to the relationship $\gamma(\eta)$, and a quadratic polynomial was fit to the relationship $q(\eta)$.

Figure 4.10 illustrates the structure of r-γ-η trajectories for each storm. The figure also indicates the projection of r-γ-η phase trajectories onto orthogonal planes of r-γ, r-η, and γ-η. Although the data are sparse, recharge is negatively correlated with unsaturated storage for the recessions of the 8/7/74 and 8/19/74 events, and the trajectory in the r-γ plane shows a counter clockwise motion.

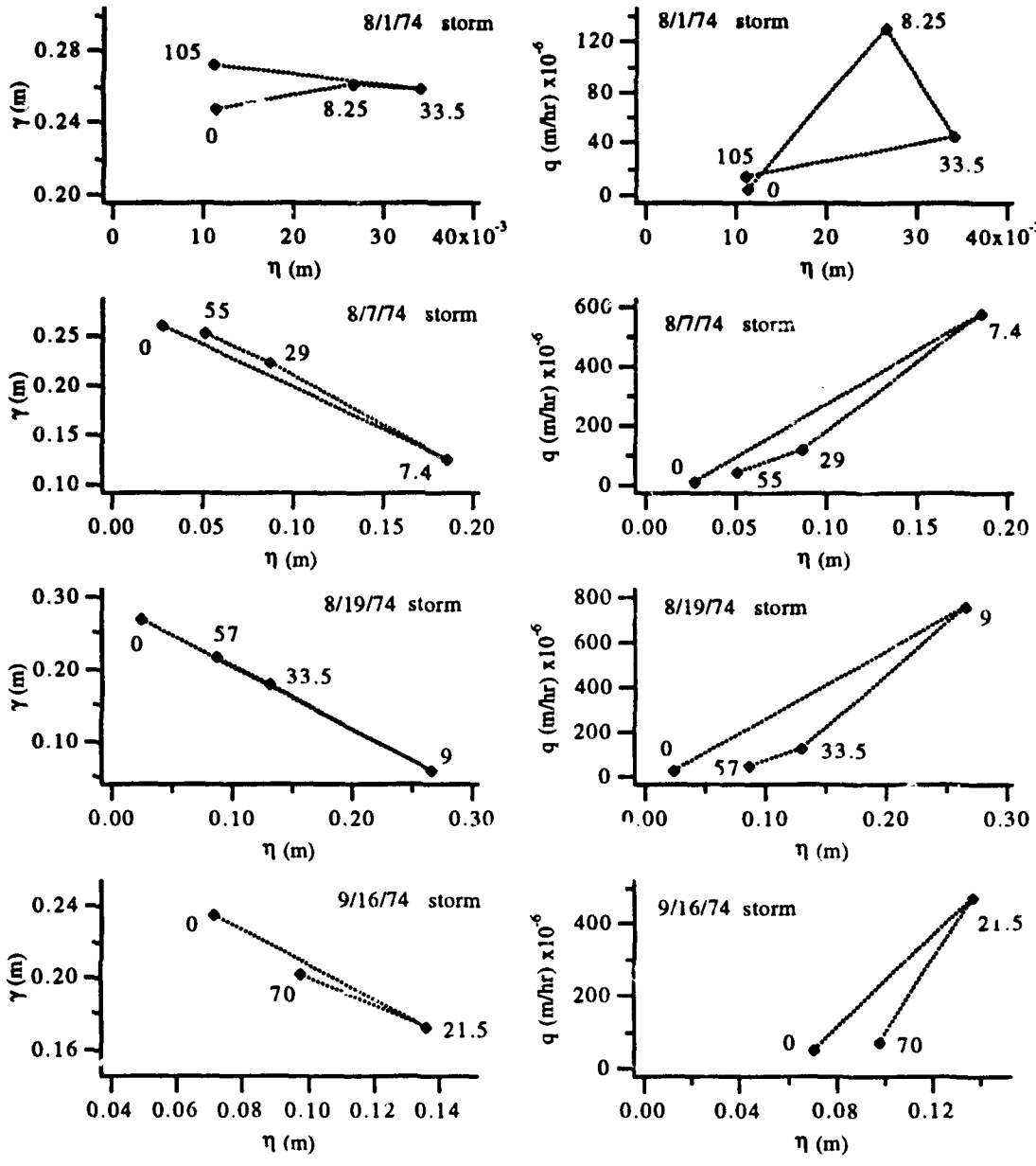

Figure 4.8. The γ-η and q-η phase paths. Numbers denote the position of phase trajectory in hours from the start of rainfall simulation.

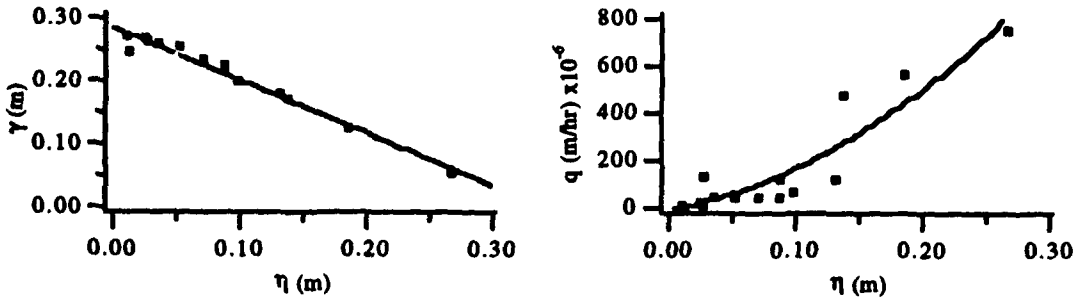

Figure 4.9. The regression relationships for $\gamma(\eta)$ and $q(\eta)$. The solid curve is the fitted polynomial: $\gamma(\eta) = 0.2845 - 0.8334\ \eta$ and $q(\eta) = -8.42157\ 10^{-6} + 0.0009474\ \eta + 0.007914\ \eta^2$.

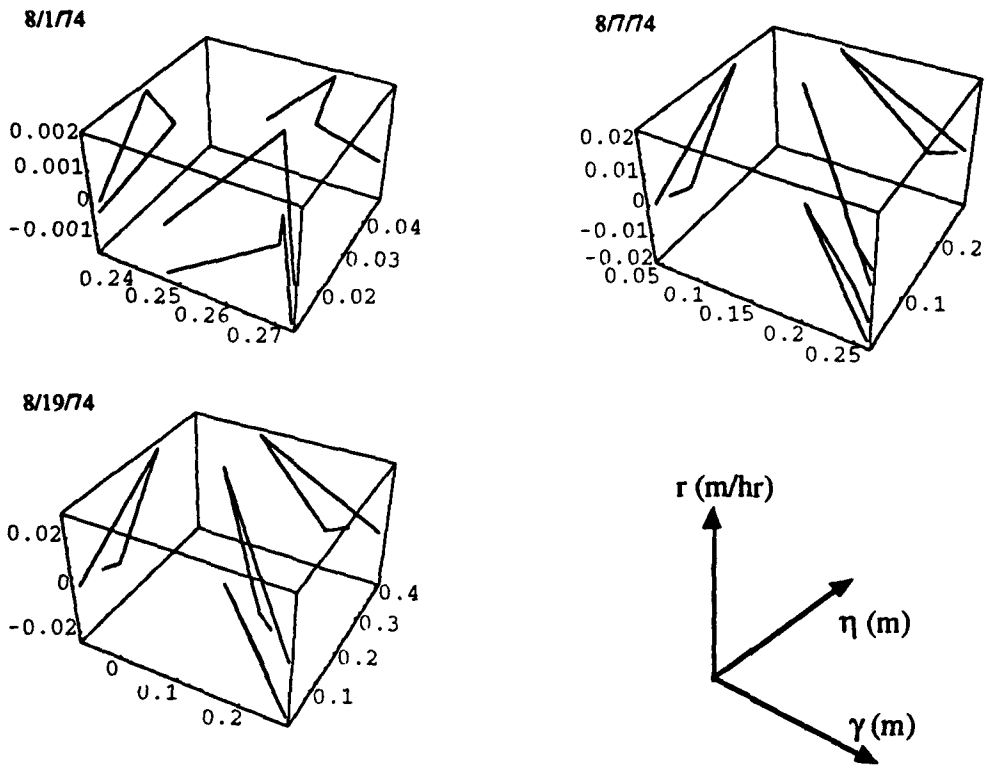

Figure 4.10. The r-γ-η phase-plane trajectory for three storm events.

4.4. Discussion of Results

The single most important result in this analysis of the Shale Hills data, is the observed inverse relationship for the phase-plane trajectory of unsaturated and saturated storage, γ-η. This inverse relationship, also found in the numerical experiments, is the simple result of competition between γ and η for storage volume on the hillslope. The forces governing storage in the unsaturated state (capillarity and gravity), and the forces governing saturated storage (gravity), introduce different time scales of response in each zone.

The dynamic constitutive relationship $q(\eta)$ manifests hysteretic (looping) behavior with a clockwise rotation during storm period. A quadratic polynomial for $q(\eta)$ was determined by regression analysis, and this model should be useful for modeling nonhysteretic subsurface outflow and saturated water storage. However, the role of hysteresis appears to be significant.

It is shown that local similarity of the hillslope shape provides a useful scaling of scattered geomorphic and hydrologic data. Within the conditional similarity region the water table surface is projected onto the unit hillslope geometry, as is the soil moisture. This projection allows the rescaled water table and soil moisture to be fit to a smooth curve, which is integrated over the hillslope.

The different time-scales for rising and recession stages offer some insight into the problem of sampling frequency in the field experiment. The quick response during the storm event requires greater sampling resolution than the drainage period. Comparison of the response time-scales of storage-flux from the Richards equation and from the field data, show that the watershed responds much more rapidly than the numerical model. Since the soil types used in the numerical study are not much different from the soils encountered in the field, the large difference in characteristic times may very well be due to heterogeneity. The effective hydraulic conductivity of the watershed is much higher than would be determined by the texture of the individual soil types. This would suggest that the integrated performance of the hillslope or watershed, and the 'effective' soil hydraulic properties cannot be determined by laboratory (small) samples but must be determined directly in the field. We propose to investigate this in future work.

5. THE TWO-STATE MODEL

5.1 The Two-State Model and its Phase Space

The numerical experiments with the Richards equation, and the interpretation of the Shale Hills field experiment, offer reasonable confirmation that spatially integrated state variables can describe the dynamics of the rainfall-recharge-runoff process. In this section an initial attempt is made at formulating the particular dynamical system. Although the numerical experiments and the field data suggest that nonlinear constitutive relations are ultimately necessary to represent subsurface dynamics, it is always useful to begin with the simplest linearized form. For a linear two-state model, solutions are found for competitive and noncompetitive state variables, responding to varying initial conditions and external forcing (rainfall). Recall that the two-component state-space form of the model is given by

$$\frac{d\gamma}{dt} = i(p,e,t) - r(\eta,\gamma,t) \qquad (41)$$

$$\frac{d\eta}{dt} = r(\eta,\gamma,t) - q(\eta,t) \qquad (42)$$

where $i(p,e,t)$ is surface infiltration rate, or that flux which infiltrates the soil less evaporation, $r(\eta,\gamma,t)$ is the recharge rate per unit surface area to/from the water table, and $q(\eta,t)$ the volumetric subsurface runoff per unit area.

The dynamic behavior of the two-state system is graphically represented by the state-space or time series of $\gamma(t)$ and $\eta(t)$, and by constructing the trajectory of a parametric curve $\gamma(t)$-$\eta(t)$ referred to as the phase space or phase portrait. Figure 5.1 illustrates the two representations of the state variables. The parametric curve γ-η defines the motion or trajectory of the state variables with time implicit for a given initial condition (γ_0, η_0), and is referred to as the phase portrait. All possible trajectories would define the phase space. Both have been used in this report. The next step is to formulate the specific constitutive relations.

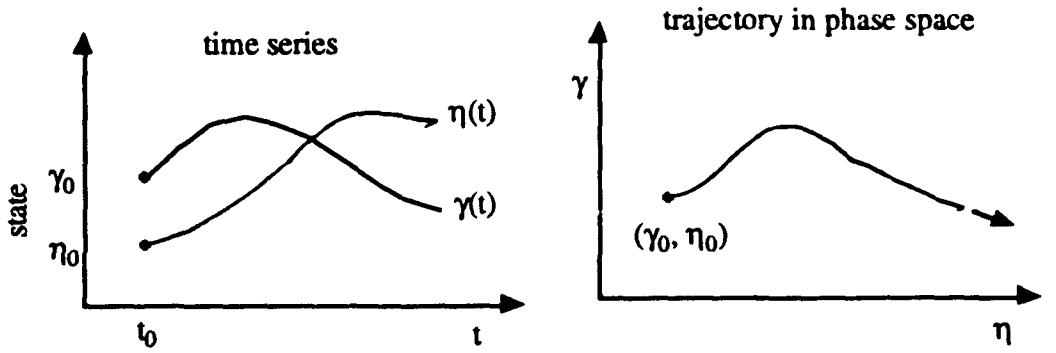

Figure 5.1. Representation in terms of state-space and phase-space.

5.2 Linear Constitutive Relations and State Space

A general two-state linear model has the form

$$\frac{dx_1}{dt} = u_1 + a_{11}x_1 + a_{12}x_2$$
$$\frac{dx_2}{dt} = u_2 + a_{21}x_1 + a_{22}x_2 \qquad (44)$$

The input vector will be simplified in the present case$\{u_1,0\}$, since rainfall u_1 is the only input to the system. First the state variables must also be modified to include residual storage, $x_1=(\gamma-\gamma_o)$ and $x_2=(\eta-\eta_o)$. Residual storage in the case of the unsaturated zone is that depth of water which is held in storage by capillary forces after gravity drainage is complete. The residual storage for the saturated region is that depth of water which exists below local base level. The task of determining the coefficients a_{ij} for the two-state model, relies on determining a series of rate constants, the form of which are determined from the numerical and field experiments.

5.3 Noncompetitive Model for γ–η

The first parameterization makes the assumption that outflow from each storage reservoir is proportional to the remaining storage in that reservoir and that transfer of moisture from one state to the other is also directly proportional. The latter condition implies that increasing moisture in the unsaturated zone should increase recharge to the saturated region. Since there is only a single output to this linear system (neglect evaporation for the time being), the output (subsurface flow to the stream) is linearly proportional to the storage in the saturated reservoir. In standard notation, the coefficients are defined in terms of the rate constants k_{ij}

$$a_{11} = -k_{21} \qquad a_{12} = k_{12}$$
$$a_{21} = k_{21} \qquad a_{22} = -(k_{02} + k_{12}) \tag{45}$$

where the subscript on the rate constants {i,j} represent the direction and origin of the transfer of fluid respectively. The output rate constant from the second reservoir is k_{02}. So this form of the model takes the form

$$\frac{d\gamma}{dt} = p - k_{21}(\gamma - \gamma_o) + k_{12}(\eta - \eta_o)$$
$$\frac{d\eta}{dt} = k_{21}(\gamma - \gamma_o) - (k_{02} + k_{12})(\eta - \eta_o) \tag{46}$$

We can refer to this formulation as 'noncompetitive', since increases in one state variable serves to enhance the other. The equilibrium or steady-state is found by setting the time derivative to zero

$$\gamma = \gamma_o + \frac{p}{k_{21}} + \frac{k_{12}}{k_{21}}(\eta - \eta_o)$$
$$\gamma = \gamma_o + \frac{k_{02} + k_{12}}{k_{21}}(\eta - \eta_o) \tag{47}$$

The direct proportionality of γ–η clearly shows the noncompetitive nature of this parameterization of the model. The single equilibrium or fixed point is given by

$$\gamma(\infty) = p\left(\frac{k_{02} + k_{12}}{k_{21}k_{02}}\right) + \gamma_o$$
$$\eta(\infty) = \frac{p}{k_{02}} + \eta_o \tag{48}$$

The general form of the solution for (46) when p=0 is given by

$$\bar{x}(t) = \alpha_1 e^{\lambda_1 t}\bar{c}_1 + \alpha_2 e^{\lambda_2 t}\bar{c}_2 \tag{53}$$

where $\{x_1, x_1\}$ are the state variables, $\{\alpha_1, \alpha_1\}$ are scalars determined from initial conditions, $\{\bar{c}_1, \bar{c}_2\}$ are the eigenvectors of the coefficient matrix (45), and $\{\lambda_1, \lambda_2\}$ are the corresponding eigenvalues. In this case we require that λ_i be real and negative for the solution to be stable.

The phase portrait for a range of initial conditions and the indicated parameters is shown in Figure 5.2. The phase portrait represents all possible solutions, including some that are clearly not physically plausible. The time series for a particular initial state is shown in Figure 5.3. In the next section, the results of the noncompetitive model will be compared with the case where soil moisture and saturated storage compete for the same hillslope storage volume.

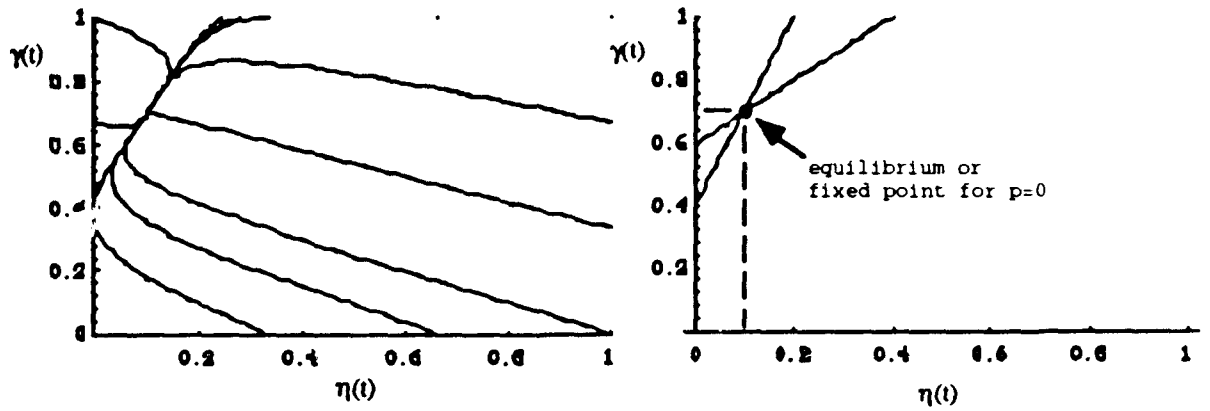

Figure 5.2 The phase portrait for the noncompetitive model with the following parameters: k_{12}=0.1, k_{21}=0.1, k_{02}=0.2, p=0.02, γ_o=0.7 and η_o=0.1.

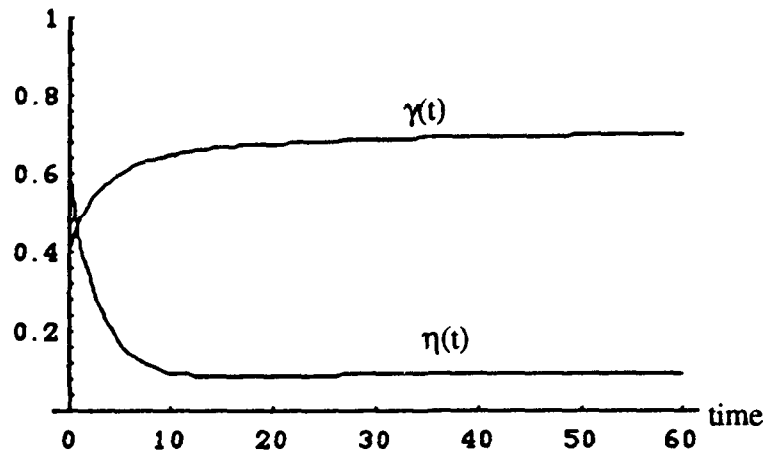

Figure 5.3 The time series for same parameters as in Figure 5.2 but with initial conditions $\{\gamma_o=.6,\eta_o=.4\}$.

5.4 Competitive Model for γ–η

Introducing competition between state variables simply means that increasing the storage in one reservoir will cause a decrease of storage in the second reservoir. Recall that both the numerical experiments and the Shale Hills field data exhibit an inverse relationship for γ–η, except during very dry conditions. The concept of competition may be counterintuitive at first, until we recall that the state variables represent the average or total moisture in each reservoir. Under well-drained conditions, the saturated storage is at its lowest point, $\eta \to \eta_o$, while the moisture store may be at a high level. During a storm, infiltration increases the soil moisture at first, but at some later time, the water table begins to capture the soil moisture volume. Below the root zone, the initial unsaturated volume

contains substantial moisture. Thus, a small amount of recharge may produce a rapid increase in the water table, and effectively reduce the volume of moisture in storage in the unsaturated zone. However, both the numerical and field experiments suggest that, during the early part of the event, both reservoirs increase. The transition from noncompetitive to competitive state variables is an important concept, which we examine next.

The coefficients are again defined in terms of rate constants k_{ij}

$$\begin{aligned} a_{11} &= -k_{21} \qquad a_{12} = -k_{12} \\ a_{21} &= k_{21} \qquad a_{22} = -(k_{02} - k_{12}) \end{aligned} \tag{49}$$

Note that this version of the model is only different in that k_{12} has changed sign. The dynamical model for competition between state variables takes the form

$$\begin{aligned} \frac{d\gamma}{dt} &= p - k_{21}(\gamma - \gamma_o) - k_{12}(\eta - \eta_o) \\ \frac{d\eta}{dt} &= k_{21}(\gamma - \gamma_o) - (k_{02} - k_{12})(\eta - \eta_o) \end{aligned} \tag{50}$$

The equilibrium or steady-state is again found by setting the time derivative to zero

$$\begin{aligned} \gamma &= \gamma_o + \frac{p}{k_{21}} - \frac{k_{12}}{k_{21}}(\eta - \eta_o) \\ \gamma &= \gamma_o + \frac{k_{02} - k_{12}}{k_{21}}(\eta - \eta_o) \end{aligned} \tag{51}$$

The single equilibrium or fixed point for this linear system is given by

$$\begin{aligned} \gamma(\infty) &= p\left(\frac{k_{02} - k_{12}}{k_{21}k_{02}}\right) + \gamma_o \\ \eta(\infty) &= \frac{p}{k_{02}} + \eta_o \end{aligned} \tag{52}$$

The general solution for (50) when p=0 is given by

$$\bar{x}(t) = e^{\sigma t}\{\zeta_1 \cos(qt) + \zeta_2 \sin(qt)\} \tag{53}$$

where the eigenvalues in this case may be complex $\lambda_i = \sigma \pm iq$, and the coefficients $\{\zeta_1, \zeta_2\}$ are related to the eigenvectors of the coefficient matrix (49). As long as the real part of λ_i is negative, the solution is stable. The reader is referred to Beltrami (1987) for details of the dynamic modeling approach.

The phase portrait for a range of initial conditions and the indicated parameters is shown in Figure 5.4, and we see that the solution takes the form of a spiral as it approaches the single equilibrium point. The phase portrait represents all possible solutions for the given parameter set, including some that are not physically plausible. It should be noted, that the addition of nonlinear constitutive relations will be necessary to constrain the nonphysical trajectories, or those where the state variable is negative. The time series for a

particular initial state of the competitive model is shown in Figure 5.5. Note the substantial change in response.

Although our numerical and field experiments show that nonlinearity is the rule rather than the exception, the linear models outlined here provide a first step towards understanding the physical mechanisms operating as they are expressed by integral variables of the hillslope system. Future work will explore in much greater detail the general nonlinear form of the dynamical model.

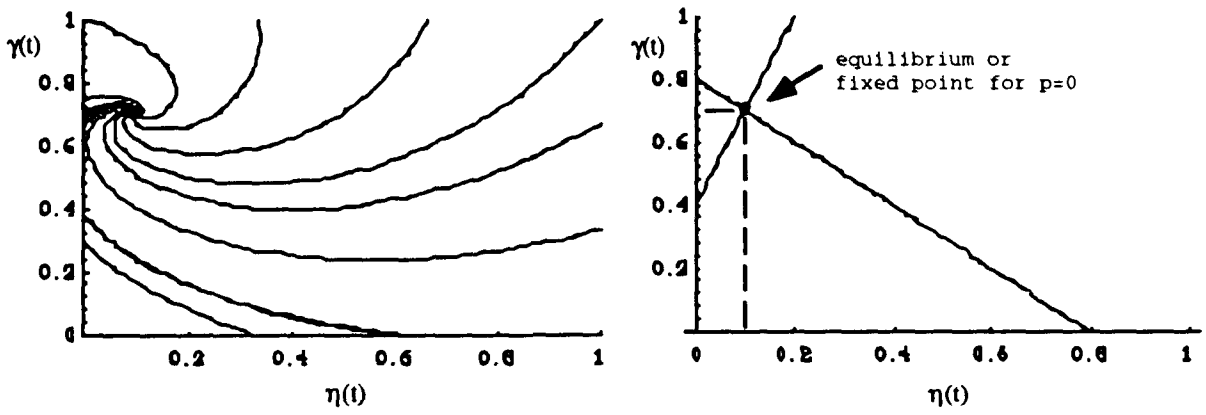

Figure 5.4 The phase portrait and equilibrium or fixed point for the competitive model with the following parameters: k_{12}=0.1, k_{21}=0.1, k_{02}=0.2, p=0.02, γ_o=0.7 and η_o=0.1.

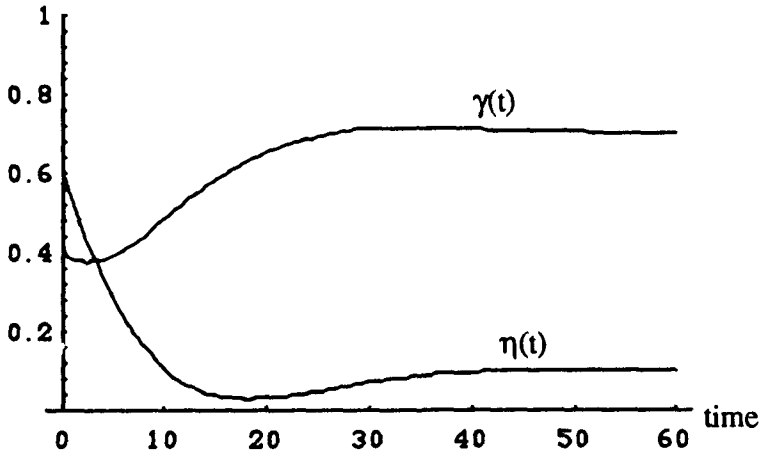

Figure 5.5 The time series for the competitive model with same parameters as in Figure 5.4 but with initial conditions $\{\gamma_o$=.6,η_o=.4$\}$.

6. DIGITAL ELEVATION DATA AND TOPO-HYDROLOGIC STRUCTURES

6.1 Fractal Topography and Similarity Regions

As part of this research an initial attempt was made to examine similarity of digital topography, and the scale over which similarity might be expected. It has been proposed that scale invariance of random topographic surfaces represents a fundamental characteristic of landform texture and thus classification (Turcotte, 1992, Mandelbrot, 1985, others). Digital topography for two 7.5 min. quadrangles, one in the Colorado Plateau, and one in the Appalachian Plateau were used. As part of the analysis, algorithms were developed to analyze the data, and these are described below. Although the analysis was limited in scope, the results point to a critical avenue for future research.

An elementary characterization of random surface texture requires two parameters, the relative roughness or variance of the surface, and the distribution of variance with map scale. For a self-affine surface z(x,y), these properties are measured by the root-mean-square roughness, σ_z and the exponent β of the variance spectrum $\Gamma(k;\beta)$, where the spectrum has the form

$$\Gamma(k) \sim k^{-\beta} \qquad (54)$$

For this model of topography, the parameter β represents the way that variance is distributed with wave number k or wavelength, $k^{-1}=\lambda$. σ_z and β may also be thought of as the scale and shape parameters respectively, of the correlation structure in z(x,y). A useful property of the spectrum is that integration over wave number k defines the overall variance of the surface, or in terms of the rms roughness

$$\sigma_z = \left(\int_{k_o}^{k_1} \Gamma(k) dk \right)^{1/2} \qquad (55)$$

where k_o is the smallest and k_1 is the largest wave number to exhibit self-affine scaling. A relation between roughnes σ_z and map length can be determined by integrating (54) (Power and Tullis, 1988)

$$\sigma_z = \left(\frac{a}{\beta - 1} \right)^{1/2} L_o^{(\beta-1)/2} \qquad (56)$$

where a is a constant, and $L_o=1/k_o$ is the longest wavelength over which the scaling behavior is observed. The fractal dimension D for the surface can be expressed in terms of the spectral slope β

$$D = \frac{7-\beta}{2}. \qquad (57)$$

A spectral estimation algorithm was developed in MATLAB based on the 2D fast fourier transform. The field was assumed to be statistically isotropic, and the radial-symmetric spectral estimate was determined. By plotting $\ln \hat{\Gamma}$ versus $\ln k$ for a subset of the DEM, the spectral slope and fractal dimension (57) were estimated and a comparison of the distribution of values were made. In this example two 7.5 minute USGS DEM's are examined, one located in the Colorado Plateau near Price, Utah and a second in the Appalachian plateau in northwestern Pennsylvania. Each spectrum estimate was determined for a 120x120 grid subset of the DEM, and the results are shown in Figure 6.1. The approximate upper and lower cutoff frequencies are indicated and the mean fractal dimension D and β is given. As the grid interval is approximately 30 meters the maximum length scale of similarity k_o^{-1} is L_o~2km, and the minimum length scale k_l^{-1} appears to be on the order of L_l~100m.

Although this is only a preliminary analysis based on a small amount of digital topography, the fractal dimension and spectral slope really do not vary all that much for these cases. Future work will expand this phase of the study and in particular to examine 5 m digital data. Understanding the transition of similarity relationships from the hillslope to watershed scale will require greater detail in the topographic data. A future goal is to examine multi-scale hypsometric relationships from the digital topography.

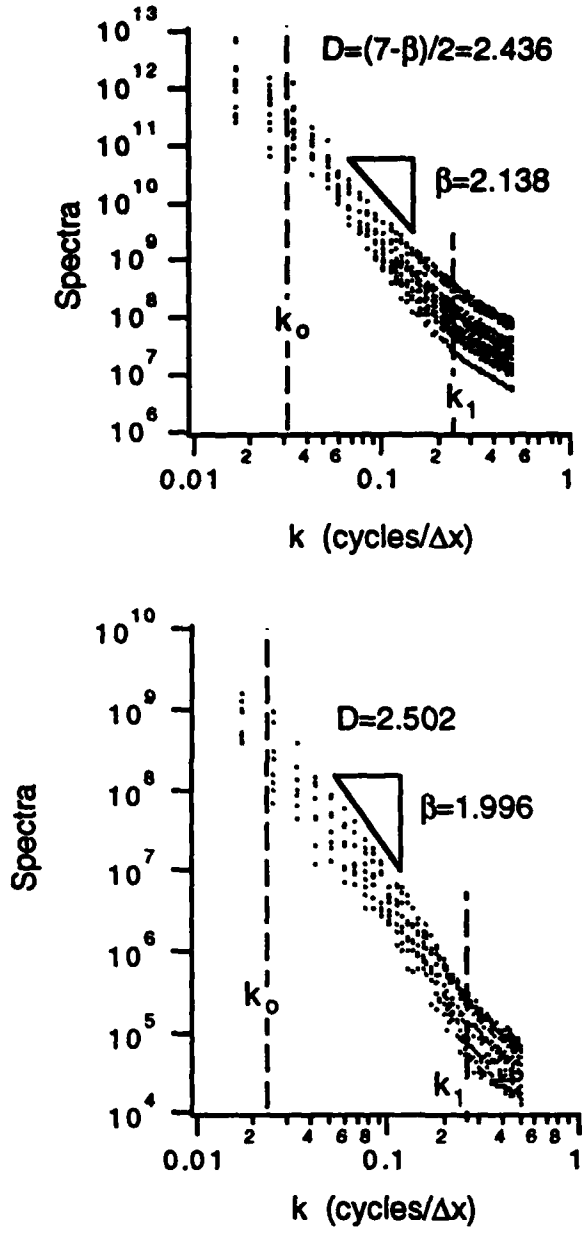

Figure 6.1. The estimated spectra for Slate Run PA. and Wellington, UT for 7.5 minute quadrangle. Each trace represents a 120x120 subgrid from the DEM.

6.2 Application to Climate Variables in Mountainous Regions

In chapter 2 we considered a general space-time representation for the state variable $y(\bar{x},t)$ of the form

$$y(\bar{x},t) = \sum_{k=1}^{\infty} y_k(t)\alpha_k(\bar{x}) \qquad (3)$$

where $y_k(t)$ represents the k_{th} amplitude and $\alpha_k(\bar{x})$ are the corresponding spatial shape functions with respect to the vector of independent variables or coordinates $\bar{x}=\{x_1,x_2,x_3\}$. From (3) the problem is to determine the 'effective' dimension of the independent variables, and their corresponding shape functions. A good example is the distribution of precipitation and temperature in mountainous regions, where the climatic variables are often reduced to simple functions of elevation. Let's say that our state variable y is a function of two independent coordinates, elevation and aspect or azimuth (ϕ,θ), and further that y is a stationary process in time. The process $y(\phi,\theta,t)$ is then decomposed into a time average $(\bar{y})$ and a stationary time-fluctuation (y')

$$y(\phi,\theta,t) = \bar{y}(\phi,\theta) + y'(\phi,\theta,t) \qquad (58)$$

where the time average $\bar{y}(\phi,\theta)$ is a function of elevation (ϕ) and aspect (θ), while the perturbation $y'(\phi,\theta,t)$ varies with elevation, aspect and time. Now let y', have the expansion

$$y'(\phi,t) = \sum_{k} y_k(t)\alpha_k(\phi) \qquad (59)$$

where $y_k(t)$ is a zero mean stationary process in time representing stationary harmonic and/or random contributions to the overall process, and $\alpha_k(\phi,\theta)$ represents the basis functions or shape functions for the same component of the y fluctuation. The y-process now has the representation

$$y(\phi,\theta,t) = \bar{y}(\phi,\theta) + \sum_{k} y_k(t)\alpha_k(\phi,\theta)\ . \qquad (60)$$

The hydrologic problem is: How does one determine the shape functions $\alpha_k(\phi,\theta)$ from time series measurements of y?

As an application of (60), Fan and Duffy (1993) applied the decomposition (60) the seasonal structure of monthly temperature (T) and precipitation (P) records for the Wasatch Front area of north-central Utah. Each time series was expressed as the sum of a long term mean, a seasonal cycle, and a residual stochastic process. In this example the shape functions were assumed to be only functions of elevation, as all climate stations were located on the western slopes of the Wasatch. They then examined the elevation dependence of the mean, the amplitude and phase of Fourier harmonics associated with the seasonal cycle, and the variance, autocorrelation and skew of the residual process. Based

on correlation with elevation and each of the above parameters, a simple parametric model of T and P as a function of elevation (z) and season (t) is developed, which preserves the seasonal variability in the data. The model provided an empirical method for estimating spatially-distributed and time-variable climatic input patterns from point observations. The application demonstrated that seasonal trajectory of the P(z,t)-T(z,t) phase portrait can be diagnostic of synoptic climate conditions for interpretation of large seasonal variations about the normal mean conditions. Finally, the model is applied to digital elevation data (DEM) of the Wasatch Front area, to generate seasonal animations of temperature and precipitation fields. The emphasis in this study is placed on the space-time structure in historic records and proposing an empirical method to incorporate such structures.

6.3 Estimating Precipitation-Temperature Shape Functions

One expects the mean temperature, μ_T, to decrease with elevation in a manner close to the lapse rate, and the mean precipitation, μ_P, to increase with elevation as a result of the orographic effect. Figure 6.2 and 6.3 illustrate monthly time for temperature and precipitation at three elevations, along with their spectra. Fan and Duffy attempted to determine whether higher statistical moments, namely the variance and skew, might also be functions of altitude. The variance of the climate time series was further decomposed into the contributions from seasonal harmonics. The state variables have the form

$$T(z,t) = \mu_T(z) + \sum_{i=1}^{m} \alpha_{T_i}(z)\ \cos\{2\pi i f_o[t + \varphi_{T_i}(z)]\} + N[\sigma_T(z), \beta_T(z), \vartheta_T(z)] \qquad (61)$$

$$P(z,t) = \mu_P(z) + \sum_{i=1}^{m} \alpha_{P_i}(z)\ \cos\{2\pi i f_o[t + \varphi_{P_i}(z)]\} + N[\sigma_P(z), \beta_P(z), \vartheta_P(z)] \qquad (62)$$

where the noise parameter is a function of the residual variance, the spectral slope, and the skew coefficient respectively. Each parameter in (61) is estimated from the data and plotted against elevation as shown in Figure 6.4. Note that each data point represents a climate record. The upper-left plot indicates that monthly mean temperature decreases with elevation at a rate of 6.06^{o}C / 1000m., slightly lower than the sea-level-average lapse rate of 6.5oC / 1000m. The upper-right plot gives the amplitude of the first three harmonics used to describe the seasonal cycle. Three harmonics are found to be the maximum number needed to meet the criteria. The plot shows no elevation dependence for the second harmonic (f=1/6 cpm, cycle per month). For the first (f=1/12 cpm) and the third (f=1/4 cpm), the amplitude decreases with elevation, or at higher elevations one observes less seasonal difference, and the air stays relatively cool all year round. The larger seasonal amplitude at low elevation may also reflect the winter inversion which causes cooler winter

temperature. The middle-left plot shows a lack of elevation dependence for all three phase components. On the average, the peak occurs in the 7th month (July, warmest month) for the first harmonic, the 5th month (May) for the second, and between the 3rd and 4th month (late March to early April) for the third. The variance of residual noise is given in the middle-right plot, and it shows large scatter and a weak correlation with elevation. The lower-left plot gives the distribution of the absolute values of spectral slope for the residual noise. The lower-right plot shows the elevation distribution of the skew coefficient for the noise process, which indicates cooler (than the mean T) in the valley and warmer (than the mean T) at higher altitudes.

Figure 6.5 illustrates the elevation distribution of precipitation moments. The upper-left plot is the long term mean monthly precipitation, fitted to a linear variation with elevation. The upper-right plot gives the amplitude of the first five harmonics used to describe seasonal oscillations. The residual contribution to the variance is higher for precipitation than for temperature (0.1%). Five harmonics are found to be the maximum necessary. The plot shows that only the first (f=1/12 cpm) and the third (f=1/4 cpm) harmonics have a significant elevation effect. The general increase of seasonal fluctuation with altitude can be explained as follows (Williams and Peck, 1962). In the Great Basin region, precipitation in winter is mostly of frontal type, resulting in a strong orographic signature. In the summer months, precipitation is primarily from local convective thunderstorms, without apparent elevation effects. At the watershed scale, this leads to a small seasonal difference in precipitation at low elevation, and a large seasonal difference at high elevation. The middle-left plot shows the phase relationship for the five harmonics. No significant altitude correlation is found except for the first harmonic (f=1/12 cpm), whose peak comes between the 12th and the 1st month (December to January), the season when frontal storms from the North Pacific are most active. The second harmonic (f=1/6 cpm) appears to be related to a large scale low-pressure cell called the Utah-Nevada Low (Jeppson, et al., 1968) that occurs in the late spring months (April to May) and the mid-fall season (October), a period of widespread thunder-storms. The middle-right and lower-left plots give the variance and the spectral slope b of the residual series. It is observed that the variance and the persistence of the residual stochastic process increase with altitude. The lower-right plot shows the large, positive skew coefficient in the residual noise at all sites and the lack of elevation dependence. Large positive skew coefficient is a characteristic of many hydrologic processes in a desert environment, such as streamflow generated from isolated, large-magnitude storm events. The relatively long inter-storm periods effectively lowers the mean value.

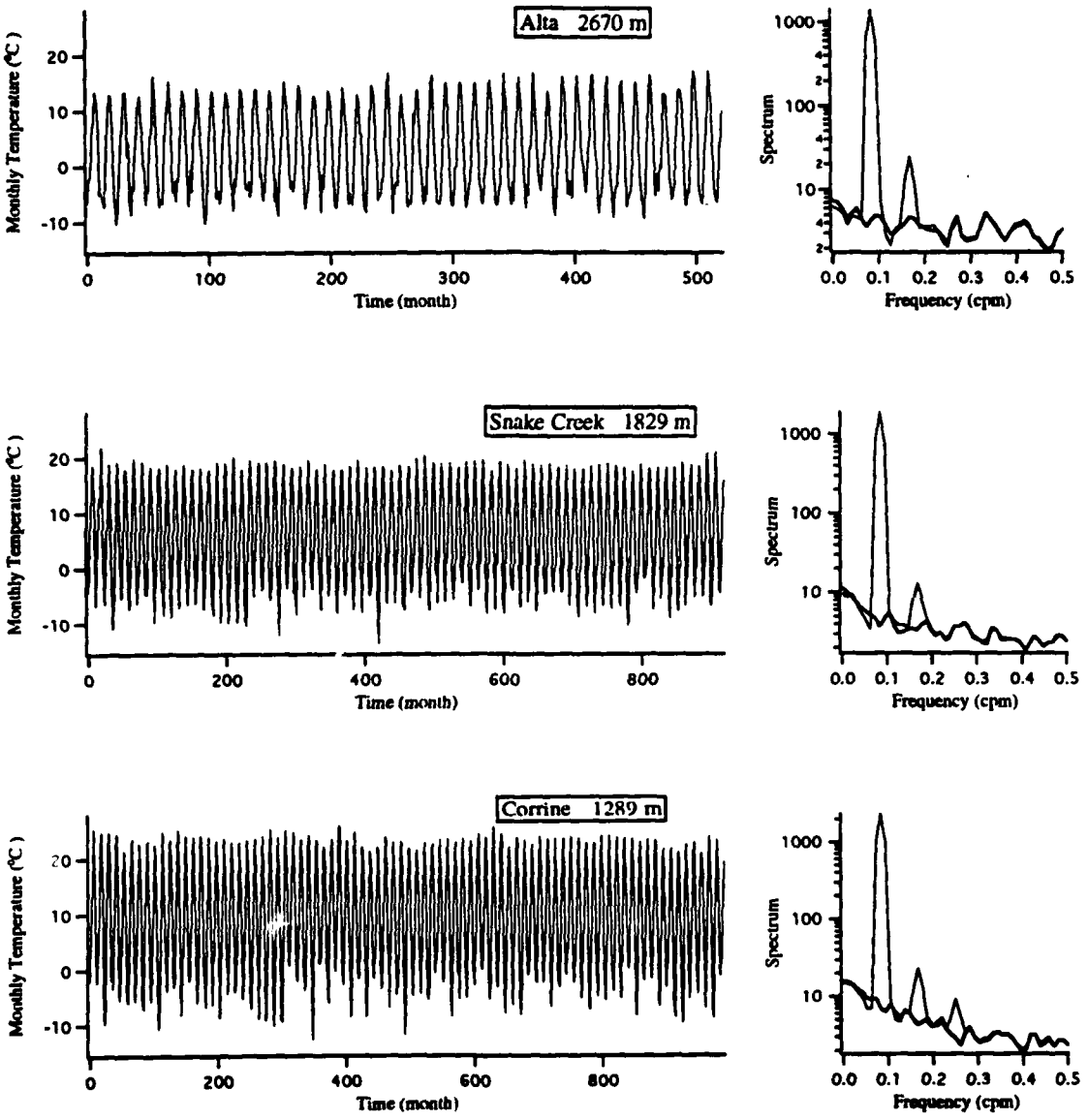

Figure 6.2 Monthly temperature time series at three elevations and their spectra before (thin line) and after (thick line) seasonal cycle is removed (cpm is cycles per month).

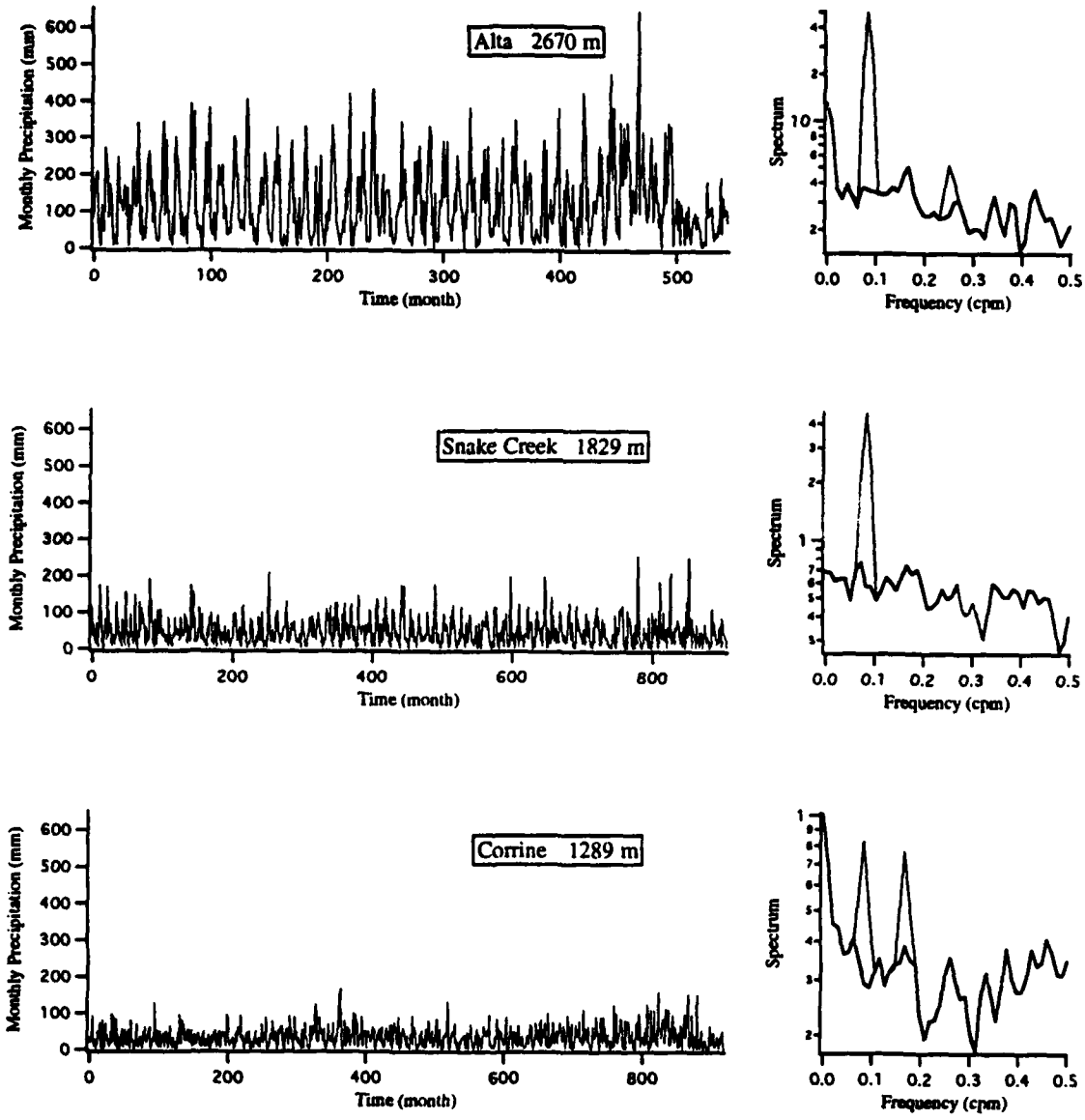

Figure 6.3 Monthly precipitation time series at three elevations and their spectra before (thin line) and after (thick line) seasonal cycle is removed (cpm is cycles per month).

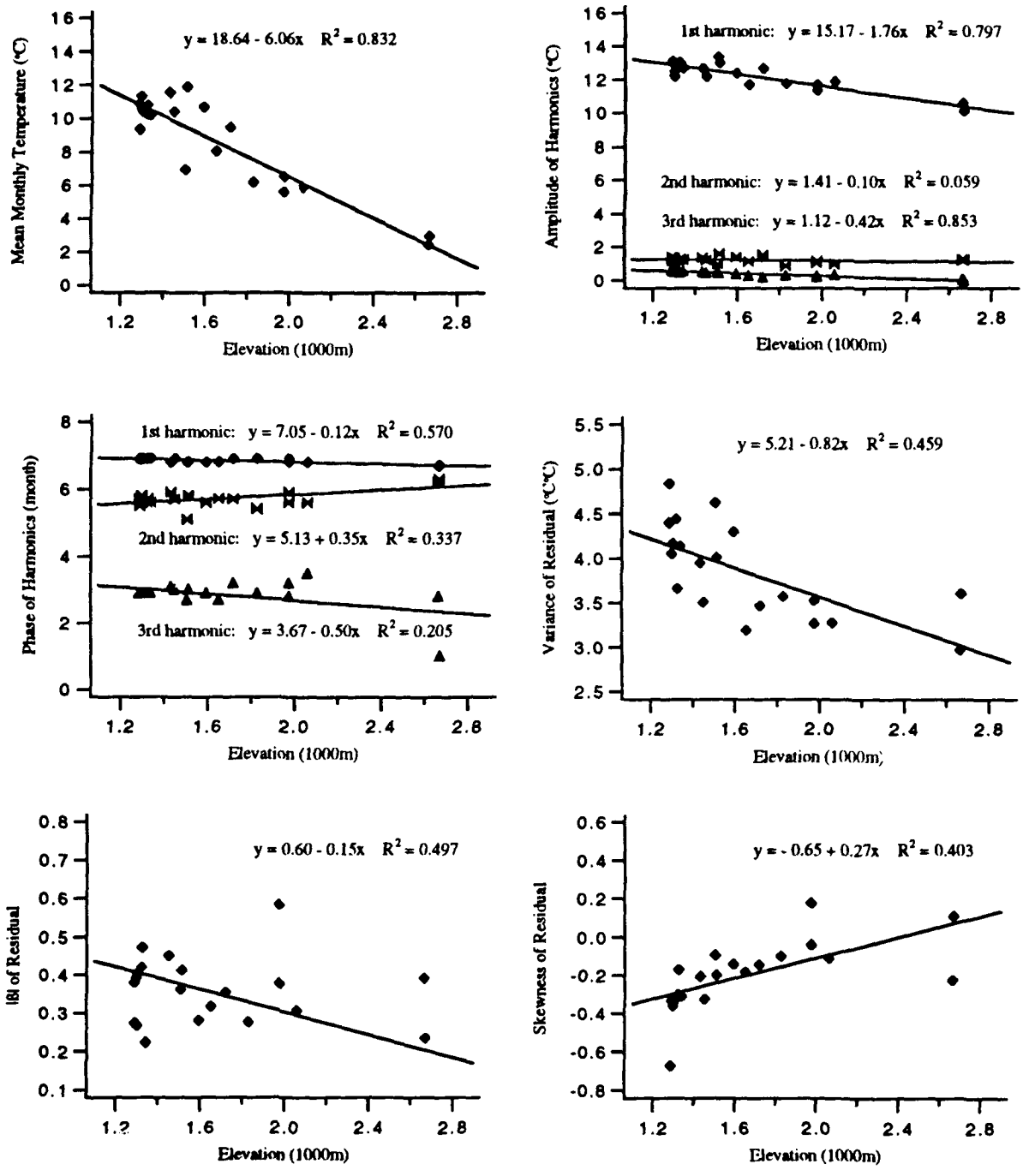

Figure 6.4 Elevation dependence of the temperature model parameters in (61).

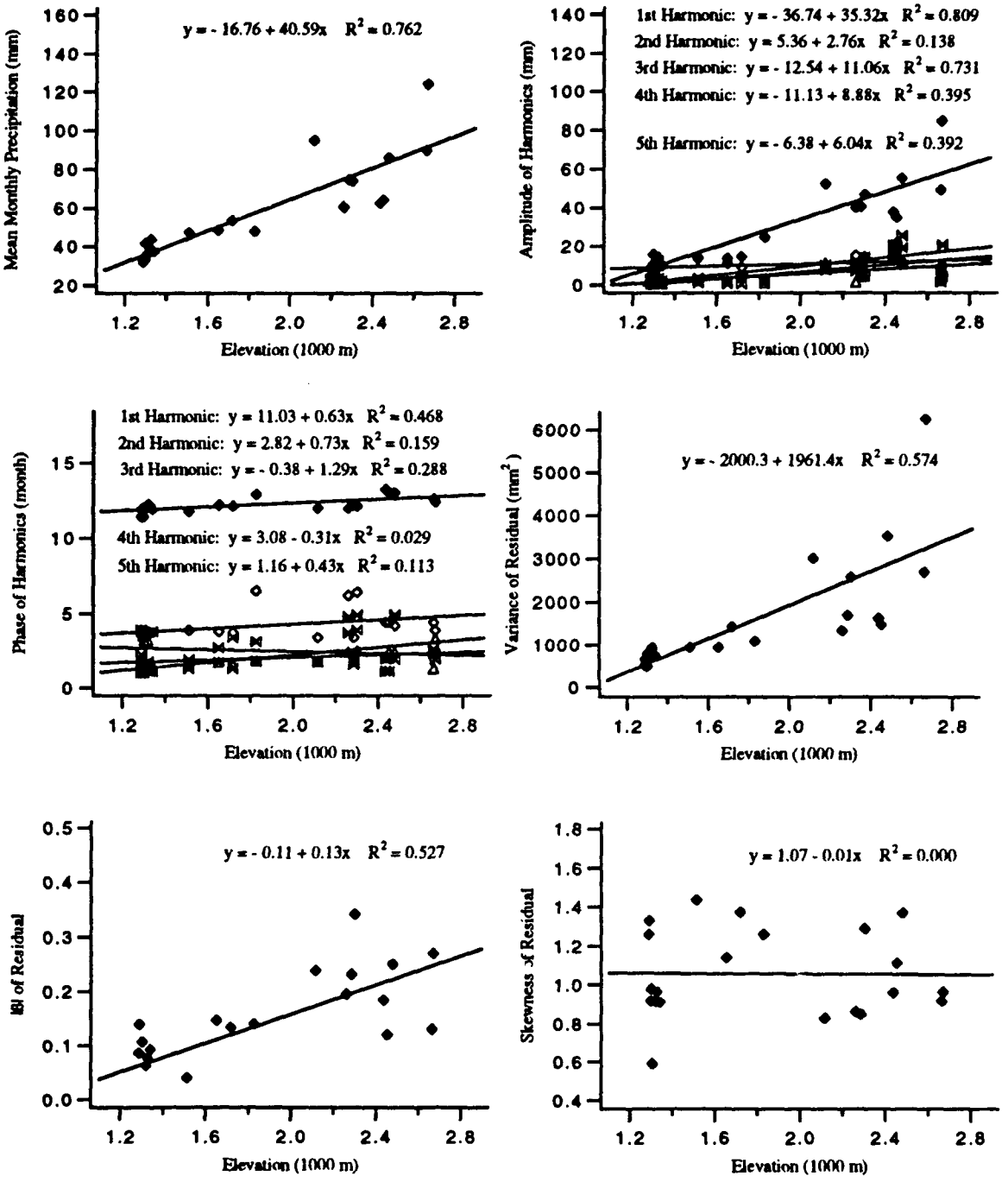

Figure 6.5 Elevation dependence of the precipitation model parameters in (62).

6.4 P-T Phase Portrait and Animation from Digital Topography

The phase portrait, or temperature-precipitation trajectory, is a useful tool for interpretation of seasonal climate conditions. Figure 6.6 illustrates the P(z,t)-T(z,t) trajectory at two elevations on the Wasatch Front. Plotted on the horizontal axis is the first two terms of equation (61), that is the mean plus seasonal harmonics of temperature. The vertical axis represents the first two terms of equation (62), or the mean plus seasonal harmonics of precipitation. The dashed line represents the trajectory of the mean precipitation-temperature relation with elevation. At an elevation of 1,289m (Salt Lake City) the monthly mean temperature is 10.8°C and precipitation 35.6 mm/mo. Note the large annual range in temperature and the small range in precipitation at this low elevation, as shown earlier in Figures 4 and 5. The wettest month is April, likely a consequence of the large scale low pressure system, the Utah-Nevada Low, also mentioned earlier. The low pressure system is reestablished in October, causing a second peak of precipitation. The strong winter frontal storms certainly have a very small contribution at this low elevation.

At 3,048 m (near the peaks of the front), the mean monthly temperature cools to 0.2°C with mean precipitation increasing to 107. mm/mo. Note three features as compared to the trajectory at 1,289 m. First, it has a smaller temperature and larger precipitation range. Second, the direction of the trajectory is reversed. While spring is wetter than fall at 1,289 m, the opposite is true at 3,048 m. Third, the wettest month is February. Each these features can be attributed to strong winter frontal storms and orographic lifting. At high elevation, precipitation has a larger winter-summer ratio, a shift of its peak toward the winter months and thus a wetter fall season. The moderately wet April and October may again reflect the effect of the Utah-Nevada Low system.

Finally, Fan and Duffy show how the approach can be used in visualization of expected temperature and precipitation fields using digital topography. Each field is generated by applying (61) and/or (62) to elevation values z(x,y) for a given month (t). The results are shown as 3-d maps for January, April and August in Figure 6.7for the Wasatch Front region. From the spatial fields the effect of elevation on monthly precipitation totals is strongest during the winter months, with a relatively weak orographic effect in the summer months. Monthly average temperature exhibits large elevation differences during the summer with much less variation in the winter.

It is our view that the phase portrait trajectory together with the generated fields from the DEM serve as a simple way of visualizing spatio-temporal (seasonal) climatic

patterns in mountainous regions. Extension of the above approach to include aspect will be attempted in future work.

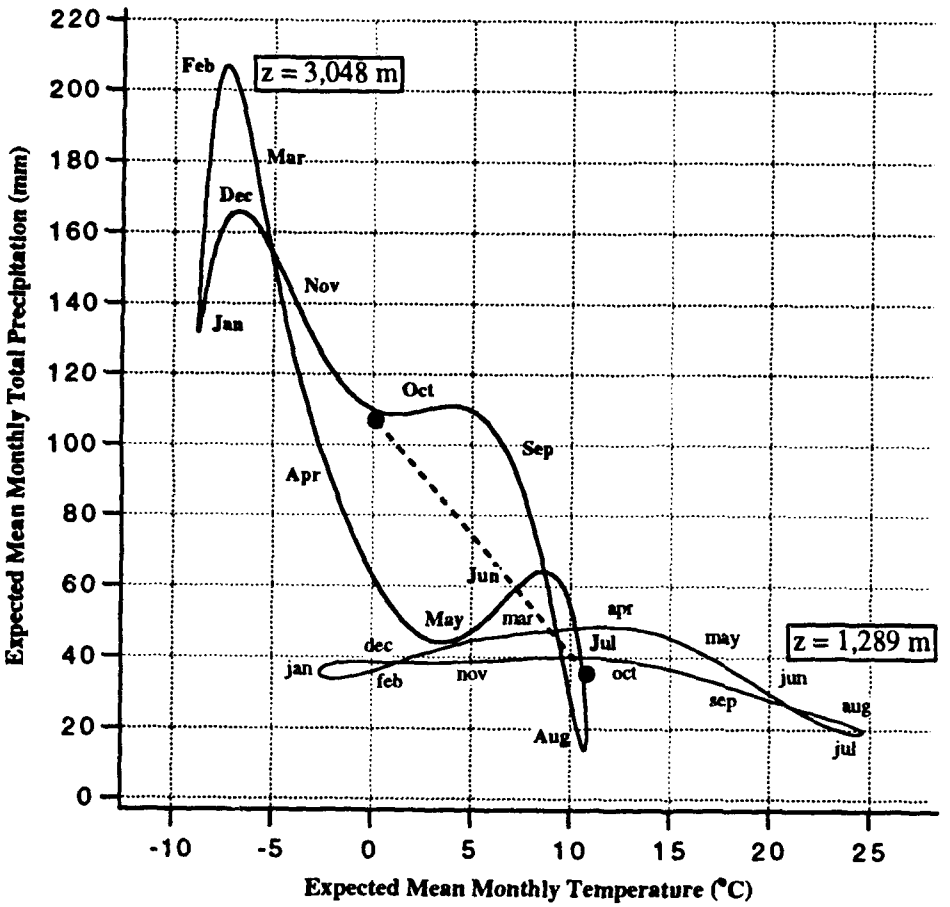

Figure 6.6 The phase portrait for the trajectory of the monthly precipitation versus temperature at two elevations and the trajectory of the time average precipitation with elevation.

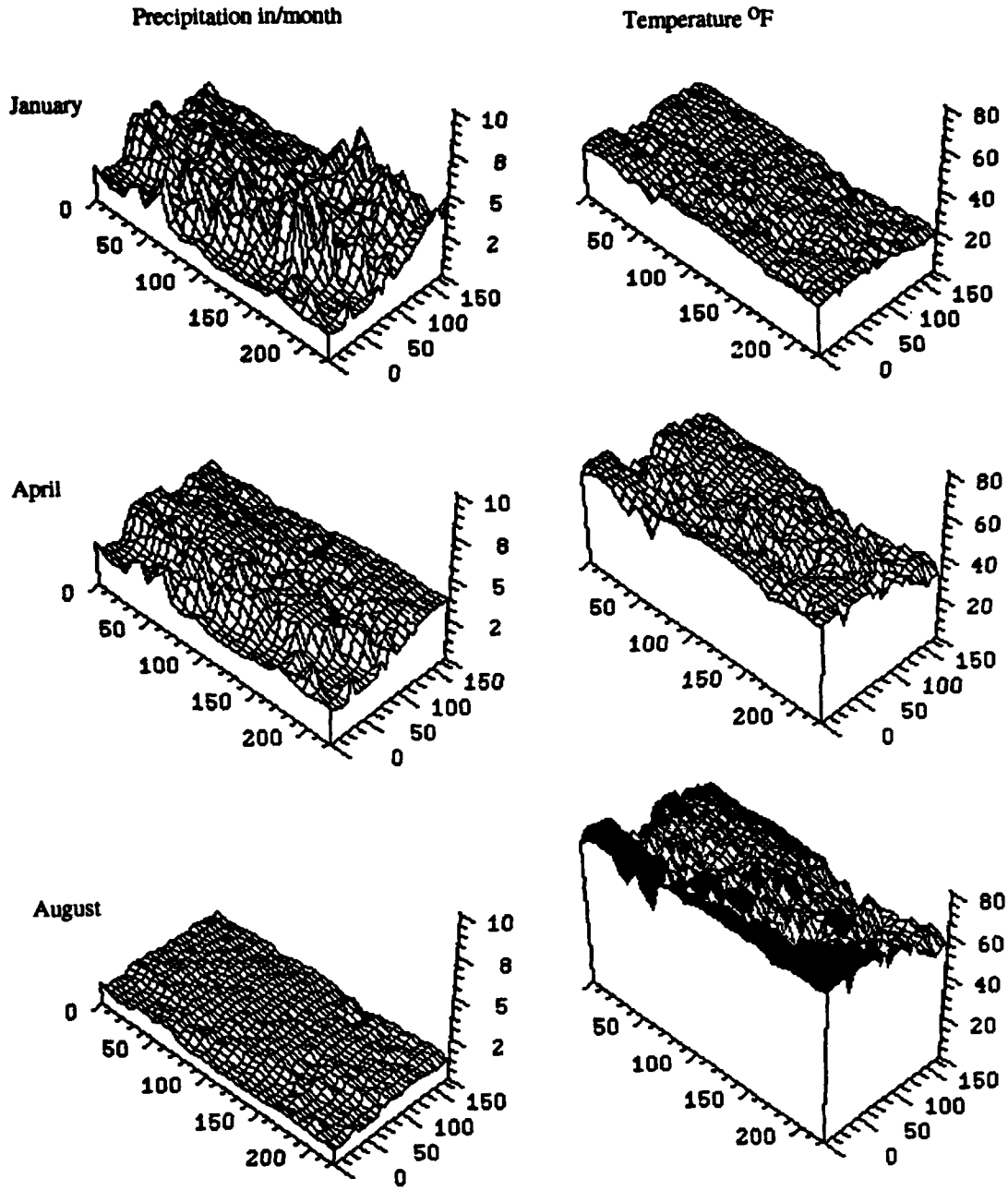

Figure 6.7 January, April, and August temperature and precipitation fields generated from the empirical model (61)-(62) and digital topography of the Wasatch Front (after Fan and Duffy, 1993).

CHAPTER 7. PHILOSOPHY

In recent years national and international efforts have focused on advancing the fundamental understanding of the physical processes governing the circulation of water in the soil-groundwater-stream system. Today it is clear that the complexities of the issue go beyond narrowly defined and traditional scientific and engineering disciplines, requiring a multidisciplinary approach. From our perspective, two themes have emerged which have the effect of unifying the seemingly endless categories of problems concerning the hydrologic models on natural landscapes. The first is that applied mathematics and numerical and symbolic computation are the centerpiece of environmental problem solving and provide a framework upon which experimental pattern and predictability may emerge from a complex environmental system. The second theme has to do with the question of scale. We know that regularities and patterns in hydrologic and environmental quality observations can be found at all scales of measure, and that the public and private demand is for prediction of hydrologic response over a wide range of scales: from soil horizons and fields or hillslopes, to geologic formations and watersheds, to physiographic regions and whole river basins. Current predictive models typically rely on laboratory or small-scale empirical relations, while field-scale predictions are made outside the range of measured conditions. That is, extrapolation of small or local scale 'laws' (e.g. Darcy's law, Fick's law, solute adsorption isotherms etc.) are assumed to be representative at the larger scales. The current predictive capability has served many useful purposes, but greater precision, reliability and integration are required if progress is to be made towards regional and global problems of water resources and environmental quality management.

The fundamental challenge of environmental/hydrologic science and engineering is to extend our predictive capabilities from fluid flows at the laboratory and local scale to length scales more pertinent to the cycle of water on landscapes such as individual watersheds and aquifers (1-10's km), collections of watersheds and river basins (>100 km). This opportunity was recently recognized by the National Academy of Sciences/National Research Council report "Opportunities in Hydrologic Science", where it is pointed out that hydrologic science is particularly lacking in theoretical and experimental knowledge across scales. In our opinion this requires a new view of the relation between hydrologic and environmental quality data and models, where on the one hand models and numerical experiments are used to guide the collection of relevant data, and on the other where data obtained across multiple scales is integrated into a relevant information base necessary for prediction and control. This approach of course is not new to atmospheric science where an international network of observations has supported the critical modeling

effort of weather prediction. Only in recent years has the US observation-network for hydrologic and environmental quality data (e.g. NAWDEX, STORET, LANDSAT, digital elevation data,...) reached a point where integration of observations and models can begin for the terrestrial component of the hydrologic cycle. It is hoped that the spirit of the research conducted through the present research grant funded by ARO to Penn State University, reflects this consensus of the scientific community. We realize that the scope of this research effort reported here is comprehensive, and yet incomplete in technical details. We can only reply that the problem of rainfall-storage-runoff is comprehensive in its complexity and incomplete in its understanding.

7.1 Research Directions

The goal of determining the essential spatial and temporal structure of hillslope, watershed, and river basin dynamics using low-dimensional models, recognizes the extraordinary computational demands of modeling the rainfall-storage-runoff processes where topography, soil, geology and climate variability, necessitates an "effective" representation. In this research we have examined the practical hypothesis that low-dimensional models (e.g. a few state variables) are predictive.

A range of questions remain concerning the low dimensional model proposed above, namely: Under what conditions are spatial averages sufficient to 'model' the rainfall-storage-runoff process? Are higher spatial moments important? Can the area-elevation-aspect approach given here be extended to the case of random or fractal topography? And perhaps, most important, how are the flux-storage relations parameterized across scales.

Not included in this report is the stochastic analysis of hillslopes using spectral and bispectral theory developed by Jin and Duffy (1994) as part of this research. The bispectrum and nonlinear time series analysis paper has been published in Water Resources Research, and reprints are included. The second paper on linear spectral theory of hillslopes, has been submitted to the Journal of hydrology. In future work signal processing and the interpretation of nonlinear signal-response will be a major focus of our effort. In addition we hope to extend the dynamical model to include surface runoff, distributed or nonpoint source water quality response, and the effect of multiple soil and geologic strata.

9. REFERENCES

Ando, Y., K. Musiake, and Y. Takahasi. 1983. Modeling of hydrologic processes in a small natural hillslope basin, based on the synthesis of partial hydrological relationships. Journal of Hydrology 64: 311-337.

Beltrami, E. 1987. Mathematics for Dynamic Modeling, Academic Press, 277p.

Bevin, K. 1983. Runoff Generation and Basin Scale Structure. Reviews of Geophysics and Space Physics 21 (3) : 721-730.

Duffy, C.J., K. Cooley, N. Mock, and D. H. Lee, 1991, Self-affine scaling and subsurface response to snowmelt in steep terrain, Journal of Hydrology, 123, 395-414.

Dunne, T. 1978. Field Studies of Hillslope Flow Processes: Chapter 7. In Hillslope Hydrology. Edited by M. J. Kirby. Wiley.227-293.

Elrick, D. E., W. D. Reynolds, H. R. Geering, and K. A. Tan. 1990. Estimating steady infiltration rate times for infiltrometers and permeameters. Water Resources Research 26(4): 759-769.

Famiglietti, J, and E. Wood, 1991, Evapotranspiration and runoff from large land areas, Surveys in Geophysics, 12, 179-204.

Fan, Y. and C. J. Duffy, 1993, Statistical Analysis of Monthly Temperature and Precipitation Fields on the Wasatch Front, *Water Resources Research, in review.*

Freeze, R. A., 1971, Three-dimensional, transient, saturated-unsaturated flow in a groundwater basin. Water Resources Research, 7, 347-366.

Gupta, V.K., E. Waymire, and C.T Wang, 1980, Representation of an instantaneous unit hydrograph from geomorphology, Water Resources Research, 16(5), 855-862.

Hack, J.T. 1957, Studies of longitudinal stream profiles in Virginia and Maryland: U.S.G.S. Prof. Paper 294-B, 45-97.

Jeppson, R. W., and D. L. Schreiber. 1972. Solution of a two-dimensional, steady-state watershed flow system, Part I. Trans. ASAE 15 (3) : 457-470.

Klemeš, V. 1983. Conceptualization and scale in hydrology. Journal of Hydrology 65: 1-23.

Langbein, W. B.1947. Topographic characteristics of drainage basins, USGS Water Supply Paper 968C, p. 125-157.

Leavesley, G. H., Jr. 1967. Effects of aspect and slope on soil moisture in relation to streamflow on two Shale Hills Watershed. Unpublished Master of Science Thesis. The Pennsylvania State University. 83 p.

Lee, Do-Hun, 1993, Numerical experiments for Richards equation on hillslopes. Ph.D. Dissertation, Civil and Environ. Engrg Dept., Penn State University.

Lee, Do-Hun, and C. J. Duffy, 1993, A Preliminary Model For Nonlinear Soil-Moisture Storage, Recharge, and Baseflow Relationships on Hillslopes, EOS, p.147.

Lynch, J.A., E. Corbett, W. Sopper, 1976, Effects of antecedent moisture on stormflowvolumes and timeing, IAHS, 89-99.

Lynch, J. A. 1976. Effects of antecedent soil moisture on storm hydrographs. Unpublished Doctor of Philosophy Thesis. The Pennsylvania State University. 141 p.

Mandelbrot, B. 1985, Self-Affine Fractals and fractal dimension, Physica Scripta, 32, 257-260.

Neuman, S. P., R. A. Feddes, and E. Bresler. 1975. Finite element analysis of two dimensional flow in soils considering water uptake by roots. SSSAJ 39 : 224-230.

Power, W. and T. Tullis , 1988, Relationship between spectral and divider methods for description of the fractal character of rock surface roughness, Geol. Soc. Amer Abstr. with Programs, A403, 1988.

Richards, L. A. 1931. Capillary conduction of liquids through porous mediums. Physics 1: 318-333.

Rodriguez-Iturbe, I., D. Entekhabi,, R. Bras, 1991, Nonlinear dynamics of soil moisture at climate scales, Water Res. Research, 27(8), 1899-1906.

Rodriguez-Iturbe, I. and J. Valdes, 1979,The geomorphic structure of hydrologic response, Water Resources Research, 15, 1409-1420.

Schumm, S. A., 1956, Evolution of dranage basins and slopes in badlands at Perth-Amboy New Jersey. Geological Soc. of Amer., Bulletin. 67. 597-646.

Sheideggar, 1970, Theoretical Geomorphology, 2nd ed. Springer Verlag, NY. 436p.

Siviplan,M, K. Bevin, and E. Wood, 1990, On hydrologic similarity, 2, A scaled model of storm runoff production, Water Res. Research, 23(12), 2266-2278.

Stephenson, G. R., and R. A. Freeze. 1974. Mathematical simulation of subsurface flow contributions to snowmelt runoff, Reynolds Creek Watershed, Idaho. WRR 10 (2) : 284-294.

Strahler, A. N. 1958. Dimensional analysis applied to fluvially eroded landforms. Bul., of Geol. Soc. of Amer. 69 (March) : 279-300.

Turcotte,D. 1992, Fractals and Chaos in Geology and Geophysics, 221p.

Wolfram, S. 1988. Mathematica: A system for doing mathematics by computer. Addison-Wesley Publishing Company, Redwood City. 749 p.

Yeh, G. T. 1987, FEMWATER: A finitelement model of water flow through saturated-unsaturated porous media, first revision, ORNL-5567/R1, Oak Ridge National Laboratory. 248 p.

Appendix A

PARAMETERIZATION FOR THE RELATION $q(\eta)$

Coefficients for $q(\eta) = a_0 + a_1 \eta + a_2 \eta^2 + a_3 \eta^3$ are summarized as follows.

case	a_0	a_1	a_2	a_3
1	-0.0122566	0.0196948	0.21227	-0.116741
2	-0.00718991	- 0.017625	0.124908	- 0.0581907
3	-0.0218222	0.115633	0.165392	- 0.118292
4	-0.0360373	0.349025	- 0.149575	- 0.00133985
5	-0.00368428	0.0640713	0.403337	- 0.690792
6	-0.0221507	- 0.00867037	0.151819	- 0.0475724
7	-0.0104826	0.246529	- 0.21767	0.061907
8	-0.0221879	0.154545	- 0.153912	0.0958753
9	0.0191508	- 0.025979	0.00798937	0.0018399
10	0.623252	- 0.282881	0.0331941	- 0.000339881
11	0.0163893	- 0.607298	3.36668	- 1.75085
12	-0.000658114	0.00196334	0.00696221	0.00452192
13	-0.238505	0.780319	2.51517	- 1.88448
14	-0.732712	0.445471	- 0.0803704	0.00521475
15	-6.14379	4.19781	- 0.837076	0.0618115
16	-0.00680131	0.129206	0.110856	- 0.0842858
17	-0.011539	0.0467111	0.192838	- 0.111842
18	-0.0135858	- 0.0597895	0.312056	- 0.151315
19	-0.0147494	0.00596443	0.223987	- 0.120729
20	0.00268886	0.0213069	0.184018	- 0.0802037

Appendix B

PARAMETERIZATION FOR THE RELATION $r(\gamma, \eta)$

case	fitted polynomial
1	$r = -0.600596 + 1.54697\,\gamma - 1.02864\,\gamma^2 + 0.653032\,\eta - 0.760397\,\gamma\eta - 0.0811913\,\eta^2$
2	$r = -0.0295403 + 0.141486\,\gamma - 0.146076\,\gamma^2 - 0.130993\,\eta + 0.117487\,\gamma\eta + 0.148161\,\eta^2$
3	$r = -1.25038 + 3.02584\,\gamma - 1.92536\,\gamma^2 + 2.3734\,\eta - 2.48641\,\gamma\eta - 0.996918\,\eta^2$
4	$r = 0.25488 - 0.601226\,\gamma + 0.363603\,\gamma^2 - 1.25134\,\eta + 1.50386\,\gamma\eta + 0.901529\,\eta^2$
5	$r = -0.103359 + 0.649351\,\gamma - 1.04637\,\gamma^2 + 0.137549\,\eta - 0.256117\,\gamma\eta + 0.266241\,\eta^2$
6	$r = -0.448817 + 0.846004\,\gamma - 0.40583\,\gamma^2 - 0.0013853\,\eta - 0.041432\,\gamma\eta + 0.145737\,\eta^2$
7	$r = 0.894396 - 2.2241\,\gamma + 1.39581\,\gamma^2 - 2.57258\,\eta + 3.04769\,\gamma\eta + 1.48404\,\eta^2$
8	$r = 2.06444 - 5.1918\,\gamma + 3.24758\,\gamma^2 - 3.02469\,\eta + 3.80659\,\gamma\eta + 1.18171\,\eta^2$
9	$r = -27.6178 + 13.6557\,\gamma - 1.68858\,\gamma^2 + 7.89528\,\eta - 1.95615\,\gamma\eta - 0.547036\,\eta^2$
10	$r = -44.9498 + 14.2581\,\gamma - 1.13741\,\gamma^2 + 8.15466\,\eta - 1.3029\,\gamma\eta - 0.361111\,\eta^2$
11	$r = 0.856927 - 4.68138\,\gamma + 5.63224\,\gamma^2 - 3.3265\,\eta + 10.2741\,\gamma\eta + 2.94938\,\eta^2$
12	$r = -0.00790433 + 0.0241201\,\gamma - 0.0198697\,\gamma^2 + 0.0037182\,\eta - 0.00287387\,\gamma\eta + 0.00455584\,\eta^2$
13	$r = 8.47777 - 25.5956\,\gamma + 19.9379\,\gamma^2 - 19.1595\,\eta + 27.2253\,\gamma\eta + 10.9892\,\eta^2$
14	$r = 156.052 - 51.557\,\gamma + 4.28883\,\gamma^2 - 29.8699\,\eta + 4.87305\,\gamma\eta + 1.43971\,\eta^2$

case	fitted polynomial
15	$r = 264.71 - 109.193\,\gamma + 11.6957\,\gamma^2$ $- 59.3592\,\eta + 11.5059\,\gamma\eta + 3.44246\,\eta^2$
16	$r = 0.0175777 - 0.0178342\,\gamma - 0.0162536\,\gamma^2$ $- 0.255801\,\eta + 0.440949\,\gamma\eta + 0.280376\,\eta^2$
17	$r = -0.561619 + 1.45122\,\gamma - 0.966134\,\gamma^2$ $+ 0.66263\,\eta - 0.737519\,\gamma\eta - 0.103081\,\eta^2$
18	$r = -2.18251 + 5.31406\,\gamma - 3.29844\,\gamma^2$ $+ 2.95242\,\eta - 3.52763\,\gamma\eta - 0.921721\,\eta^2$
19	$r = -1.32396 + 3.26534\,\gamma - 2.06584\,\gamma^2$ $+ 1.82922\,\eta - 2.13889\,\gamma\eta - 0.562959\,\eta^2$
20	$r = -2.18899 + 5.04628\,\gamma - 2.90585\,\gamma^2$ $+ 2.99582\,\eta - 3.37525\,\gamma\eta - 0.915284\,\eta^2$

Appendix C

PARAMETERIZATION FOR THE RELATION $b(\eta)$

Coefficients for $b(\eta) = a_0 + a_1 \eta + a_2 \eta^2 + a_3 \eta^3$ are summarized as follows.

case	a_0	a_1	a_2	a_3
1	-0.336185	1.79049	-1.89537	0.962291
2	-1.10185	4.64517	- 5.49403	2.39557
3	-0.180528	1.1619	- 1.07807	0.64611
4	-0.0698513	0.575338	- 0.124827	0.215397
5	-0.152382	2.95064	- 6.23662	9.01029
6	-0.50495	1.47304	- 1.04505	0.318246
7	0.0502717	- 0.51244	1.02533	- 0.0774156
8	0.0865337	- 0.851851	2.18505	- 0.798875
9	-0.377101	0.358386	- 0.0760458	0.00738185
10	-4.11953	1.60227	- 0.204627	0.00920631
11	-0.233898	1.3704	- 1.54107	1.01157
12	-0.310726	1.68137	- 1.57922	0.823962
13	-0.338929	1.94723	- 1.86052	0.97213
16	-0.0757071	1.10363	- 1.72519	1.12782
17	-0.26482	1.80463	- 2.25957	1.21578
18	-0.325671	0.730326	0.068719	0.0900953
19	-0.4683	2.07984	- 2.09865	1.02825
20	-0.0111592	0.115312	- 0.0759964	0.40259